MICROCRYSTALLINE SILICON SOLAR CELLS: GROWTH AND DEFECTS

Thèse

Présentée à la Faculté des Sciences
Institut de Microtechnique
Université de Neuchâtel

Pour l'obtention du grade de docteur ès sciences

Par

Martin Python

Acceptée sur proposition du jury:
Prof. C. Ballif, directeur de thèse
Prof. M. Zeman, rapporteur
Dr. A. Poruba, rapporteur
Assoc. Prof. E. Vallat-Sauvain rapporteur
Dr. F. Sculati-Meillaud, rapporteur
Prof. P. Thomann, rapporteur

Soutenue le 5 mars 2009

Université de Neuchâtel

2009

Université de Neuchâtel unine

FACULTE DES SCIENCES
Secrétariat-Décanat de la faculté
- Rue Emile-Argand 11
- CP 158
- CH-2009 Neuchâtel

IMPRIMATUR POUR LA THESE

Microcrystalline silicon solar cells : growth and defects

Martin PYTHON

UNIVERSITE DE NEUCHATEL

FACULTE DES SCIENCES

La Faculté des sciences de l'Université de Neuchâtel,
sur le rapport des membres du jury

Mmes F. Sculati-Meillaud, E. Vallat-Sauvain (Oerlikon-Solar-Lab, Neuchâtel),
MM. C. Ballif (directeur de thèse), P. Thomann, M. Zeman (Delft, NL)
et A. Poruba (Prague, Czech Republic)

autorise l'impression de la présente thèse.

Neuchâtel, le 16 mars 2009

Le doyen :
F. Kessler

UNIVERSITE DE NEUCHATEL
FACULTE DES SCIENCES
Secrétariat - décanat de la faculté
Rue Emile-Argand 11 - CP 158
CH-2009 Neuchâtel
Felix Kessler

■ Téléphone : +41 32 718 21 00 ■ E-mail : secretariat.sciences@unine.ch ■ www.unine.ch/sciences

Mots-clés: silicium, microcristallin, cellule solaire, simulation de croissance, cracks, morphologie de surface

Keywords: silicon, microcrystalline, solar cells, growth simulation, cracks, surface morphology

Ce résumé est dédié aux francophones non-scientifiques. J'espère que cette partie sera digeste et incitera à parcourir quelques pages de cette thèse.

For other people, you will find a brief abstract of this thesis in Section 1.7.

Résumé

Dans cette thèse, l'effet de la structure du silicium microcristallin est étudié. Ce matériau est utilisé pour la fabrication de cellules solaires dites "en couche mince". Ce travail s'est déroulé sous trois approches :

1) L'étude des cellules solaires par des méthodes de caractérisation
2) La modélisation de la croissance du silicium grâce à un programme 3D
3) L'observation des cellules solaires via la microscopie électronique

Le fil rouge de ce manuscrit est l'étude des « cracks ». Les cracks sont des zones de faible densité de silicium (zones poreuses) qui apparaissent lorsque l'on dépose la couche de silicium. Par analogie, on peut assimiler que le dépôt de silicium à la neige qui tombe et qui forme une couche sur le sol.

La première partie du travail est basée sur l'étude de ces zones afin de déterminer leur origine et leur influence sur les performances des cellules solaires. Il s'avère que ces zones sont constituées de micro-vides et sont responsables du phénomène de post-oxydation (l'oxygène s'infiltre dans le silicium par ces zones poreuses <u>après</u> le dépôt de la couche). Ce phénomène peut réduire l'efficacité des cellules solaires

Deux études ont été menées afin de permettre la croissance du silicium sans ces zones poreuses (cracks):

La première approche a été de modifier la morphologie de la surface du substrat. En effet, le substrat est volontairement rugueux (structures pyramidales) pour diffuser la lumière dans les couches de silicium. Il a été observé que ces cracks se trouvent au dessus de la partie en V entre les pyramides. Un traitement plasma permet de modifier la partie en V pour la transformer en U. En d'autres termes, on arrondi la partie entre les pyramides.

La deuxième approche a été d'augmenter la température du substrat lors du dépôt du silicium afin de donner plus d'énergie aux atomes de silicium qui forment la couche. Grâce à ce procédé, le silicium peut se déplacer plus facilement en surface et ainsi, la croissance de la couche se fait de manière plus dense (moins de cracks)
Ces 2 procédés ont démontré une diminution du nombre de cracks grâce au programme de simulation. Divers substrats ont pu être comparés (pyramides avec des parties en V, pyramides avec des parties en U, …). La simulation permet de quantifier le nombre de cracks. Ainsi, l'influence du substrat sur le nombre de cracks a pu être observée. L'augmentation de la température a été modélisée par une augmentation de la diffusion de surface, représentée dans le programme par le nombre d'étapes de diffusion que la particule peut faire avant de se fixer à un endroit.

Les mesures expérimentales ont pu confirmer l'amélioration des performances électriques des cellules sans les cracks. La microscopie électronique a permit d'évaluer le nombre de ces cracks, et la caractérisation (notamment mesures électriques des cellules) a donné les paramètres électriques des cellules solaires. Durant cette thèse, une nouvelle méthode de comptage de cracks a été développée.

Finalement, un nouveau circuit électrique équivalent a été proposé pour prendre en compte l'effet des cracks. En physique, les circuits électrique équivalents (composé de résistances, diodes, …) permettent de modéliser de façon simple le fonctionnement d'un appareil et dans notre cas, le fonctionnement des cellules solaires.

Les principaux résultats de cette étude sont :

- Une meilleure compréhension des performances des cellules solaires microcristallines.
- Une nouvelle méthode, plus simple et plus rapide, pour le comptage des cracks à l'aide de la microscopie électronique.
- La confirmation de la post-oxydation des cellules due aux cracks.
- 2 méthodes pour diminuer le nombre de cracks dans les cellules :
    - Par arrondissement des pyramides.
    - Par augmentation de la température de dépôt.
- Un nouveau circuit électrique équivalent pour les cellules solaires microcristallines.

TABLE OF SYMBOLS

c-Si	Crystalline silicon
a-Si:H	Hydrogenated amorphous silicon
µc-Si:H	Hydrogenated microcrystalline silicon
AM1.5g	Air mass 1.5 global
PECVD	Plasma enhanced chemical vapor deposition
VHF	Very high frequency
RF	Radio frequency
SiH_4	Silane
H_2	Hydrogen
SC	Silane concentration: $SiH_4/ (H_2+SiH_4)$
LP-CVD	Low pressure chemical vapor deposition
ZnO	Zinc oxide
TCO	Transparent conductive oxide
FCA	Free carrier absorption
DEZ	Diethyl-zinc $(C_2H_5)_2Zn$
V_{oc}	Open circuit voltage
J_{sc}	Short circuit current
FF	Fill factor
η	Efficiency
E_0	Urbach parameter
n	Ideality factor
k	Extinction coefficient
Eg	Energy band gap
EQE	External quantum efficiency
FTIR	Fourier transform infrared spectroscopy
FTPS	Fourier transform photocurrent spectroscopy
VIM	Variable illumination measurement
SEM	Scanning electron microscopy
TEM	Transmission electron microscopy
ARS	Angular resolved scattering
Ag	Silver
Al	Aluminum

1. Introduction

The sun has been providing energy on earth for billions of years: the energy received during less than one hour corresponds to the total world annual energy consumption [Markvart 2000]. This renewable energy (at mankind's scale) is free but devices able to absorb and to transform it into useable energy like electricity (photovoltaic (PV) application) or heat (thermal application) are needed. In the first case, photons are directly converted into electricity with the help of a semi-conductor material, such as silicon. In the second case, the sunlight is used to warm a liquid like water for domestic utilization (shower, bath, pool, washing machine …). Furthermore, by using concentrators (mirror that focus the light), on can heat a fluid, creating vapor that is turbined to produce electricity.

1.1. Silicon solar cells

Several materials are used for PV conversion like Cadmium telluride (CdTe) or Copper indium gallium (di)selenide (CIGS), but they include toxic (Cd) or rare materials (In, Te). This makes them unsuitable for long term large scale production compared to silicon, which is non-toxic and abundant on earth.
Silicon is a four-fold coordinated atom that is normally tetrahedrally bonded to four neighboring silicon atoms. In crystalline silicon this tetrahedral structure is repeated many times over a large range, forming a well-ordered lattice (**monocrystalline**). **Polycrystalline** silicon consists of multiple small silicon crystals and can be recognized by a visible grain, a "metal flake effect".
In the domain of silicon-based solar cells, silicon wafers based modules are the most mature product commercially available for PV application, but the energy to produce them and their price is still too high. Indeed, mono-crystalline wafers are composed of high purity silicon of around 200 microns thick and require lots of silicon (~ 3 g/W_p considering efficiency of 15%). Moreover, during the process of fabrication, lots of silicon is lost, because of the kerf losses during sawing.
At IMT Neuchâtel and in several other research labs and industries, thin film solar cells that use a small amount of silicon (cells being typically of the order of 0.25 to 3 μm thick) are in development to decrease the manufacturing costs, while increasing the efficiency. Thin film solar cells are currently one of the most promising industrial routes towards large scale production of photovoltaic electricity.
Thin film silicon solar cells can be composed of 2 kinds of material: hydrogenated amorphous a-Si:H and microcrystalline μc-Si:H silicon, whose microstructure differs from c-Si.

1.1.1. Hydrogenated amorphous silicon solar cells a-Si:H

Chittick et al. first developed the technology in 1969 and it has evolved ever since [Chittick 1969]. Amorphous silicon is the non-crystalline form of silicon. In amorphous silicon long range order is not present and silicon atoms form a kind of continuous random network, with most atoms four-fold coordinated. Due to this disordered nature of the material, two main defects can result: broken bonds (called dangling bonds), resulting in recombination centers and bond distortion, resulting in bandtails. For PV application, the material is passivated by hydrogen (a-Si:H), to reduce the dangling bond density by several orders of magnitude [Kroll 1996]. However, the electrical properties change when this material is exposed to light (light induced degradation). This effect is also known as the "Staebler-Wronski" effect [Staebler 1977]. However, amorphous silicon solar cells (a-Si:H) have now reached reasonable stabilized efficiencies and are produced by many companies.

1.1.2. Hydrogenated microcrystalline silicon solar cells µc-Si:H

The typical microstructure of hydrogenated microcrystalline silicon µc-Si:H consists of crystalline and amorphous phases plus grain boundaries. Additional defects, such as voids and cracks can be present. Microcrystalline silicon layers were produced, one year before amorphous silicon, by Veprek et al. [Veprek 1968] but their development for photoactive layers in PV-devices was stopped because of the poor quality of the undoped material obtained. However, fully microcrystalline p-i-n solar cells were produced by Meier et al. in 1994 in Neuchâtel and have renewed interest in this undoped material as an absorber material [Meier 1994]. Thin films of hydrogenated microcrystalline silicon (µc-Si:H) in PECVD have been widely studied in the last decade [Keppner 1999, Saito 1999, Schropp 1999, Vetterl 2000, Yamamoto 2000, Vallat-Sauvain 2000, Klein 2001, Droz 2003, Zeman 2007]. It is a promising absorber material for single junction solar cells and for the "micromorph" concept [Meier 1994] that consists of tandem solar cells with an a-Si:H top cell and a µc-Si:H bottom cell.
The main advantage of µc-Si:H is the stability of the material compared to an amorphous one. Indeed, no light induced degradation had been observed [Goerlitzer 1997] even though a mild form of degradation has been reported by F. Meillaud et al. [Meillaud 2005]. For thin film solar cells, the concept based on p-n junctions only is not possible, because the doped-layers are too defective (high recombination). Nevertheless, by inserting an intrinsic layer (i-layer) between the n- and the p-layers, the major absorption in the i-layer is achieved and recombination is low. The remaining n- and p-layer (negligible in thickness compared to the i-layer) generate an internal electrical field in the cell to separate the electron and hole (see Section 1.2 for more details). This explains

why these thin film solar cells are called p-i-n junction. It is also possible to deposit n-i-p layers. This series of letters indicates the sequence of deposition: p-i-n means that the p-layer is deposited first. As light always has to enter from the p-side, n-i-p cells can be deposited on transparent and opaque substrates, whereas p-i-n cells are usually deposited on transparent substrates only.
In this work, we study exclusively µc-Si:H deposited by the Very High Frequency Plasma Enhanced Chemical Vapor Deposition (VHF PE-CVD) technique (see Section 1.5). As previously mentioned, microcrystalline silicon (µc-Si:H) is a complex material consisting of small crystalline grains (10-500 nm) embedded in an amorphous silicon matrix, plus voids and cracks. The µc-Si:H microstructure depends on the conditions of deposition [Bailat 2003], on chemical nature of the substrate [Vallat-Sauvain 2005] or on substrate morphology [Bailat 2006]. Three main length scales of disorder can be identified in this material [Droz 2003]:

1. Local disorder: small crystalline grains (black grains in Fig. 1.1) are embedded in an amorphous matrix (grey part). This **amorphous** part contains a certain amount of defect density (dangling bonds)
2. Nanometrical disorder: **small crystalline** grains have random orientation in the amorphous matrix. The boundaries between these grains and the amorphous material consist of a certain form of amorphous tissue
3. Micrometrical disorder: **conglomerates** are formed by a multitude of small crystalline grains. Boundaries between them are also a kind of amorphous tissue. Moreover, with rough substrates, voids and/or micro-cracks (see definition in Section 3.7) can appear during the growth.

Note that the subject of this thesis is focused on the characterization of **µc-Si:H** solar cells.

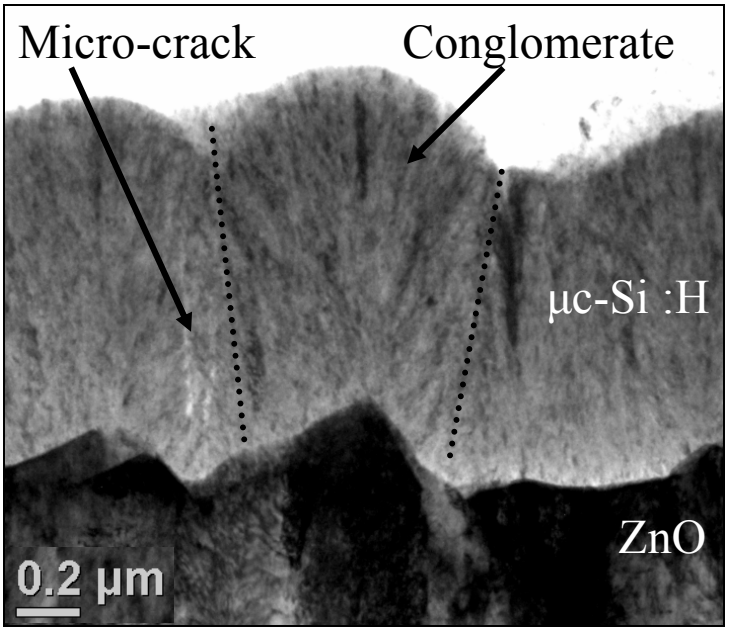

Figure 1.1: TEM micrograph of hydrogenated microcrystalline silicon µc-Si :H.

1.1.3. Multi-junctions and efficiencies

Single junction solar cells can thus be produced with both materials, but multi-junction cells are also possible by combining, e.g. 2 amorphous cells, 1 amorphous with 1 microcrystalline cell (**micromorph** cells) or even 1 amorphous and 2 microcrystalline cell (triple junction) [Saito 2003, Schropp 2003, Rech 2003]
The 2008 certified efficiency records in laboratories for all types of silicon-based solar cells are presented in Table 1.1 [Green 2008].

Type	Efficiency (Lab) (%)	Reference
Monocrystalline	24.7 +/- 0.5	[Zhao 1998]
Polycrystalline	20.3 +/- 0.5	[Schultz 2004]
Amorphous (stable)	9.5 +/- 0.3	[Meier 2004]
Microcrystalline	10.1 +/- 0.2	[Yamamoto 1998]
Micromorph (hybrid)	11.7 +/- 0.4	[King 1994]

Table 1.1 Record efficiency for silicon solar cells larger than 1 cm^2 in labor.

The efficiencies of commercial modules reach 6-7 % for amorphous silicon solar cells and around 8.5 % for micromorph modules (see Ersol, Sharp Kaneka or Fuji company website), as compared to 10% to 15 % for mono- and poly-crystalline wafer modules.

1.2. Operation of a thin film p-i-n solar cell

The photovoltaic effect was first discovered in 1839 by French physicist A. E. Becquerel. Photons (light particles) enter the device (Fig. 1.2a) and are absorbed, permitting a transfer of electrons from the valence band to the conductive band. A photon can create an electron-hole pair only if its energy is equal to, or larger than the energy gap (energy difference between the valence band and the conductive band). Silicon is a semiconductor able to perform this photovoltaic effect, because the gap (1.12 eV) permits to absorb the visible part of the solar spectrum.

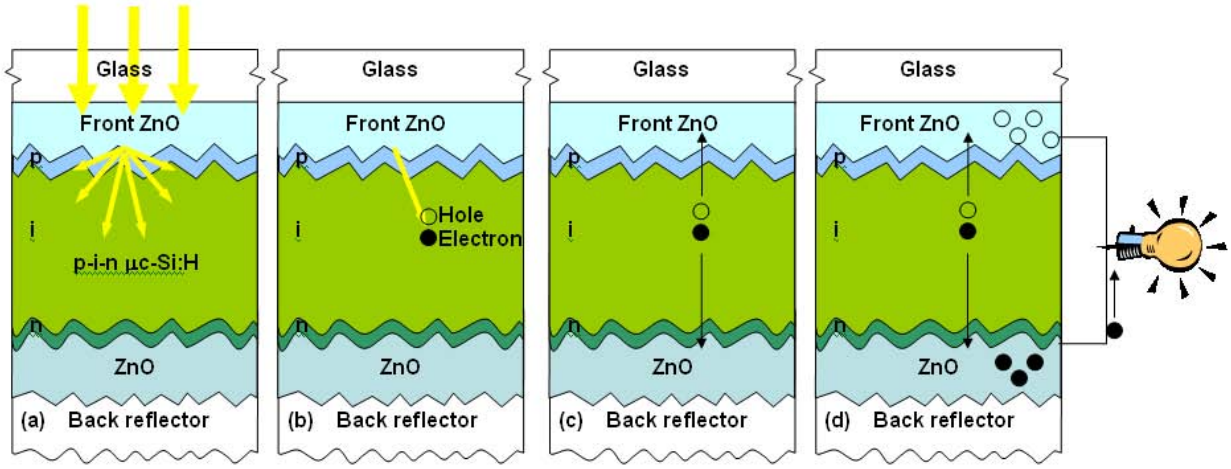

Figure 1.2: Steps to produce electricity from solar energy a p-i-n device:
(a) The photons enter the device.
(b) One photon is absorbed and creates an electron-hole pair.
(c) Electron and hole are separated with the help of an internal electrical field generated by p-doped and n-doped layers.
(d) Electrons and holes arrive at the contacts and follow the external wire → external current.

When an electron is transferred from the valence band to the conduction band it leaves behind a hole, or missing electron (Fig. 1.2b). This process permits the electron and the hole to move freely in the material. Finally electrons and holes are transferred to n/p doped layers respectively by means of the electrical field, created by the doped layers on each side of the silicon absorbing layer (drift) (Fig. 1.2c). The majority carriers then carry the current to a metal contact or a transparent conductive oxide (TCO) like Zinc Oxide (ZnO). An external wire can connect the 2 sides and the electron will move through this wire to create the external current (Fig. 1.2d).

1.3. Front contact

Conductive layers are necessary on each side of the silicon layers in order to collect the electrons and holes. The front contact needs to be transparent to the visible light (that is to be absorbed by silicon) to avoid useless absorption in the conductive layer. The TCO must also scatter the light efficiently to increase the photon optical path inside the cell, and hence the short-circuit current. Zinc oxide (ZnO) is used at IMT Neuchâtel as the TCO. Here the deposition is performed by low pressure chemical vapor deposition (LPCVD), typically at 180°C [Faÿ 2000, Steinhauser 2006]. Typical LPCVD-ZnO layer has few microns thick and is deposited from a vapor-gas mixture of water, diethyl-zinc and diborane on various substrate (i.e. AF45 glass substrates from Schott).

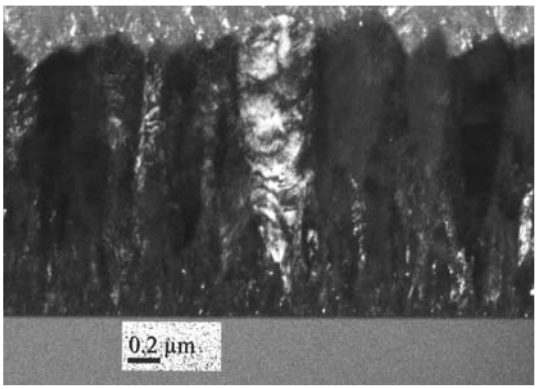

Figure 1.3: Transmission electron microscopy (TEM) in dark field for LPCVD ZnO. The columnar growth is clearly represented by the white grain.

The LP-CVD ZnO growth is typically columnar (see cross section in Fig. 1.3) and has a natural surface morphology composed of pyramids (see top view Fig. 1.4a). In order to improve the silicon growth, a plasma treatment is performed on ZnO (see Fig. 1.4b). As explained in detail in Chapters 4 and 5, the smooth surface morphology instead of rough one leads to better electrical performances (V_{oc} and FF). However, the treatment decreases the light scattering effect due to the change in morphology.

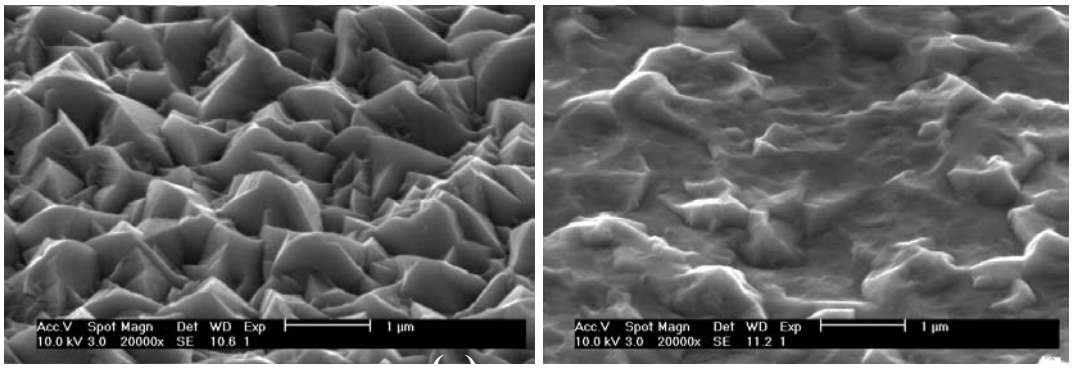

Figure 1.4: (a) As-grown LPCVD ZnO observed by scanning electron microscope (SEM) with a tilt of 45°. (b) Similar ZnO after plasma surface treatment.

1.4. Back contact

For back contact, the conductive layer can be non-transparent. One can use ZnO/Ag or any conductive material that reflects visible light. At IMT Neuchâtel, LPCVD ZnO (same as front TCO) or sputtered ZnO are used. To improve back reflection with the TCO, a reflector can be added such as white paste that diffuses/reflects the light back into the solar cell.

1.5. Thin film solar cell fabrication

Two main methods are used to deposit the active and doped silicon: "hot-wire" chemical deposition (HWCVD) [Heintze 1996, Schropp 1997, Klein 2003] and plasma enhanced (or assisted) chemical vapor deposition (PECVD) [Platz 1998, Lihui 2000, Nasuno 2000, Collins 2003]. The difference between them is that the HWCVD decomposes the silane using a hot wire, whereas the PECVD decompose it using plasma. Solar cells are deposited in Neuchâtel using a PECVD process (Fig. 1.5). Silane (SiH_4) is decomposed by plasma and neutral and ionized sub-components reach the substrate, resulting in layer growth.

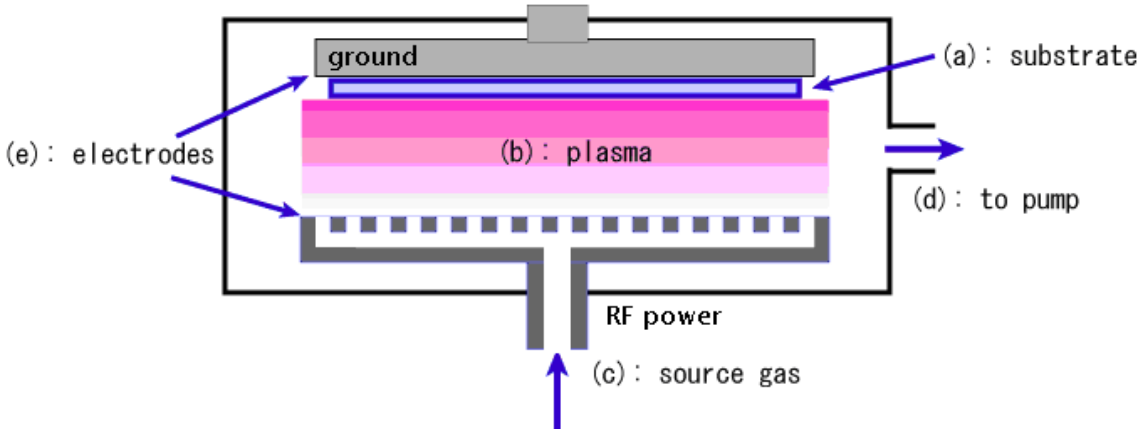

Figure 1.5: sketch of PECVD deposition chamber.

The typical temperature is around 200 °C. Radio frequencies (RF) at 13.56 MHz or very high frequency (VHF), between 25 and 150 MHz [Curtins 1987, Torres 1994], PECVD can be used for such deposition. The increase in frequency permits an increase the deposition rate, which is very useful for commercial application where the process time is important and lower deposition temperature open possibilities for deposition on plastic.

1.6. Goal of the work

In this thesis, the effect of the microstructure, of microcrystalline silicon, as incorporated in operational devices is studied. The effect of substrate morphology on microstructure is simulated and bulk, i-layer material quality is evaluated. The approach was threefold:

1) Study of the devices by characterization methods (optical and electrical)
2) Modeling with help of a program that simulates the growth of silicon
3) Study of material's microstructure by electron microscopy (SEM, TEM and AFM)

In particular, the effect of surface morphology of the substrate (TCO) on the electrical parameters of the resulting solar cells has been studied in detail. Microscopic observations have highlighted suppression of cracks into microcrystalline solar cells deposited on smooth TCO. Moreover, a deeper investigation has been performed in order to incorporate this result into an equivalent electrical model and to understand why these micro-cracks represent an issue. In parallel, a growth modeling program has been modified in order to confirm the effect of substrate morphology and to find an ideal substrate. Finally, an alternative way has been investigated to decrease the number of cracks in the devices, without changing the substrate's surface morphology, by increasing the temperature of the substrate.

1.7. Original contributions of this work

Micro-cracks (further referred to simply as "cracks") in μc-Si:H have been pointed out to be responsible for the decrease in electrical parameters and have already been observed in the literature by [Luysberg 1997, Goerlitzer 1998, Houben 1998, Shah 2002, Graf 2003, Li 2008]. J. Bailat et al. [Bailat 2006], demonstrate a clear correlation between the substrate morphology (treatment of ZnO) and the electrical performances. The treatment of the TCO modifies the surface morphology and increases the fill-factor and open-circuit voltage of the deposited μc-Si:H solar cells. With this method, an efficiency of 9.9 % is reached for single junction μc-Si:H devices. A thorough characterization is performed in this thesis to understand the origin of this behavior, based on a large number of cells.

In particular in this work, the cracks are directly related to losses in fill factor and open-circuit voltage. Moreover, it is demonstrated that these cracks behave as a bad diode in the equivalent electrical circuit. Indeed, by adding such a diode, it is possible to model the J(V) curves of μc-Si:H solar cells deposited on the front ZnO, with various morphologies and thus, to improve the equivalent electrical model originally proposed by Merten et al. for a-Si:H solar cells [Merten 1998].

The physical origin of these cracks is linked to the morphology of the substrate as shown by [Nasuno 2001]. In his paper, the angle theta (opening angle) is the "key parameter" to tune the morphology of the substrate. However, in this work, the curvature radius of the valley of the pyramids of ZnO is chosen as the key parameter via the time of the surface treatment. In our μc-Si:H cells cracks are located above the valleys of the ZnO pyramids (V-shaped). The U-shaped morphology (increase of curvature radii) of the valleys permits a drastically decrease in the crack density and thus improves the electrical performances of the deposited μc-Si:H solar cells [Bailat 2006].

Noticeably, Sakai et al. as well as Löffler et al. have observed cracks in amorphous silicon solar cells [Sakai 1989 and 1990, Löffler 2005] and most of the findings in this work likely also apply here.
The preparation of transmission electron microscopy (TEM) sample for estimating the crack density is time consuming, as discussed in Chapter 2. For solar cell investigation, the method by Benedict et al. [Benedict 1992] is commonly used. In this thesis, a new method is described in order to estimate the crack density using a simpler and faster way.
The variation of ZnO parameters (doping, thickness, morphology) on FTPS measurements, used for intrinsic layer bulk quality assessment, is explored and a method to suppress the influence of the TCO is proposed. Finally, it is concluded that FTPS is not sensitive to cracks (2D like zones).
Finally, Delli Veneri et al. [Delli Veneri 2004] propose to change the substrate temperature during the deposition of the intrinsic layer in order to improve the electrical performances of the deposited μc-Si:H solar cells. Here, we will demonstrate that the increase of substrate temperature during the intrinsic layer deposition leads to a decrease in crack density, as described in Chapter 8. However, other microstructure parameters are also modified, such as crystalline fraction, and a complete optimization of process parameters is still needed to fully take advantage of this effect.

1.8. Outline of the thesis

Chapter 2 discusses the various electrical and optical characterization methods used to analyze thin film solar cells. Microscopy is also introduced with transmission electron and scanning electron microscopy. A new method for counting cracks in microcrystalline silicon is described in this Chapter as well.
Then, Chapter 3 presents a literature review of existing simulation programs that deal with the simulation growth of thin films. A comparison with the MANEMO model used in this thesis is made. Then, a definition of cracks and voids is given, based on experimental results. We emphasize that cracks are composed of porous material and not complete voids.
The growth of microcrystalline silicon with plasma enhanced chemical vapor deposition (PECVD) is presented in Chapter 4 for a large variety of substrates (TCO, wafers). The influence of the substrate's morphology on the material's microstructure and the resulting variations in the electrical parameters is then introduced.
A comparison with the MANEMO program developed in this work and experiments is presented in Chapter 5. The modifications of the program introduced in the framework of this thesis are presented as well: isotropic incidence of particles, diffusion procedure by maximization of neighbors, implementation of new substrates and function for counting cracks. Issues about

density of the growing material are introduced. The crack density as a function of the morphology of the substrate is shown numerically and confirmed experimentally.
Chapter 6 presents Fourier transform photocurrent spectroscopy (FTPS), which is a characterization method to analyze the quality of the bulk material for microcrystalline silicon. The influence of ZnO (doping, thickness and morphology) on FTPS measurements is presented and two procedures to suppress this influence is proposed.
Chapter 7 introduces the "2 diodes model" developed during this thesis in order to model the J(V) curves of microcrystalline silicon solar cells by considering the cracks as a second diode in the equivalent electrical circuit.
A method used to decrease the crack density without modifying the surface of the substrate is presented in Chapter 8.
Finally, the conclusions of this work are discussed in Chapter 9.

2. Characterization techniques

2.1. Introduction

As mentioned in the introduction, thin film silicon solar cells are fabricated, at IMT, by plasma enhanced chemical vapor deposition (PECVD). The cells are processed on 8 cm x 8 cm TCO-coated glass substrates. They are then structured into small area devices (0.25 → 1 cm^2).
The characterization of solar cells is performed using several methods. Current-voltage curves and spectral response are systematically performed in order to calculate the conversion efficiency, whereas other methods are only used in specific cases. In this Chapter, the main characterization methods used in this work are presented. "Variable illumination measurements" allow the measurement of the serial resistance, the shunt resistance, and the collection voltage of the solar cells. "J(V) dark" is useful to determine the diode parameter of the equivalent electrical circuit of the cells. "Fourier transform photocurrent spectroscopy" provides information about the quality of the bulk material. "Micro-Raman" permits the calculation of the crystallinity of the microcrystalline cells and scanning electron microscopy (SEM) as well as transmission electron microscopy (TEM) is helpful in analyzing the surface morphology and the microstructure of the thin film solar cells.

2.2. J(V) Measurement

The efficiency is established, under the so-called "1 sun" illumination, at AM 1.5g, which is defined as the total distribution (direct + diffuse) of sunlight. It corresponds to an integrated irradiance of 1000 W/m^2 incident on a sun-facing plane tilted at 41.8° to the horizontal (P_{light}). The efficiency is then defined by:

$$\eta = \frac{P_{cell}}{P_{light}} \tag{2.1}$$

The current density-voltage measurement (J(V)) is systematically performed after each solar cell deposition. It allows the measurement of the open circuit voltage (V_{oc}) and the fill factor (FF) that are used to calculate the efficiency. In Neuchâtel, this measurement is done by using a "class A" WACOM solar simulator with 2 lamps: a xenon lamp for the UV and blue part of the spectrum and a halogen lamp for the visible and near infrared spectrum. The spectrum is close to the sun spectrum and the illumination is equal to 1000 W/m^2. If the surface of the solar cell is not well defined, and to take into account non-ideality

of the solar simulator spectrum, the short-circuit current density J_{sc} is more precisely measured using the external quantum efficiency measurement (EQE) (see Section 2.3). Fig. 2.1 shows a J(V) curve for a typical µc-Si:H solar cell (thickness around 1.7 µm):

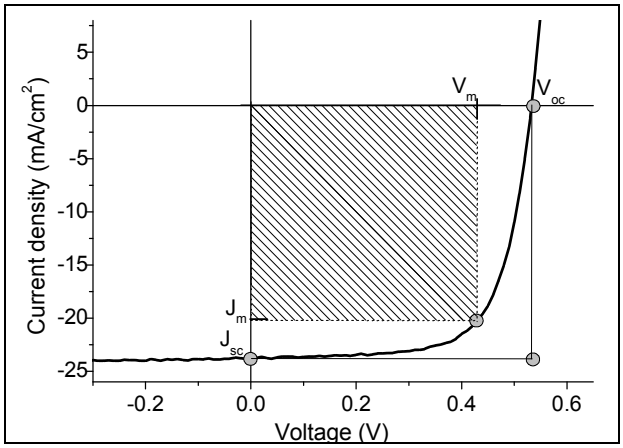

Figure 2.1: J(V) measurement of a typical single-junction microcrystalline solar cell. J_m and V_m are current density and voltage at maximum power point respectively, J_{sc} = 23 mA/cm^2; V_{oc} = 0.520 V.

The open-circuit voltage (V_{oc}) is given by the intersection of the diode response with the x-axis, i.e. where the current density is equal to 0. The fill-factor (FF) is defined as:

$$FF = \frac{J_m \cdot V_m}{J_{sc} \cdot V_{oc}} \tag{2.2}$$

with J_m and V_m the current density and the voltage at the maximum power points, respectively.
In order to easily compare the electrical performances from one solar cell to the other, the product $J_m \cdot V_m$ is generally replaced by the product $J_{sc} \cdot V_{oc} \cdot FF$ and the efficiency is then given by the formula:

$$\eta = \frac{P_{cell}}{P_{light}} = \frac{J_{sc} \cdot V_{oc} \cdot FF}{P_{light}} \tag{2.3}$$

2.3. External quantum efficiency EQE

The external quantum efficiency is the measure of the capacity of the solar cell to convert a photon with a specific wavelength in an electron/hole pair, which will participate (because it has not recombined) to the creation of current in the external circuit under short-circuit conditions. The set-up is composed of a

halogen lamp followed by a monochromator, which separates the different wavelengths of the light, and permits only a narrow range (λ_0 +/- 10 nm) of the spectrum to pass through and reach the solar cell; the photocurrent is measured in short-circuit mode. The intensity of the incoming light on the measured cell is calibrated using a reference cell.

$$EQE = \frac{Current\ measured \,/\, |charge\ of\ 1\ e-|}{Total\ power\ of\ photons \,/\, Energy\ of\ 1\ photon} = \frac{J(E_{photon})}{e\phi(E_{photon})} \qquad (2.4)$$

The total device short-circuit current density is established by integrating the external quantum efficiency over the whole measurement spectrum.
A voltage bias can be applied to the solar cell in order to superimpose an additional electrical field on the electrical field present within the p-i-n (or n-i-p) devices, which favors, in reverse biais, the collection of electron and holes for lower quality cells. Typically, one can thus evaluate collection losses within the device by measuring EQE at 0 V and -2 V.
When variations are observed with J_{sc}, V_{oc} or FF in a series of solar cells, their origin is investigated by means of complementary (non-standard) methods. Such methods are also used from time to time for a complete analysis or when an abnormal behavior appears.

2.4. Variable Illumination Measurement VIM

Variable Illumination Measurement (VIM) is a complementary method for the electrical characterization of thin film solar cells. The complete measurement gives three parameters of the equivalent electrical circuit.

1) The series resistance R_{series}
2) The shunt resistance R_{shunt}
3) The collection voltage V_{coll}

2.4.1. Merten model

In 1998, Merten et al. [Merten 1998] proposed an equivalent electrical circuit for amorphous silicon solar cells (Fig. 2.2):

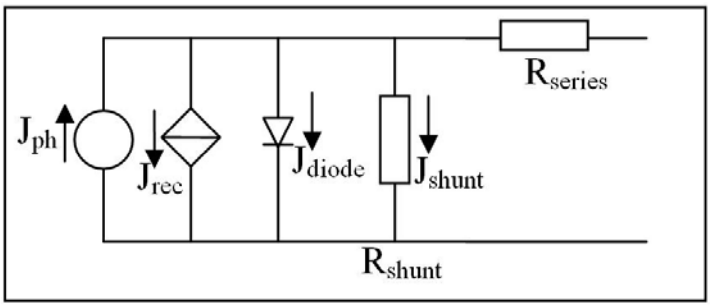

Figure 2.2: Equivalent electrical circuit for a-Si:H solar cell proposed by Merten [Merten 1998], with J_{ph} the photogenerated current density, J_{rec} the recombination current density, J_{diode} the current density of the diode, J_{shunt} the shunt current density, R_{shunt} the shunt resistance and R_{series} the series resistance.

Merten's equivalent electrical circuit allows the fit of a-Si:H solar cells J(V) curves over six orders of magnitude of photogenerated current density. According to [Merten 1998] and assuming negligible diffusion currents, a strong field in the i-layer, thin cells and low defect densities in the intrinsic layer, the total current density may be expressed as the superposition of the photogenerated current density (J_{ph}) minus the current density losses from the diode (J_{diode}), the defects (recombination) J_{rec} and the parasitic effect (shunt and series resistance: R_{shunt} and R_{series}):

$$J(V) = J_{diode} + J_{rec} + J_{sh} - J_{ph} \tag{2.5}$$

that can be rewritten [Merten 1998]:

$$J(V) = \underbrace{J_0\left(\exp\left(\frac{e(V - JR_{series})}{nkT}\right) - 1\right)}_{\text{Diode losses}} + \underbrace{J_{ph} \cdot \frac{d_i^{\,2}}{(\mu\tau)\cdot[V_{bi} - (V - JR_{series})]}}_{\text{Recombination}} + \underbrace{\frac{V - JR_{series}}{R_{shunt}}}_{\text{parasitic effects}} - J_{ph} \tag{2.6}$$

with J_0 the saturation current density, e the elementary charge, n the ideality factor, k the Boltzmann constant, T the absolute temperature of the device, ($\mu\tau$) the mobility – lifetime product of electron and holes and V_{bi} the built-in voltage. The J_{rec} parameter is necessary for a p-i-n junction (not present for a p-n junction), because the absorption occurs in the intrinsic layer that contains recombination centers [Street 1991].

The shunt resistance R_{shunt} is obtained in first approximation by measuring the derivative of the J(V) curve close to J_{sc} (called R_{sc}) at low illumination, whereas the series resistance R_{series} is obtained by measuring the derivative of the J(V) curve close to V_{oc} (called R_{oc}) at high illumination (several suns). Assuming that collection losses are only due to recombination losses in the i-layer, V_{coll} is defined as: [Merten 1998]

$$V_{coll} = \frac{(\mu\,\tau)\cdot V_{bi}}{d_i^2} \tag{2.7}$$

with μ the mobility, τ the lifetime, V_{bi} the built-in voltage and d_i the intrinsic layer thickness. The equation can thus be rewritten:

$$J(V) = J_0\left(\exp\left(\frac{e(V - JR_{series})}{nkT}\right) - 1\right) + J_{ph}\cdot\frac{V_{bi}}{V_{coll}\cdot[V_{bi} - (V - JR_{series})]} + \frac{V - JR_{series}}{R_{shunt}} - J_{ph} \tag{2.8}$$

This model is equivalent to the wquivalent circuit's characteristics for μc-Si:H in Meillaud's thesis [Meillaud 2006].

2.4.2. Measurement procedure

VIM consists of J(V) measurements taken under various illumination levels (G) by using, e.g. grey filters (metallic grids of various meshes) under a solar simulator. After taking the usual "1 sun" J(V) measurement, grey filters are placed between the lamps and the sample in order to remeasure J(V) under a fraction of "1 sun". Typical transmission values of the metallic grids are 52 %, 27.5 %, 10.7 %, 1.4 % and 0.4 % of 1000 W/m^2. Fig. 2.3 presents an example of a VIM measurement. Note that $R_{oc}(G)$ and $R_{sc}(G)$ are calculated with the help of the slope at V_{oc} and J_{sc}, respectively.

$$R_{oc}(G) = -\left(\frac{dV}{dJ}\right)_{J=0} \tag{2.9}$$

$$R_{sc}(G) = -\left(\frac{dV}{dJ}\right)_{V=0} \tag{2.10}$$

R_{shunt} of equation 2.6 is obtained using the value of R_{sc} at low illumination [Merten 1998]:

$$R_{shunt} = \lim_{G\to 0} R_{sc}(G) \tag{2.11}$$

The series resistance R_{series} in equation 2.6 is obtained using the value of R_{oc} at high illumination (several suns).

$$R_{series} = R_{oc}(G) \quad for\ G > 1\,sun \tag{2.12}$$

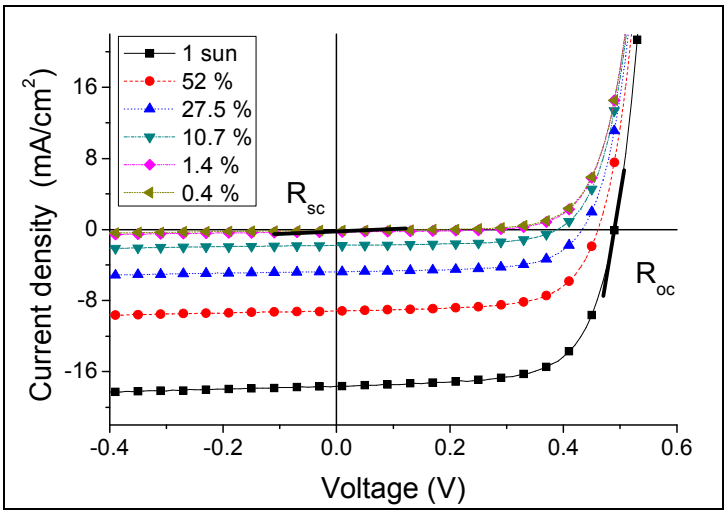

Figure 2.3: Variable Illumination Measurement (VIM) for a typical µc-Si:H solar cell.

Then, by plotting the short-circuit resistance $R_{sc}(1/J_{sc})$ as a function of the reciprocal of the short-circuit current density, one can obtain information on the collection voltage (see Fig. 2.4). The shunt resistance, defined as the limit of R_{sc} (eq. 2.11) when the illumination is low, is seen in Fig. 2.3.

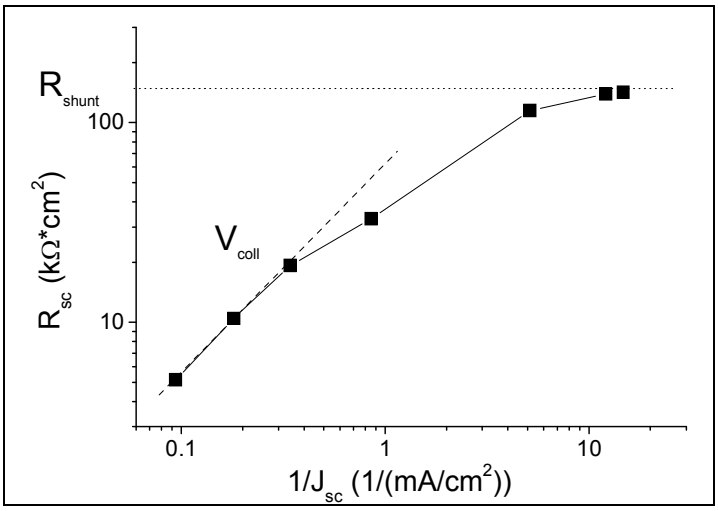

Figure 2.4: Typical VIM measurement for microcrystalline silicon solar cell.

The collection voltage V_{coll} is obtained by linearly fitting $R_{sc}(1/J_{sc})$ for medium intensity levels. High V_{coll} indicates minimum recombination within the i-layer and a good material quality. Typical values for V_{coll} for µc-Si:H is between 20-40 V. The best cells have a V_{coll} higher that 60 V.

In this thesis, a new equivalent model for microcrystalline silicon solar cells is presented, that includes the effect of cracks in the material. Indeed, we will show that porosity in the material modifies the electrical behavior of the solar cell (see Chapter 7).

2.5. J(V) Dark

This experiment is similar to the J(V) measurement, but instead of "1 sun" illumination, the J(V) curve is measured without light. At low voltage, the J(V) curve is related to thermal release of carriers from defect states within the gap [Meillaud 2006a]. An example of a dark J(V) curve is shown in Fig. 2.5 (for the same µc-Si:H solar cell as presented in Fig. 2.1). This measurement helps to determine the ideality factor n and the reverse saturation current density J_0 of the diode equation (Eq. 2.5).

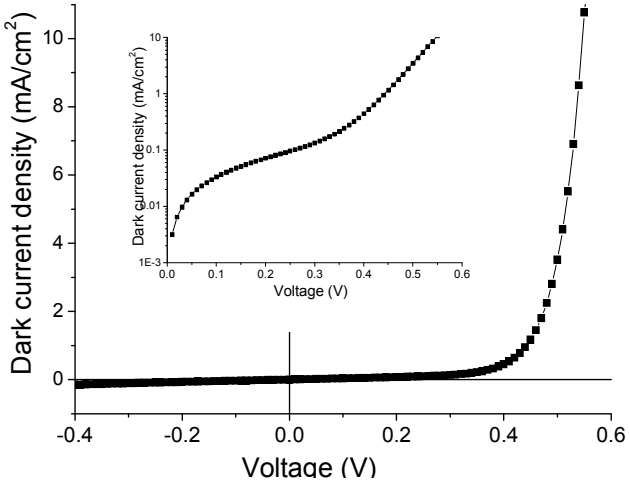

Figure 2.5: JV Dark of a typical microcrystalline silicon solar cell, linear and logarithm (insert) representations.

The ideality factor is related to the microscopic recombination process prevailing in the device (in c-Si, with a thick absorber (200 µm), it is usually assumed: n=1: diffusion current dominates; n=2: recombination current dominates) and J_0, which is related to the defect density of the material [Meillaud 2006]. For µc-Si:H solar cells, the ideality factor is around 1.45 [Python 2008]. J(V) dark measurements have been performed for the Chapter 7 in order to obtain the ideality factor and the reverse saturation current.

2.6. Fourier Transform Photocurrent Spectroscopy (FTPS)

2.6.1. FTPS Set-up

Fourier Transform Photocurrent Spectroscopy (FTPS) is a method that uses a commercial Fourier-Transform InfraRed spectrometer (FTIR) for the measurement of photocurrent (Fig. 2.6). The source of light is a halogen lamp. This excitation beam is modulated in Michelson's interferometer. For our measurements, the CaF_2 beamsplitter is used (utilization range from

approximately 700 to 8000 nm). The interferometer modulates the light at a different frequency for each wavelength. This excitation, modulated in frequency, is then directed towards the outside of the set-up and is focused on the solar cell, which is used as an external detector.
The photocurrent produced by the solar cell is measured in short-circuit conditions. The photocurrent produced by the active, absorbing μc-Si:H layer is amplified by a "low noise current preamplifier" before being digitalized and transmitted to the computer. The spectrum of photocurrent at the different wavelength is rebuilt by taking the Fourier transform of this digitalized signal. The OMNIC interface controls the spectrometer, and displays the measured curves. This solar cell signal must be divided by the baseline to obtain the FTPS spectra. The baseline is obtained using a pyrodetector inside the set-up.

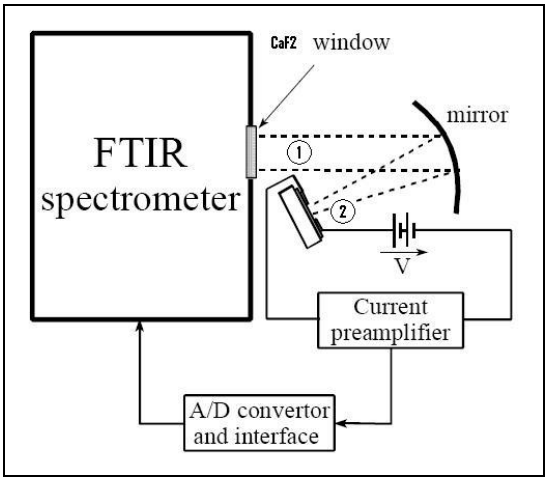

Figure 2.6: Experimental set-up for the FTPS measurement. For layer measurement, an external voltage is applied to separate electrons and holes [Vanecek 2002].

Thus, for the photons with energy higher than the bandgap, FTPS measurement is a measurement of the relative spectral response; by careful calibration, absolute spectral response can be evaluated by FTPS [Poruba 2000, Hod'áková 2006].
For photons with sub-bandgap energy, the measured signal will be produced by electronic transitions involving electronic states in the energy gap. In this case, one measures absorption due to the defects of the material (bandtail state or dangling bonds). By evaluation of the Urbach slope (E_0) and absorption coefficient at 0.8 eV ($\alpha_{0.8}$), one has an assessment of the quality of μc-Si:H [Beck 1996]. Fig. 2.7 shows the possible sources available, the existing beamsplitters, the existing detectors and their working range. In our case, the typical configuration is:

- Halogen source (27000 – 2000 cm^{-1})
- Beamsplitter CaF_2 (14500 – 1200 cm^{-1})
- Detector DTGS (Deuterated TriGlycine Sulfate) (12500-350 cm^{-1})

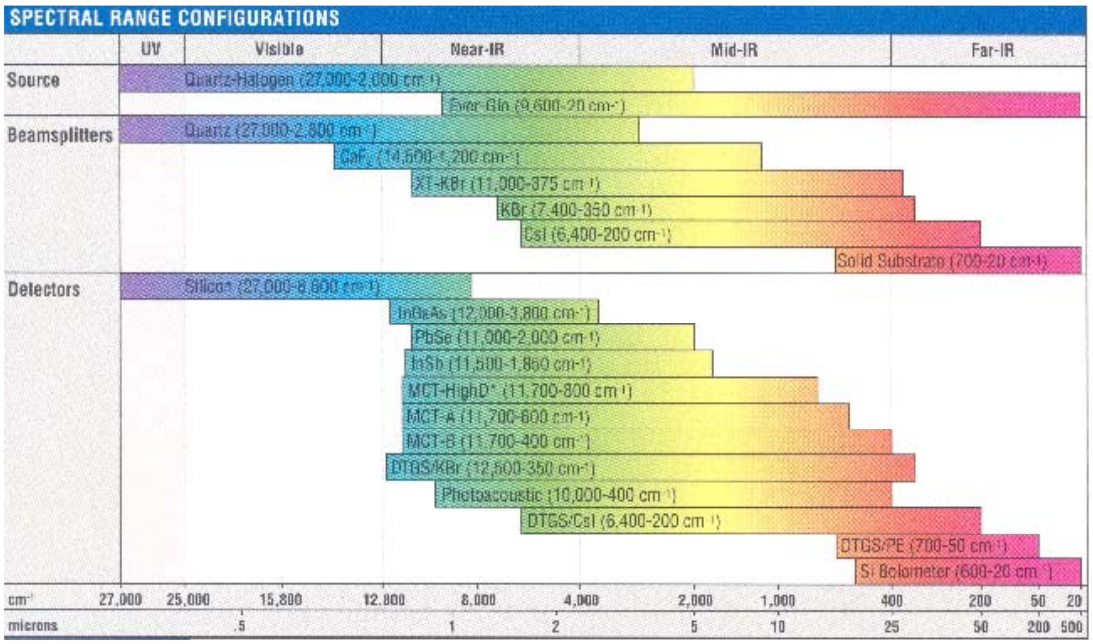

Figure 2.7: Spectral range configurations for FTPS set-up.

2.6.2. FTPS measurements

Thanks to the power of the Fourier transformation method, FTPS allows the measurement of the spectral dependence of the optical absorption coefficient on more than 6 orders of magnitude. It is hence a fast measurement that gives information on the quality on the absorbing (silicon-based) material [Poruba 2008]. The photocurrent is assumed to be proportional to the absorptance in the intrinsic layer of the device. The method is powerful to detect sub-bandgap defects.

In order to measure the FTPS spectrum over a wide range of photon energies, it is hence necessary to measure FTPS signal with filters. Indeed, the measurements are limited by both signal to noise ratio and signal due to second or third order signal. The first effect is represented for example in Fig. 2.8 by the noisy signal on each side of the dotted green curve, whereas the second one is illustrated by the continuous black curve for the photons of lower energy than 1 eV. Thus, in order to obtain the 6 decades of amplitude of the photocurrent, it is necessary to perform several measurements (here 3 measurements have been done):

1) Without filter for the visible part of the light spectrum (WL)
2) With a low pass filter (IKC6) that cuts the spectrum above 1.4 eV
3) With 2 filters (Si + 3C8 filters) that cut the spectrum above 1.1eV

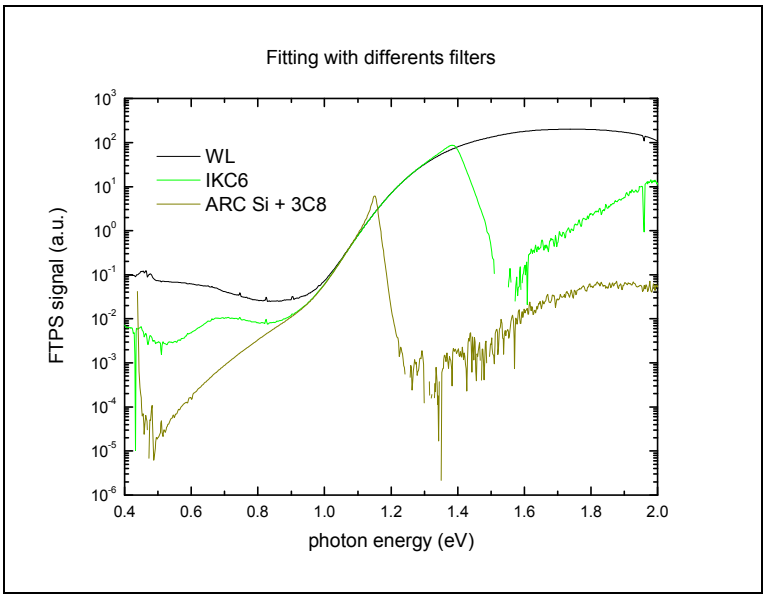

Figure 2.8: Measurements with various filters to establish the FTPS spectra on the full range of energy.

The utilization of those filters thus allows the measurement of absorption coefficient α(hν) over the range of 0.6 to 2 eV by combining the different curves obtained. In Chapter 6 of this thesis, the influence of the TCO on the absorption curve is presented. Indeed, the nature of the TCO as well as its thickness modifies the measured absorption. An original procedure to suppress the influence of the TCO on the FTPS spectrum is presented.

2.6.3. Calibration

The curves obtained by FTPS are not in absolute scale. The FTPS spectra measured in this study were calibrated at 1.35 eV, by setting the absorption coefficient of the µc-Si:H cells to the value of crystalline silicon (245 cm^{-1}). With this calibration procedure, we measure the values of the defect density brought back to the crystalline volume fraction. To obtain an absolute value, the signal should be corrected with the crystallinity. The defect-related absorption is assumed to originate from the defects in the crystalline phase or at its boundaries [Meillaud 2006c].

2.7. Micro-Raman spectroscopy

Micro-Raman spectroscopy is typically used for the measurement of the crystalline fraction of the µc-Si:H material. Raman spectroscopy consists of illuminating the material with a monochromatic light (typically a laser), that is absorbed and interacts inelastically with the phonons or other vibrationnal

excitations of the material resulting in a shift in energy that is typical of the chemical bounds [Voutsas 1995].

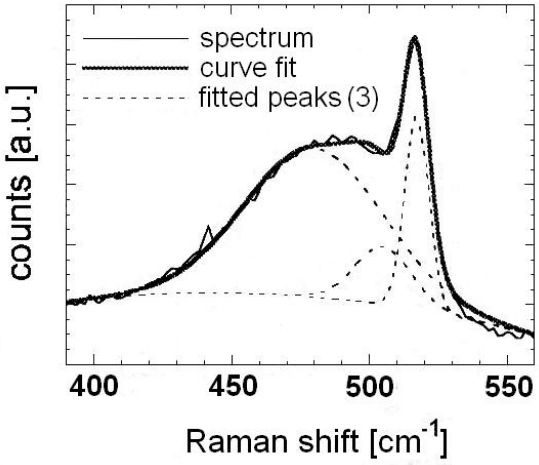

Figure 2.9: Typical Raman spectrum of a µc-Si:H solar cell. The dotted lines represent the 3 Gaussian peaks used to fit the spectrum.

In a Raman spectrum, three peaks are deconvoluted using commercial software (Grams), assuming a Gaussian shape (Fig. 2.9). The amorphous silicon phase of the µc-Si:H leads to the appearance of a broad peak centered at 480 cm^{-1}, whereas the nanocrystalline silicon phase results in an asymmetric peak centered at 520 cm^{-1}. The low-wavenumber tail of this peak (around 510 cm^{-1}) is attributed to the defective, but yet crystalline part of the nanocrystals [Vallat-Sauvain 2006]. By integrating the surface below these peaks, one obtains the Raman crystallinity factor "Φ_c" from the following relationship:

$$\phi_c = \frac{I_{510} + I_{520}}{I_{480} + I_{510} + I_{520}} \tag{2.13}$$

where I_{480}, I_{510}, I_{520} are the integrated areas of the peaks at 480 cm^{-1}, 510 cm^{-1} and 520 cm^{-1}, respectively.

The result is a fingerprint of Raman crystalline fraction given by the excitation laser interaction volume in the sample. The latter is determined by the absorption coefficient of the layer at the wavelength of the laser. For example, a red laser (HeNe, 633nm) has a low absorption coefficient in a-Si and µc-Si, and consequently the Raman signal originates from around 500-700 nm of material, while the Raman signal for a strongly absorbed green laser (Argon, 514 nm) originates from a volume around 50-100 nm deep. Note that the measurement can be done from the side of the cell exposed to air as well as from the substrate side (if transparent) to probe a larger volume [Droz 2003]. The Raman crystalline fraction is related to the volume crystalline fraction by the formula:

$$X_c = \frac{I_c}{I_c + y \cdot I_a} \tag{2.14}$$

where I_a and I_c are the integrating intensity of amorphous and crystalline phase, respectively, and y is the 'Raman emission cross-section ratio'. However, this ratio is not clearly determined for a quantitative evaluation of the crystallinity, as values ranging from 0.1 to 1.9 are reported [Vallat-Sauvain 2006].

2.8. Atomic Force Microscopy AFM

Atomic force microscopy (AFM) is a high resolution imaging technique used to study the morphology at the surface of a sample. It is composed of a cantilever with a sharp tip (see Fig. 2.10). The sharp tip is brought into close proximity with the sample, and scanned over the sample to map the contours of the surface. The variations in the force between the tip and the surface atoms lead to a variation of an optical signal (beam deflected on the cantilever). Usually, while scanning the xy plane, a feed-back loop adjusts the z position so that the value of the optical signal remains close to the set point [Binnig 1987]. (X, y, z) surface maps are then obtained.

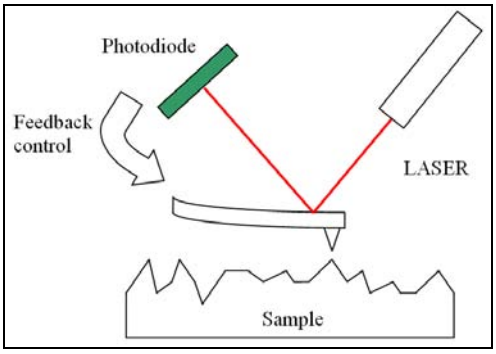

Figure 2.10: sketch of AFM measurement.

The following information can be extracted from an AFM image:

- (a) Root mean square roughness (rms) also called quadratic mean
- (b) Peak to valley height difference
- (c) Geometrical features

It is hence used to statistically characterize the surface morphology [Bailat 2003]. There are several different utilization modes for AFM. In this thesis, samples were scanned in tapping mode. In this mode, the cantilever oscillates near its resonance frequency (around 120 kHz).

2.9. Scanning Electron Microscope SEM

The scanning electron microscope (SEM) is used in this work as a fast surface analysis tool. Electrons emitted from an electron source (lanthanum hexaboride (LaB_6) electron cathode or field emission gun) are focalized on the surface to be studied, they react with the material, and detectors collect electrons or x-rays. X-rays are used for chemical analysis of the material. For topographic information, the 2 main detectors used are: (a) secondary electron detector (SE) for low energy electrons re-emitted close to the surface (~ 10 nm) and (b) back scattered electron (BSE) for high energy elastically back-scattered electrons that come from a deeper region below the surface (to a depth of ~ 450 nm) [Goldstein 2003].
The sample must be conductive enough to avoid the electrostatic charging induced by electron bombardment. For insulator material, a few nanometers of carbon or gold can be deposited on the surface. In Neuchâtel, a Philips XL-30 ESEM with a field emission gun (FEG) is available with an acceleration voltage ranging between 5 to 30 kV.

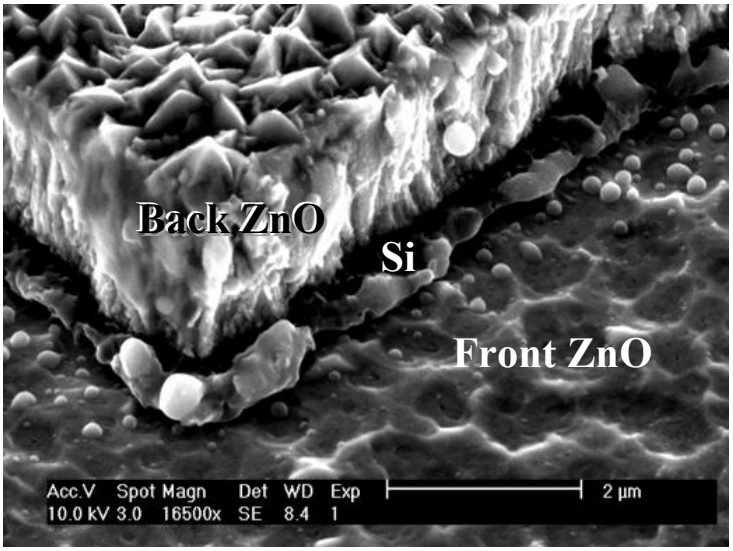

Figure 2.11: SEM micrograph: View of a-Si:H solar cell separated by laser scribing: silicon layers between two ZnO layers.

Fig. 2.11 presents a SEM micrograph of an a-Si:H solar cell. The laser scribing has removed the silicon layers and the back ZnO from the front ZnO. Energy Dispersive X-Ray (EDX) is a method, available with this microscope, which permits the analysis of the chemical nature of the sample's surface, by monitoring X-rays emitted from transition in the core level of sample's atoms.

2.10. (High Resolution) Transmission Electron Microscope (HR) TEM

Transmission electron microscopy (TEM) is a powerful tool for material sciences in general. Indeed, optical microscopes are limited in resolution due to the wavelength of the order of few hundreds of nanometers. Thus, using accelerated electrons with wavelengths down to picometers (10^{-12} m or 0.001 nm) as is it the case with TEM, it is possible to increase the magnification (maximum around 5 mio. times). The limitation for resolution in TEM is the aberration of magnetic lenses.
TEM observation requires very thin samples (20-100 nm), because they must be transparent to electrons. Electrons generated by the electron gun (similar to SEM) are diffracted by atomic planes of the sample. With an aperture that suppresses diffracted electrons from the image, one obtains a contrast between transmitted electron and diffracted electrons (see Fig. 2.12 bottom right). In the focal plane, one can observe the diffraction and thus obtain a pattern related to the crystal structure (Fig. 2.12 top right). Details of the set-up are presented in Fig. 2.12 on the left. An opening can be inserted in the focal plane to select either the direct beam (bright field) or the chosen diffracted beam (dark field).

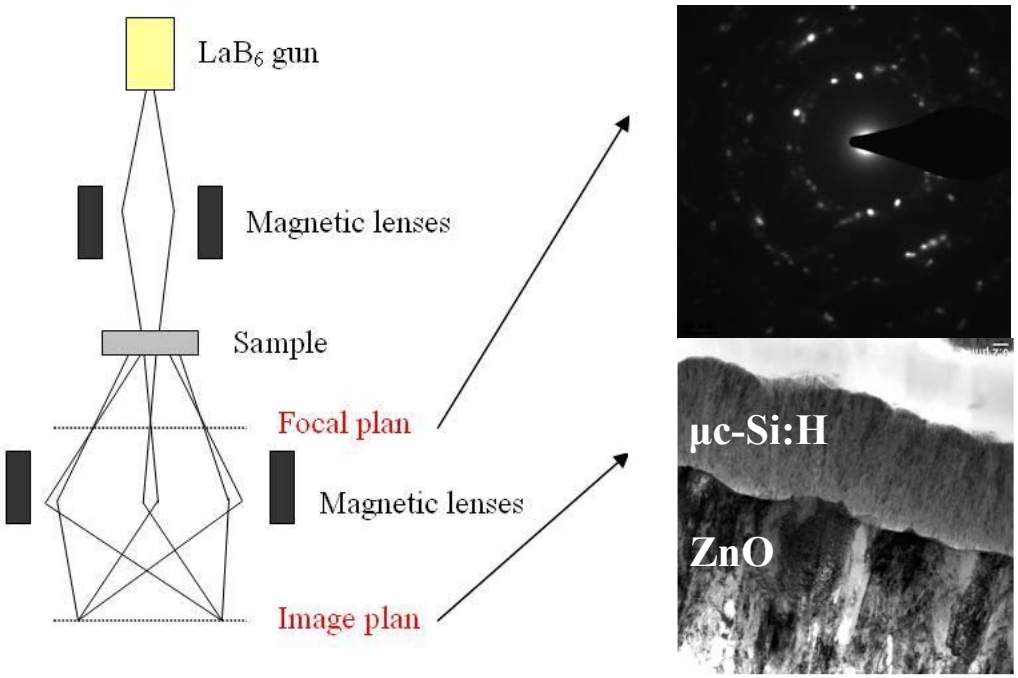

Figure 2.12: Left: Sketch of TEM set-up / Right: top: objective lens's focal plane for ZnO sample; bottom: image plane of objective lens of µc-Si:H on ZnO.

The difficulty to prepare thin samples is the major drawback of TEM. Moreover the sample preparation is time consuming (typically 1 full day is necessary to prepare one sample). Methods of preparation are discussed in the next Section. In Neuchâtel, one uses a Philips CM-200 that accelerates electrons from a LaB_6 filament at 200 kV. EDX is also available on the TEM.

2.11. Sample preparation for electron microscopy

2.11.1. Existing methods

The preparation of samples for Transmission Electron Microscopy (TEM) is a science in itself. Indeed, depending on the substrate (the material or the structure) several approaches are possible. Thus, several sample preparation methods are available (see the non-exhaustive list below):

1) Ion bombardment (thinning of the sample by argon bombardment)
2) Wedge polishing (with or without ion bombardment), explained in detail in this section
3) Cleavage (cut by following atomic direction) [McCaffrey 1991]
4) Ultra-microtomy [Wessels 2006]
5) Electrolyte polishing [Tanem 2005]
6) Deposition of thin film layer, films scraped from the glass substrate and fragments directly picked on a carbon-coated TEM grid [Vallat-Sauvain 2000]
7) Focused Ion Beam (FIB) [Abolhassani 2006]

For the study of thin film microcrystalline silicon solar cells, three of these methods have been used: Ion bombardment, Wedge polishing and FIB. The most important points investigated in this work are the structure of the films (growth and cracks) and the thickness of the layers.

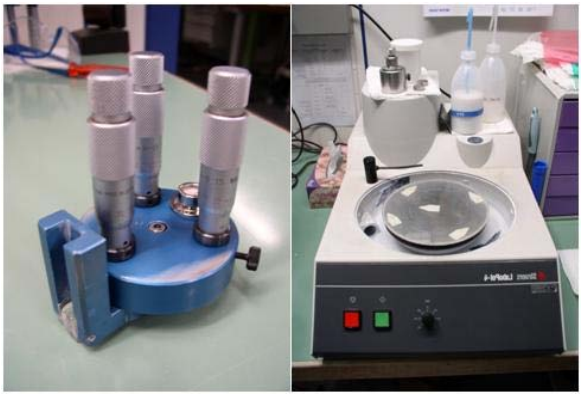

Figure 2.13: Left: Tripod used for wedge etching sample preparation / Right: rotative plate Struers LaboPol-4.

For solar cells, wedge polishing of edge or parallel cross-sections followed by ion bombardment has been extensively used (see [Bailat 2004]). First, a "sandwich" of solar cells is prepared as described in Benedict et al. [Benedict 1992]. Second, mechanical polishing is performed to further reduce the

thickness of the sample with a series of diamond films with various grain sizes, on a rotative plate Struers LaboPol-4 (Fig. 2.13 right). It is followed by a chemico-mechanical polishing step with a colloidal silicate on a velvet plate. The sample is fixed to a tripod (Fig. 2.13 left). The first face is polished, and then an angle (around 0.6%) is applied for polishing of the second face (see Fig. 2.14 left). If ion bombardment (Baltec Res-100) is used, the second face is polished parallel and a hole is drilled at the focus of the accelerated Ar^+ ions at few kV (Fig. 2.14 right). In the first case, the electron-transparent area lies along the thinner side and in the second case, it is at the center, near the hole. A short ion bombardment step can also be performed on edged samples to further reduce the thickness or to clean the sample.

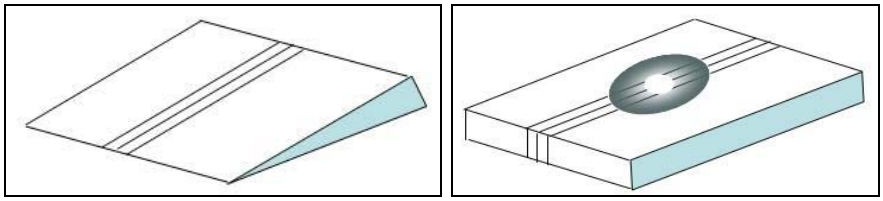

Figure 2.14: Left: Edged chemico-mechanically thinned sample / Right: Mechanically thinned and argon etched.

For FIB preparation, the macroscopic sample is inserted in a SEM equipped with a gallium ion source. Thus, the ions are accelerated and etch the material. The sample preparation follows these steps:

a) The sample is protected by local deposition of platinum
b) Two areas are etched on each side of the sample
c) A support (tip) is fixed to one side of the sample (point A in Fig. 2.15 left) in order to keep one fixed point to the sample (not shown here)
d) The second side is cut (point B in Fig. 2.15 left)
e) The first side is cut (after the fixed point) (point C in Fig. 2.15 left)
f) The tip moves the sample close to the sample holder
g) The second side is fixed to the sample holder (Fig. 2.15 right)
h) The tip is released from the sample

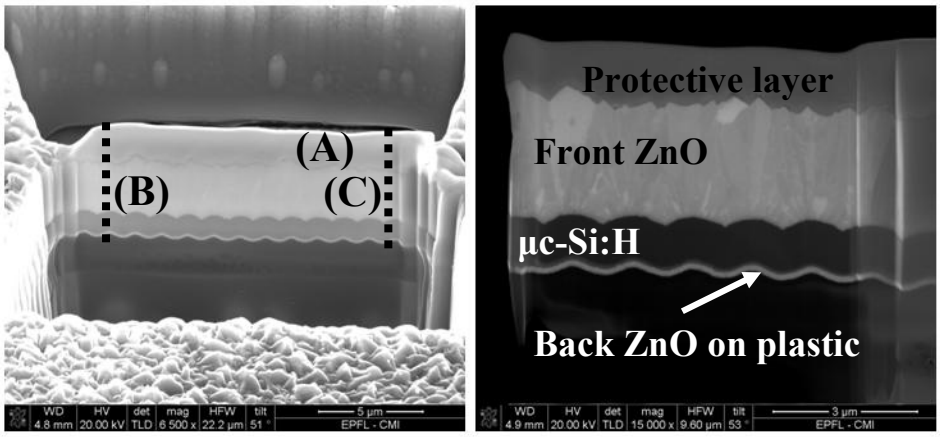

Figure 2.15: SEM micrograph of FIB preparation. Left: 2 areas are etched away on each side of the sample. Right, the sample is fixed on a sample holder. Courtesy of Mireille Leboeuf.

The focused ion beam method is the most expensive one. Thus, only special preparations are performed with this method, i.e. solar cells deposited on flexible substrates that cannot be edged-polished. Furthermore, the length of the FIB thinned area is around 10 microns, which is not optimal for statistical investigation. The FIB set-up is located at the EPFL in Lausanne (FEI Nova 600 Nanolab)

2.11.2. New method for counting cracks in the solar cells

Cracks can be observed by transmission electron microscopy (TEM) and appear as white lines in bright field mode slightly under-focused, as seen in Fig. 2.16.

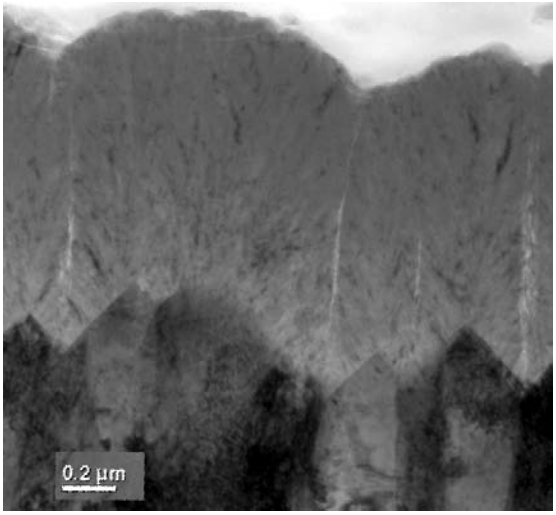

Figure 2.16: Microcrystalline silicon on as-grown ZnO by TEM. The cracks look like white lines in the silicon layers (contrast du to lower absorption in less-dense cracks).

Unfortunately, the preparation of TEM samples is time consuming. In order to estimate the density of cracks, another, easier and faster sample preparation

method is presented below. With this new method, SEM is sufficient for observation. The procedure is inspired from the TEM sample preparation with a tripod from Benedict et al. [Benedict 1992] and is called: "**1 face polishing**":

- First, a "sandwich" is prepared by cutting the solar cell in two pieces 2x10 mm^2, which are glued in front of each order with epoxy glue. The glue needs to be heated for 40 min at 100 °C before cooling at room temperature. The cutting is performed with a "Well 3242" composed of a diamond wire with diameter of 170 microns.

- Second, the sandwich is placed on a tripod in order to polish the face. Allied papers (High Tech Products, Inc.) with various grain sizes: 30 µm, 15 µm, 6 µm, 3 µm, 1 µm, 0.5 µm and 0.1 µm are consecutively used to achieve a surface as flat as possible. The last step of polishing (chemico-mechanical) is performed with alkaline silicate colloidal on a velvet plate on a "Struers LaboPol-4".

- Third, the sandwich is cut under 1 mm of the polishing face and stuck on a carbon scotch (polished face up). A few nanometers of carbon are deposited by evaporation on the surface and a small wire of carbon is placed to connect the top surface with the sample holder via the carbon scotch to avoid surface charging during SEM observation.

- Finally, the surface is observed under a scanning electron microscope (SEM) in "back scattered electron" (BSE) or "secondary electron" mode (SE).

A linear crack density (crack/micron) is estimated by counting the number of cracks along the substrate plane on SEM micrographs, such as on the one presented in Fig. 2.17.

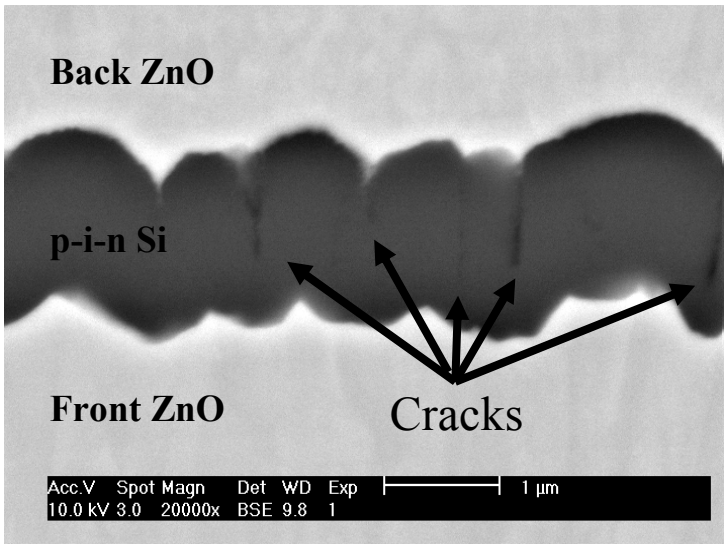

Figure 2.17: SEM micrograph of µc-Si:H solar cell. Cracks appear as darker lines due to the lower density of material.

The time necessary for the preparation of such sample is considerably decreased as compared to the preparation of lamellae for TEM observations. Indeed, instead an average of 1 sample per day, it is possible to analyze and observe 4 samples per day. Moreover, the preparation is easier and leads to an observable length of 4000 microns, allowing for a better statistics for crack counting.
The SEM micrograph (Fig. 2.17) obtained with this sample preparation method look similar to images obtained in a previous study by scanning Kelvin probe microscopy (SKPM) [Dominé 2007]. In this previous work the SKPM technique allowed us, for similar samples, to identify a higher local work-function at the cluster boundaries formed by this porous µc-Si:H material.
This original method, initially developed for counting cracks, has allowed us to analyze issues of ZnO deposition and other defects as well:

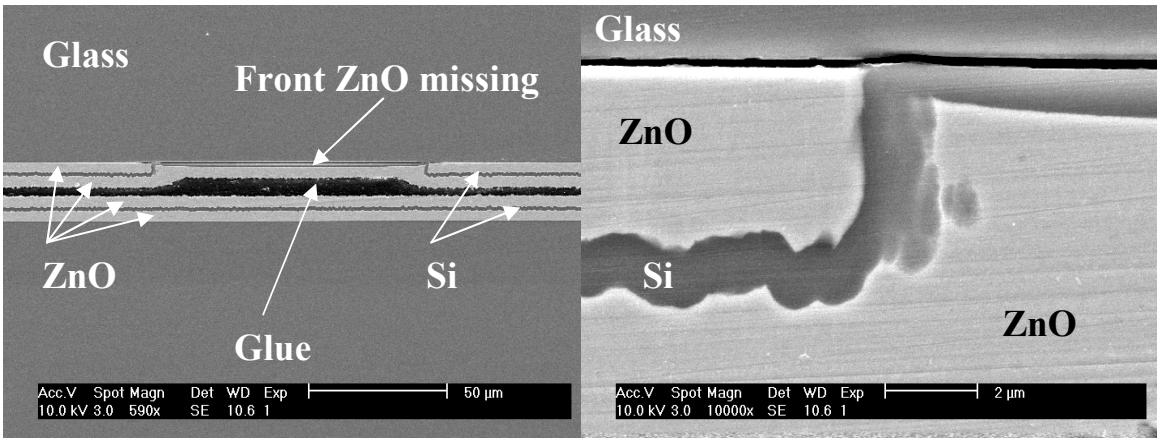

Figure 2.18: SEM micrograph of ZnO missing on glass. Right: zoom of left micrograph.

In Fig. 2.18, we can observe a part of a µc-Si:H solar cell where the front ZnO is missing, which is probably due to a dust particle on the glass removed after deposition of the front ZnO layer. On the next micrographs (Fig. 2.19), the

defective growth is again due to a particle of dust, which was probably on top of ZnO before silicon deposition.

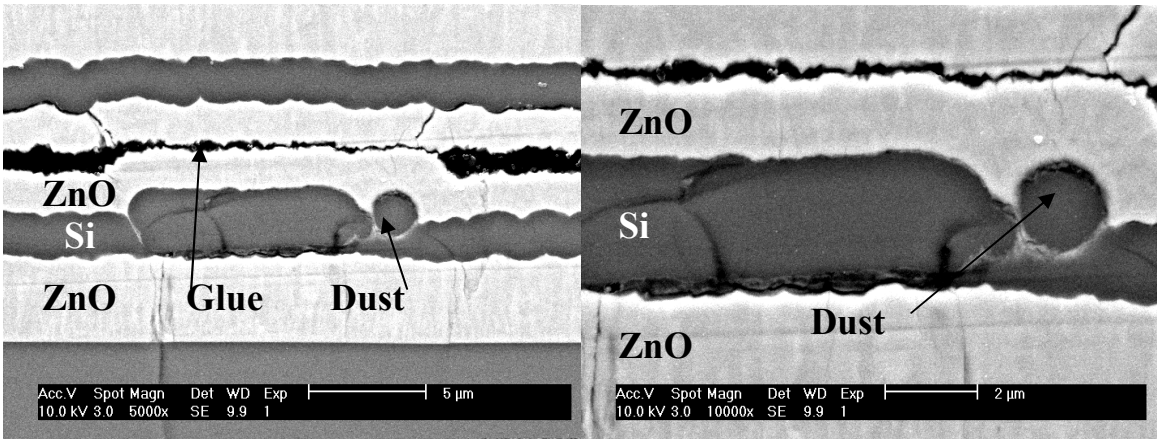

Figure 2.19: SEM micrograph: dust between ZnO and silicon deposition that leads to defective growth. Right: zoom of left micrograph.

2.12. Conclusion

Electrical characterization of devices (J(V), EQE, VIM) will be performed with morphology (SEM, AFM) and microstructural analysis (TEM) to diagnose the effect of substrate morphology and device microstructure on electrical performances of solar cells. Moreover, Fourier transform photocurrent spectroscopy (FTPS) and micro-Raman spectroscopy will be used to complete the understanding of the properties of series of solar cells (crystallinity, i-layer quality). In Section 2.11.2., a new method to estimate the crack density is presented and will be used in order to analyze the density of cracks in the cells in Chapter 8.

3. Thin film growth: simulation and experiment

3.1. Introduction

Contact filling in microelectronics for very large scale integration (VLSI) (process of creating integrated circuits by combining thousands of transistor-based circuits into a single chip) is the domain in which interest is the largest in software development for simulation of layer growth. Consequently, numerical growth models have been mostly designed for simulation of metallic contact deposition within deep trenches: SAMPLE [Oldham 1979, Oldham 1980], SPEEDIE [Rey 1990, McVittie 1990], SIMBAD [Dew 1991] or SHADE [Hamaguchi 1993]. For industrial applications, the actual trend is to take electrical contacts as deep as possible in wafers, in order to maximize their bulk utilization [Chatterjee 1995]. In order to reach deeper contact, it is important to control the growth in a conformal way, as illustrated in Fig. 3.1.

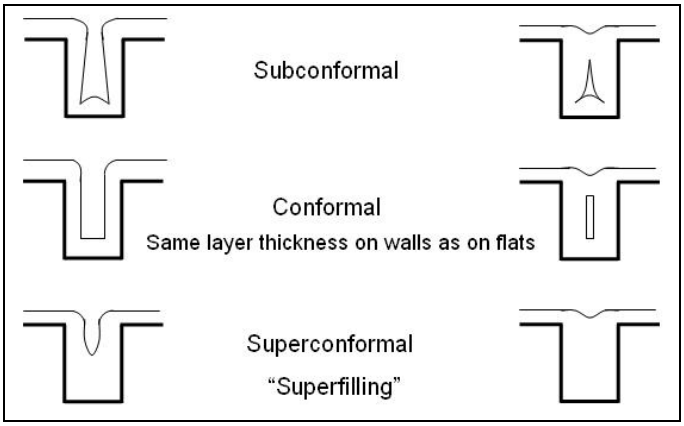

Figure 3.1: Definition of conformality as used for the growth in trenches.

When the growth is called subconformal or superconformal, it means that the deposited layer thickness is not constant when measured perpendicularly to the substrate's surfaces as presented in Fig. 3.1. The thickness of the deposited metallic layer particularly affects: resistivity, etching characteristic, oxidation, index of refraction, permittivity, diffusion properties and surface roughness., which is the reason why it is important to monitor the growth.
In order to study the effects of deposition parameters on the growing layer's morphology, an important number of samples should be prepared and characterized. Sample preparation is time consuming and simulation programs are hence very useful. Indeed, they improve our understanding by comparison of predictions from numerical simulations with experimental observations. It drastically reduces the number of associated experiments and optimizes manufacturing processes within the framework of existing processing systems.

A general overview of the recent numerical simulations for metallic "Trench filling" is presented in this Chapter, and simulation of thin film silicon deposition by PECVD will be described for growth of μc-Si:H solar cells on substrates with trenches. In Chapters 5, we will study the effect of substrate surface morphology on silicon growth and microstructure with a simulation program introduce in Section 3.4.

3.2. Simulation

A numerical simulator may be constructed in a variety of ways, depending on the goal, machine limitations, and state of the art in modeling the physical process of interest. In general, any model for thin film deposition can be separated in two distinct subroutines:

(i) The generation of growth species and its transport from the source to the substrate.
(ii) The incorporation of the species into the growing film by considering roughness, surface diffusion length, local relaxation or material removal.

For (i), different approaches can be used depending on the process involved (sputtering, CVD, PECVD, Hot-wire …), the geometry of the system (target shape in sputtering, gas distribution in CVD), and the process parameters (power density, pressure, gases concentrations). Fig. 3.2 shows an example of 3D flux treatment where the particle trajectory is determined by two angles.

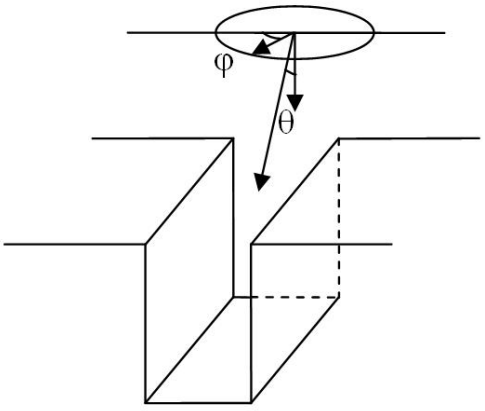

Figure 3.2: Example of angular distribution of adatoms.

For (ii), the incorporation of material follows discrete or continuous equations. The majority of models are "continuous models": a parameter such as the internal energy is minimized to decide on the incorporation of the impinging particles (called adatoms) on the growing surface.

3.3. Existing programs

As previously mentioned, most existing softwares are used to model metallization in trenches. One can classify these models as a function of several criteria. One of them is the type of equation (discrete or continuous) that describes the physical laws governing the evolution of the growing surface. Some models use a continuous description and numerically solve the thermodynamical equation (e.g. minimization of internal energy). In the other models, a discrete approach is used, in which the evolution of the growing surface is described by the ballistic collision of growth species on the surface. In this case, a dynamical approach is used for the description of the incorporation of local adatoms.
The most widespread statistical approach is the Monte Carlo (MC) simulation [Ikegawa 1989, Fichthorn 1991, Stout 1993], which is widely used for algorithm procedures. It is a stochastic, non-deterministic method, using random numbers. The name "Monte Carlo" was popularized around 1940 by physicists working on nuclear weapons (the name is a reference to the Monte Carlo Casino in Monaco). Indeed, the use of randomness and the repetitive nature of the process are analogous to gambeling.
Historically, the first models were created to simulate the growth of metallic layers in sputtering systems. At the beginning, 2D models were created like SAMPLE [Oldham 1979, Oldham 1980], SPEEDIE [Rey 1990, McVittie 1990] or SHADE [Hamaguchi 1993]. They are designed to produce cross-sections of trenches at various stages in the processing, see Fig. 3.3. For example, SPEEDIE uses statistical approach calculations to determine the incoming particle's trajectory (as in Fig3.2). Then, the particles can be absorbed or re-emitted. After the Monte Carlo simulation, the number of particles attached to each string has to be converted to the particle distribution on the surface. Finally, a process of smoothing is performed [McVittie 1990].

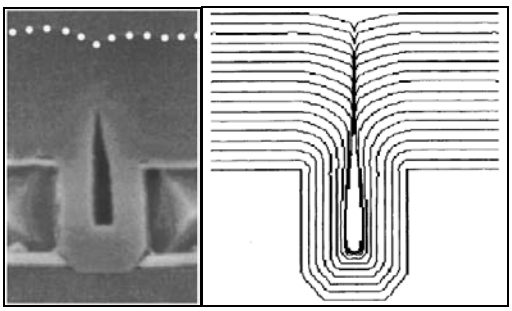

Figure 3.3: Continuous model for simulation's deposition (SPEEDIE). Left: SEM micrograph. Right: equivalent simulation [Rey 1990].

These softwares correspond well with scanning electron microscopy (SEM) or transmission electron microscopy (TEM) observations of layer's surface morphologies at various stages of growth. The problem here is to obtain a representation of the layer structure. Thus, complementary simulation programs have been created, such as SIMBAD, where a ballistic approach is considered [Dew 1991]. Here, information about microstructure of the growing layer is obtained as can be seen in Fig. 3.4.

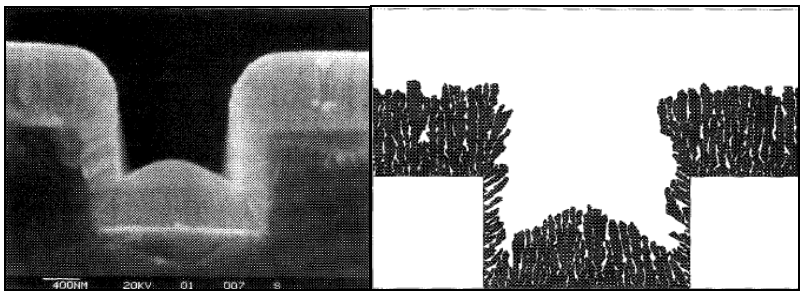

Figure 3.4: Simulation of deposition in a trench by SIMBAD [Dew 1991].

Another program using the ballistic approach is presented in Fig. 3.5. Instead of using blocks with the shape of a disk as in SIMBAD, "3D-films" uses cubes. These cubes can take a color representing material information or local temperature [Smy 2001]

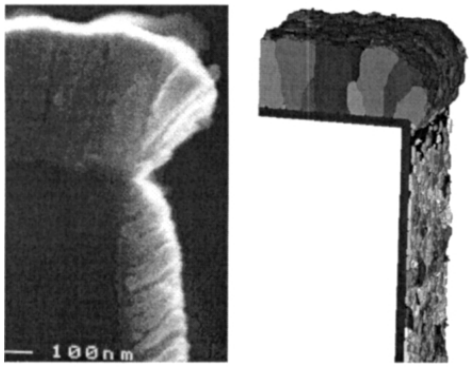

Figure 3.5: Simulation of deposition with « 3D-films » program [Smy 2002].

Simulation of deposition of thin films performed by Physical vapor deposition (PVD) or ionized physical vapor deposition (IPVD) is presented in Fig. 3.6. Here, a molecular dynamics approach is used for calculation of target emission spectra and Monte Carlo (MC) for the simulation of the transport at the reactor [Belsky 2005].

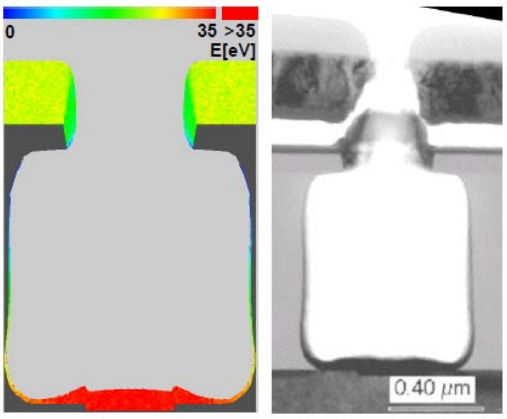

Figure 3.6: Simulation of deposition. Left: energy deposition in eV/atom, 2D profile; right: TEM micrograph of the film in the feature [Belsky 2005].

Molecular dynamics is also used to simulate the transition between amorphous material and μc-Si:H, during post deposition hydrogen exposure [Sriraman 2002]. Even if this method is not related to the trench filling, it is mentioned here, because, to the author's knowledge, it is the only one currently able to simulate the transition of the material's microstructure at a fundamental level.

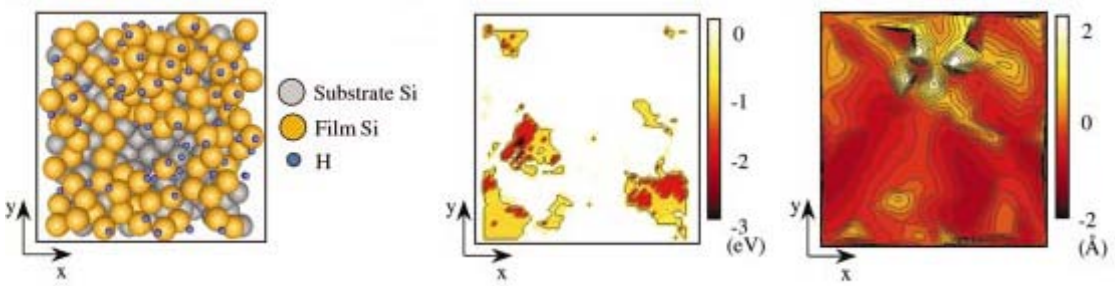

Figure 3.7: Left : surface structure ; middle : surface chemical reactivity with SiH_3 radicals; right: surface morphology during a-Si:H film growth. [Ramalingam 2001].

3.4. MANEMO software

In Plasma Enhanced Chemical Vapor Deposition (PECVD), growth of the solid phase occurs far from thermodynamical equilibrium (from condensation of the gaseous species on the solid surface). For this reason, a thermodynamical approach to this system is not appropriate. Ballistic growth approach, where local equilibrium is macroscopically considered, is hence used to simulate the growth of thin solid films for PECVD [Barabasi 1995]. The program developed by Bailat et al. [Bailat 2004a] and further developed here (the so-called "MAjority NEighbours MOdel MANEMO) is currently able to simulate the transition of the material's microstructure from amorphous to microcrystalline silicon. An example of μc-Si:H microstructure is presented in Fig. 3.8.

Figure 3.8: Dynamical modeling with MANEMO. Microcrystalline growth on trenches. Variations of grey (or color) represent the various crystallographic orientations.

3.5. MANEMO vs existing approach

Our model will be described in detail in Chapter 5. Here, we compare it to the other existing models either for simulation of growth of metallic trenches or of insulator/passivation layers. As we use a discrete, atomistic-like, description of growth, our model can only be compared with the SIMBAD model, which is able to simulate cracks and voids within the deposited layer, but is unable to simulate the transition from a non-ordered to an ordered material. It will be seen that the choice of the angles of particles to calculate their patrajectories to achieve an isotropic distribution is a Monte-Carlos process.

With MANEMO software, no "physical equation" is used, but only basic "rules" are applied which has the following advantages:

- Easy to achieve numerically (nevertheless the treatment of boundary conditions, and of particle contact with the surface, has to be taken carefully into account, and is described in detail in Chapter 5)
- Fast to implement (graphical treatment)
- Allows an easy treatment of various concepts (modification of selection rules)

3.6. Thin film silicon growth in PECVD: general aspects

In contrast to metallization that is performed by sputtering, growth of insulators or passivation layers such SiO_2 and SiN is achieved by Plasma Enhanced Chemical Vapor Deposition (PECVD) in the semiconductor industry. Many simulations have been made to characterize the chemical reactions taking place in Silane plasmas [Mataras 2002, Lyka 2005, Donker 2006] and to understand the effect of the incidental flux of particles on the substrate. Surprisingly, few simulations have been done on the growth of silicon with PECVD. For insulator

thin film layers, a mixture of Tetraethyl orthosilicate (TEOS) and oxygen are typically used as a precursor. Li et al. [Li 1995] studied step coverage with a Monte Carlo simulator in SPEEDIE, whereas Prasada et al [Prasad 2002] used EVOLVE's simulator. Otherwise, simulated surface profiles under CVD and sputtering fluxes are made with Monte Carlo simulation [Pelliccione 2006]. Little attention has been given to the specific problem of simulation of PECVD growth of silicon film in hydrogen-rich environment.

3.7. Definition of voids and cracks

The formation of cracks is relevant to the application of µc-Si:H, as the active photogeneration layer in solar cells. Indeed, for this application, nanotextured substrates are systematically used. Thus, optimization of µc-Si:H must take into account the observed and, after adaptation of the model, the simulated non-dense growth of µc-Si:H layers. In Fig. 3.9, one can see the evolution of µc-Si:H microstructure in the growing layer: Fig. 3.9a shows a TEM cross-section of a dense µc-Si:H p-i-n solar cells, whereas micrograph at Fig. 3.9b shows large voids (white areas) due to the highly textured substrate. For the TEM micrograph in Fig. 3.9c, silicon is dense overall, but a porous zone appears where the substrate present pinches (white lines). Porosity is defined in this thesis as:

- **Voids**: the growing layers contain relatively large empty volumes (voids) that are clearly separated from dense material (like in Fig. 3.9b);

- Initially, **cracks** were thin areas which gave a white contrast in TEM imaging. As described in the next Sections, these turn out to be empty volumes extending over a large scale, and can be composed of nano-voids and more or less dense material (like in Fig. 3.9c).

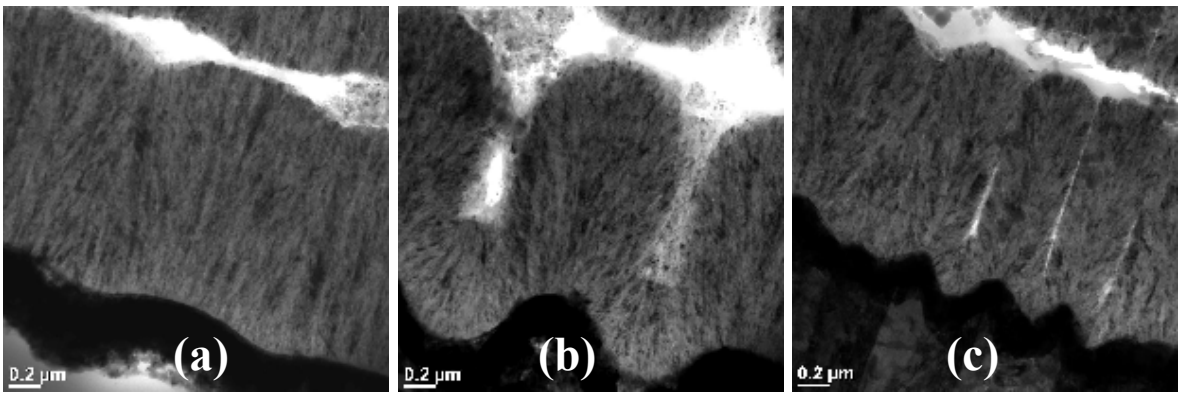

Figure 3.9: TEM micrographs. Influence of the surface morphology on the microcrystalline growth.
(a) Dense µc-Si:H silicon // (b) Voids // (c) Series of cracks.

3.8. Nature of so-called "cracks":

Fig. 3.10a shows a TEM micrograph with cracks (white lines) that cross the µc-Si:H from above the V-shaped valley of the ZnO layer up to the top of the layer. At first approximation, one can think that cracks are missing material at the boundaries of clusters defined by the pyramidal structure of the surface. However, two measurements show that these cracks are not missing material: AFM measurements as seen in Fig. 3.10b and HRTEM in Fig. 3.11.

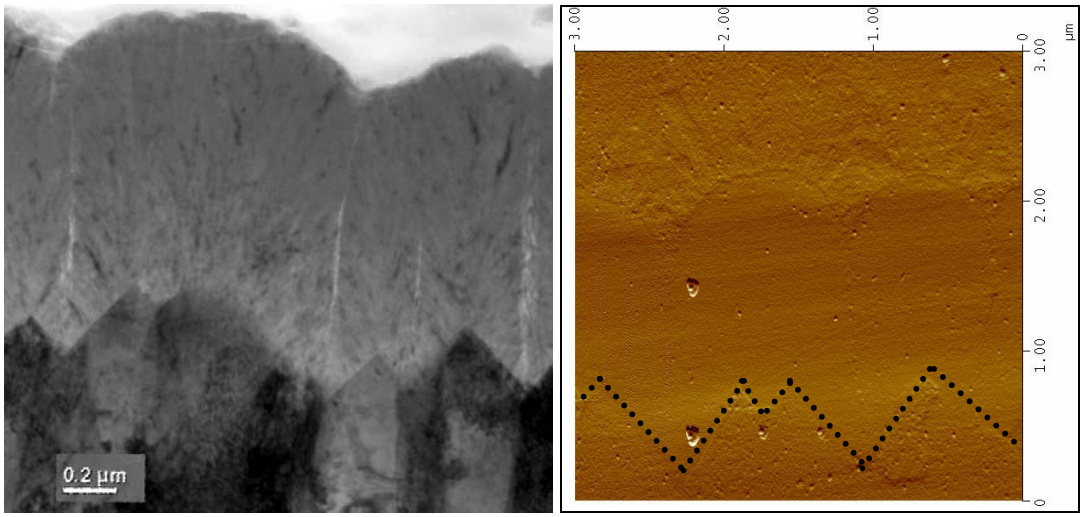

Figure 3.10: (a) Microcrystalline silicon on as-grown ZnO by TEM. The image contrast is enhanced by using slightly under-focused conditions, white Fresnel fringe occurs at the edge of the dense material. (b) AFM amplitude image (tapping mode). The surface shows no trenches in the region of cracks. Dotted lines suggest the interface between the ZnO and the µc-Si:H layers.

Indeed, AFM measurement performed on polished solar cell cross-sections clearly show no trenches at the surface on locations where cracks appear in the corresponding scanning electron microscopy images. Moreover, high resolution TEM micrographs in these cracks show silicon near and above the cracks, as seen in Fig. 3.11. Note that the thickness of this TEM cross-section sample is around 50 nm.

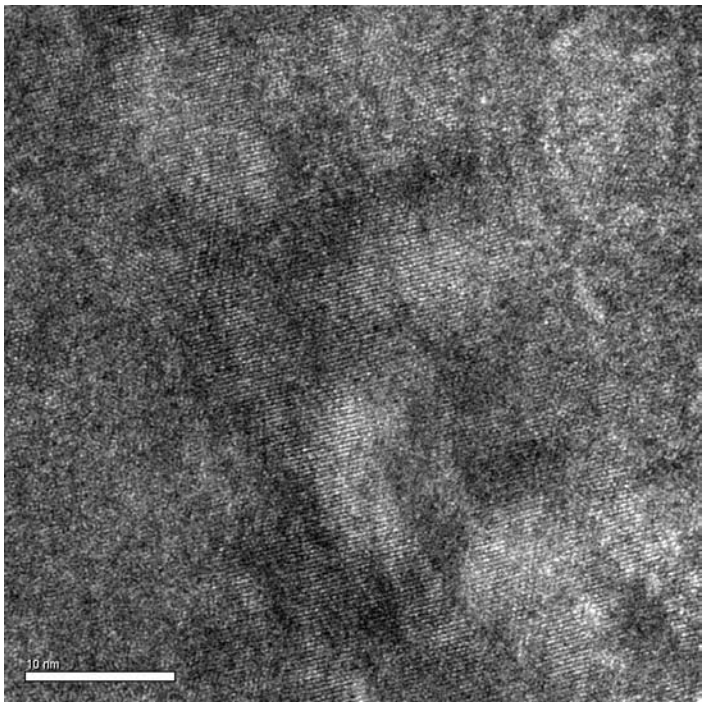

Figure 3.11: HRTEM micrograph of a crack (cross-section thickness 50nm): amorphous materials and "nanograins" are present.

The contrast in the SEM micrograph in Fig. 2.17 is thus explained by assuming a low density material in the region above the V-shaped valley of the ZnO. This contrast is observed with a perpendicular cross-section on electron back-scattered (EBS) and secondary electron (SE) detectors.
SEM micrograph taken with SE detector on tilted sample does not show any contrast (See Fig. 3.12). This image indicates that zones of porous material (cracks) are not located at the surface but are along a plane perpendicular to the surface.

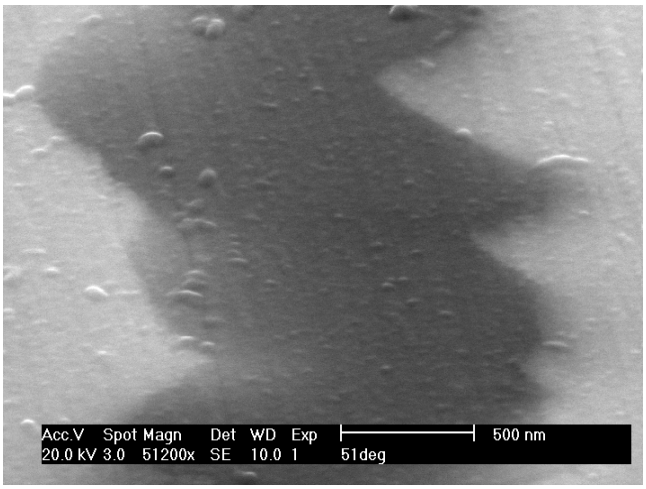

Figure 3.12: SEM on solar cell cross-section tilted at 51° with SE electron microscope. The contrast is no longer observable. Cracks are not "purely" surface feature.

From these observations, cracks are confirmed to be zones of porous, less dense material. SEM micrographs show that the cracks are not linear but 2D-like zones. This observation leads one to assume that cracks are zones of porous material all around the perimeter of the base of the pyramidal structures in the ZnO. The width of these voids is less than 50 nm, because no lack of material was observed in HRTEM micrographs (prepared from Focused ion beam (FIB) method)

3.9. Influence of cracks on oxygen content

In order to analyze the concentration of impurities linked to the cracks, a comparison between a solar cell with a high number of cracks (deposited on ZnO treated for 20 minutes) and less cracks (deposited on ZnO treated for 40 minutes) was performed. Secondary ion mass spectroscopy (SIMS) measurements show that the cell with more cracks contains more oxygen (Fig. 3.13)

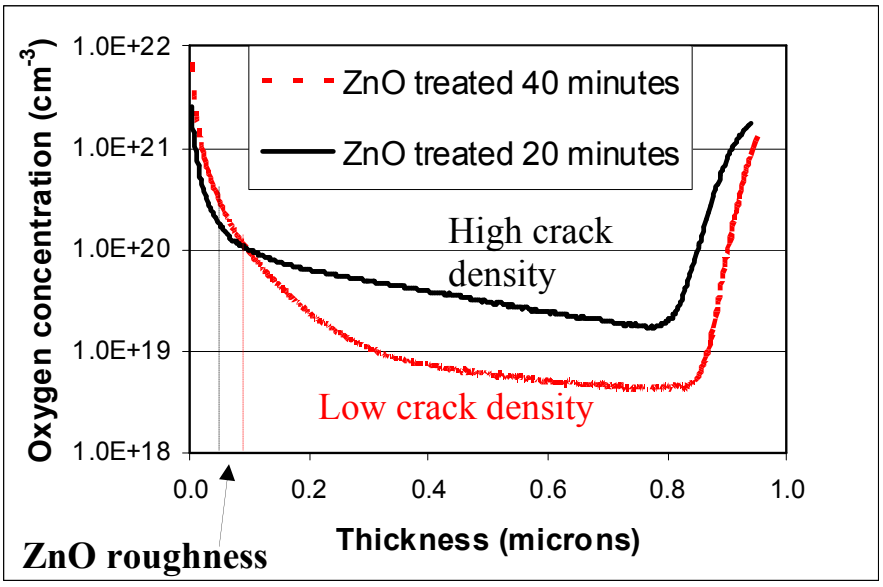

Figure 3.13: SIMS measurements of µc-Si:H solar cell deposited on various TCO's surface morphologies. The black line is the measurement for a solar cell containing more cracks than the cell represented by the dotted line. Courtesy Xavier Niquille and Thomas Söderström.

The Fig. 3.13 shows that the oxygen concentration depends on the surface morphology of the substrate (here ZnO). Moreover, the beginning of the SIMS measurement (end of silicon growth) contains more oxygen than the end of the measurement (beginning of the growth). This effect is seen by the slope of the measurement (typically with the black line).

A new method to characterize this effect has been performed. The experiment, called nano-SIMS, permits to map the concentration of oxygen with nanometrical spot size of analysis. The method "1 face polishing", presented in Section 2.11.2 has been used to prepare the sample for this experiment. The Fig 3.14 shows the concentration of oxygen on the cross section of the sample. The red zones are saturated signal of oxygen due to ZnO layers. The yellow part is the silicon. Note that the interface between the ZnO layer and the silicon layer appears as orange, due to the size of the spot and the thickness of the sample. Other zones appear orange, in the silicon layer: zone of cracks. This results shows that oxygen is present in zone of cracks and suggest that cracks are responsible for post-oxidation of the cell.

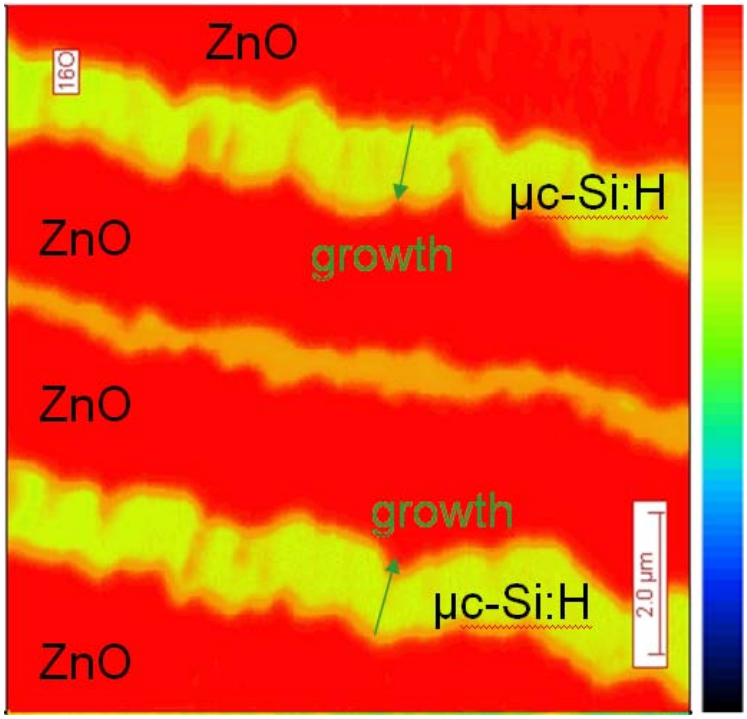

Figure 3.14: Nano-SIMS measurements of µc-Si:H solar cell cross-section deposited on non-treated ZnO. The preparation is done with "1 face polishing" method.

Thus, we assume that cracks are zones of porous material that contain oxygen. The oxygen is probably due to post oxidation of the cell, because the deposition is performed with the help of a purifier [Torres 1996]. In Chapter 7, a new equivalent electrical circuit is proposed in order to include these cracks in the model.

4. Microcrystalline silicon growth with PECVD on a structured substrate

4.1. Introduction

Microcrystalline silicon exhibits a complex microstructure composed of nanocrystals in an amorphous matrix [Vallat-Sauvain 2000, Luysberg 2001, Vetterl 2000] plus voids/cracks (see previous discussion in Chapter 1). Cracks have been first observed in amorphous silicon for solar cells [Sakai 1989 and 1990, Löffler 2005] and in a-Si:H deposited on CMOS used as detectors of particles [Miazza 2004, Despeisse 2008]. For microcrystalline silicon solar cells, cracks have been observed by many authors [Luysberg 1997, Goerlitzer 1998, Houben 1998, Shah 2002, Graf 2003, Li 2008] but no direct relationship has been made with electrical performances.

In order to further improve the efficiency of thin film microcrystalline solar cells, a better understanding of the present limitations of material quality for the device's performance is necessary. The dependence of their performance on the crystalline volume fraction of the i-layer material is fairly well documented [Klein 2007, Droz 2004], but the role of the voids/cracks on the electrical properties of the device warranted further investigation [Smets 2008, Python 2008].

The μc-Si:H microstructure depends on the substrate's chemical nature [Vallat-Sauvain 2005], but also on its surface morphology. Nasuno et al. [Nasuno 2001] have established the relationship between μc-Si:H solar cell performance and surface morphology of the substrate in terms of average slope of substrate surface textures. A recent work [Bailat 2006] has shown that a post-treatment of the transparent conductive oxide (TCO) that modifies the surface morphology from V-shaped to U-shaped before the deposition of the μc-Si:H solar cell, improves the electrical device's performance of the deposited cells. V- or U-shaped corresponds to the shape of the bottom of the valley of the pyramids. The assumption was that silicon growth on a V-shaped surface leads to the creation of "cracks", i.e. zones of porous material (see Section 3.7). In relationship with this observations, we will show that these "cracks" can be considered, in the device equivalent electrical circuit previously introduced in Chapter 2, as a "bad parallel diode" (see Chapter 7) and can be held mostly responsible for the decrease of the electrical performances observed with too rough substrates (low open-circuit voltage, low fill factor).

In order to confirm and further highlight the detrimental role of cracks on single-junction microcrystalline solar cells, a series of V- to U-shaped type of substrate is used here. Wafers with so-called random pyramids, exhibiting V-shaped areas between the pyramids, are tested. The curvature radii at the bottom of the

pyramids can be continuously varied by chemical etching. An analysis of the electrical performances of the solar cells as a function of the curvature radii of the pyramids valleys confirms that, with all other parameters kept unchanged, U-shaped substrates yield to devices with increased electrical performances. This effect is further highlighted on a large set of various commercial and R&D TCO's: Asahi U (SnO_2:F), "sputtered and etched" zinc oxide (ZnO) [Müller 2001] as well as Low-pressure chemical vapor deposited ZnO (LP-CVD) (w and w/o post-treatment to modify the surface morphology).

4.2. Experimental procedure

Single-junction μc-Si:H thin film solar cells were deposited at 200°C at 40 MHz excitation frequency by plasma-enhanced chemical vapor deposition (PECVD) in a modified KAI-S plasma-box reactor from Oerlikon-Solar AG. The deposition of μc-Si:H was performed in one run in the p-i-n configuration on a load of wafer substrates with random pyramids (called hereafter pyramidal wafers) and various transparent (Glass/TCO) substrates.

The following substrates were used:

- Pyramidally-textured monocrystalline silicon cz wafers
- Glass/LP-CVD ZnO substrates
- Glass/Asahi U substrates
- Glass/sputtered-etched ZnO substrates

A series of V- to U-shaped pyramidal etched wafer substrates were prepared by chemical etching in a CP133 solution, which consists of a mixture of HF:CH3COOH:HNO3 (1:3:3) with increasing treatment time. Silver (50 nm thick sputtered at room temperature) and sputtered aluminum-doped ZnO (50 nm) were deposited as conductive contact layer stacks on the initial and treated wafers. The surface morphology of the substrates investigated by SEM is presented in Fig. 4.1. The as-received pyramidal wafer showed pyramids with small structures between the main pyramids (Fig. 4.1a). The smoothing treatment performed on the pyramidal wafer first eliminated the small structure and second transformed the V-shaped valley at the bottoms of the pyramids into U-shaped valleys (see Fig. 4.1a to 4.1c).

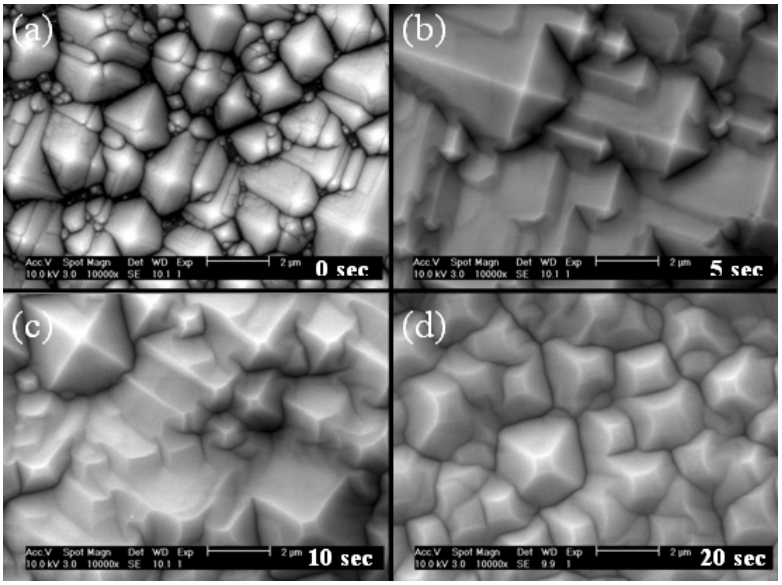

Figure 4.1: SEM micrographs (magnification = 10 000 x) of as-received wafer with random pyramids (top left) and after $HF/HNO_3/CH_3COOH$ smoothing treatment: top right: 5 second treatment, bottom left: 10 seconds, bottom right: 20 seconds.

The glass/LP-CVD ZnO substrates [Faÿ 2006] were prepared by depositing a ~4 µm thick LPCVD-ZnO layer, from a vapor-gas mixture of water, diethyl-zinc and diborane, on AF45 glass substrates from Schott. The surface morphology was subsequently modified by applying a plasma treatment to the ZnO layers [Bailat 2006]. The variation of the duration of this treatment allowed for morphology modifications ranging from a V-shaped (initial) morphology to a U-shaped one, with long treatment (Fig. 4.2a and 4.2b).

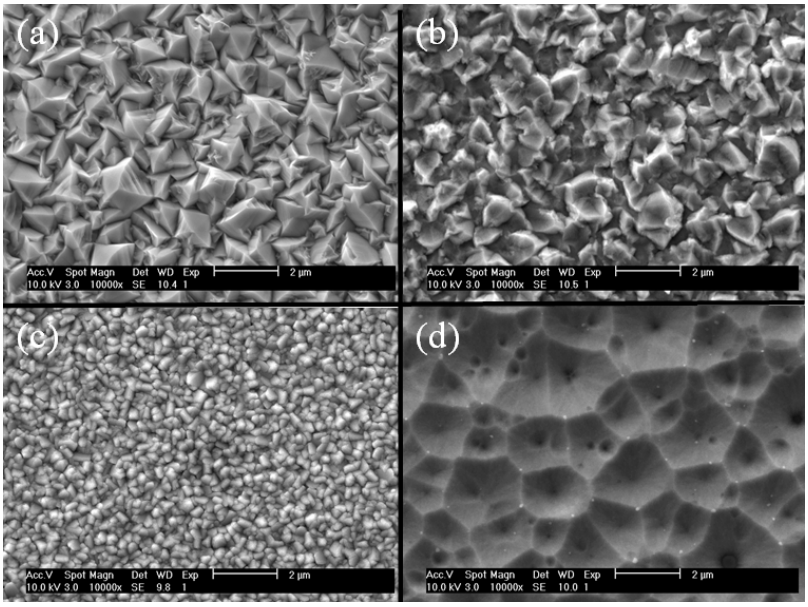

Figure 4.2: Plane-view SEM micrographs (magnification = 10 000x) of glass/TCO based substrates: top left: LPCVD-ZnO, top right: LPCVD-ZnO with 60 minutes of plasma treatment [Bailat 2006], bottom left: Asahi U, bottom right: sputtered and etched ZnO.

The glass/Asahi U substrate was commercially purchased (Fig. 4.2c) and the glass/sputtered-etched ZnO substrate was obtained from Forschungszentrum Jülich, Germany (Fig. 4.2d).
Before the µc-Si:H deposition, the substrates were characterized by scanning electron microscopy (SEM) and after fabrication of the µc-Si:H device, the LP-CVD ZnO back contact was structured by a lift-off procedure to produce solar cells having an area of 0.25 cm^2. TEM cross-sections of one solar cell per substrate were prepared by cutting, wedge polishing and ion milling with the method presented in [Benedict 1992]. The current density-voltage (J(V)) curves were measured, with the n-layer on the illumination side for cells on the wafer.
Note that the same magnification (and then same scale) is used for the 8 micrographs presented in Fig. 4.1 and 4.2.

4.3. Results

We will first present the effect of the pyramidal wafer's morphology on the V_{oc} and FF of single junction p-i-n µc-Si:H solar cells, whereas in the second part, the effect of various substrate morphologies as obtained from common glass/TCO (LPCVD ZnO, Asahi, "sputtered and etched" ZnO) will be presented. Comparisons of numerical simulations with the experimental observations will be detailed in Chapter 5.

4.3.1. Effect of pyramidal morphologies on the electrical parameters

The surface morphology of the substrate was presented in Fig. 4.1 with SEM micrograph. TEM cross-sections are performed on solar cells, co-deposited (same run) on such substrates. The TEM cross-sections of Fig. 4.3 show that the radius of curvature typically changes from 20 nm to 500 nm after the treatment and corresponds to substrates in Fig. 4.1a and 4.1d, respectively.

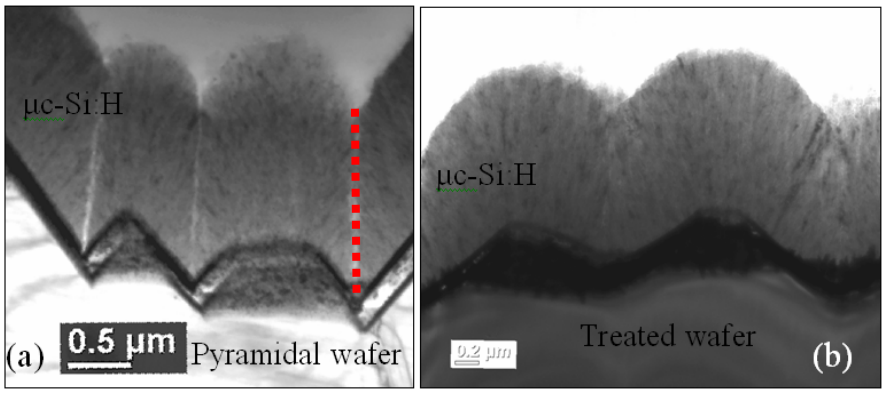

Figure 4.3: TEM micrograph cross-section of a single-junction p-i-n solar cell deposited on a pyramidal wafer substrate. On the left, the V-shaped valleys of the substrate result

in cracks crossing the whole p-i-n device (light area). On the right, the U-shaped substrate valley results in a denser microstructure.

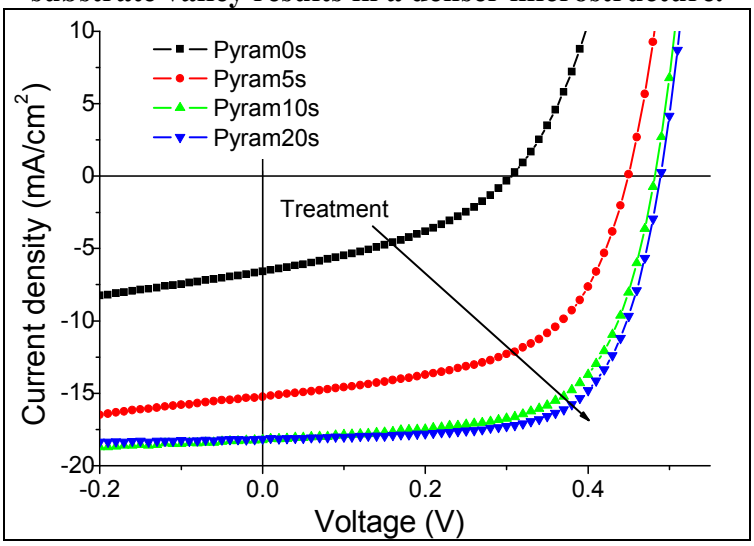

Figure 4.4: J(V) curves of thin film p-i-n microcrystalline silicon solar cells co-deposited on pyramidal wafer substrates as a function of smoothing treatment ($HF/HNO_3/CH_3COOH$) time. Here cells are exceptionally illuminated from the n-side.

The electrical results (Fig. 4.4 and 4.5) confirm an increase of both V_{oc} and FF (from 0.32 to 0.49 V and 42% to 68%, respectively) as a function of smoothing treatment time for co-deposited p-i-n µc-Si:H cells, such as observed in [Bailat 2006]. The origin of such an increase in electrical performances will be described in more detail in Chapter 7.

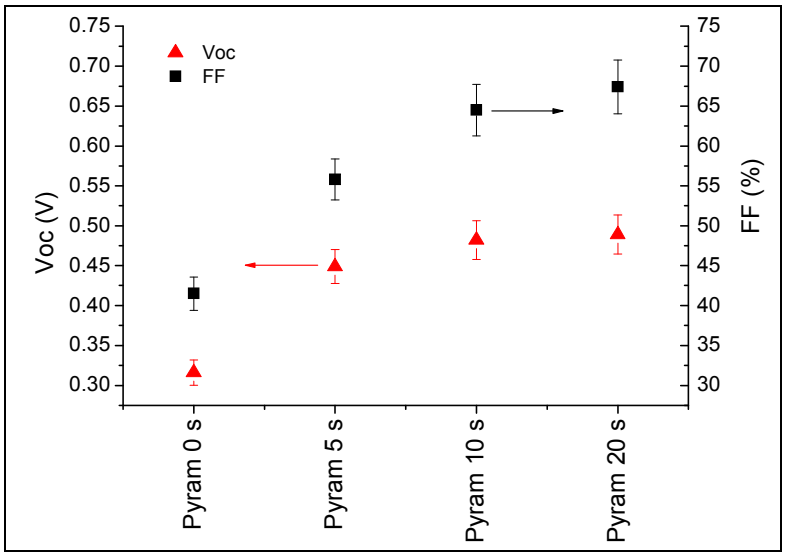

Figure 4.5: V_{oc} and FF of thin film p-i-n microcrystalline silicon solar cells co-deposited on pyramidal wafer substrates as a function of smoothing treatment ($HF/HNO_3/CH_3COOH$) time. Here cells are exceptionally illuminated from the n-side.

4.3.2. Effect of TCO

Here, p-i-n single junction solar cells were co-deposited (same run as for wafer substrate) on different TCO's with various morphologies, as shown by the SEM micrographs in Fig. 4.2. The electrical performances of the corresponding devices are given in Fig. 4.6.

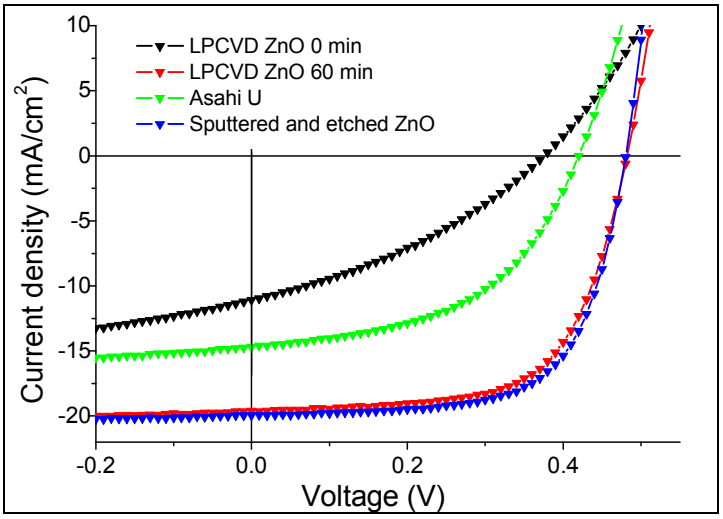

Figure 4.6: J(V) curves of thin film p-i-n microcrystalline silicon solar cells co-deposited on glass substrates.

Again, we observe low V_{oc} and FF values (0.38 V and 34%, respectively) for the cells deposited on non-treated, rough LPCVD ZnO. With a smoothing post-treatment, it is possible to considerably improve the electrical performances (V_{oc} = 0.48 V and FF ~ 65 %).

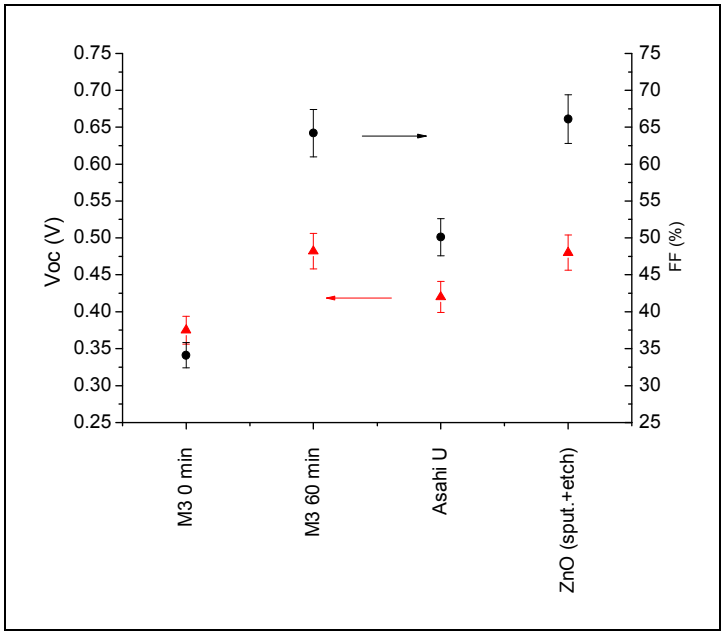

Figure 4.7: Triangle: V_{oc}, dots: FF of p-i-n microcrystalline silicon solar cells on various deposited TCOs. M3 means LPCVD ZnO, the time is the treatment time.

We observe that lower performances are also obtained for the p-i-n μc-Si:H cell deposited on Asahi U. This TCO possesses a fine surface structure, which seems inadequate for our μc-Si:H cell (which is specially optimized for plasma treated LP-CVD ZnO), as it results in a high density of cracks at the beginning of growth. Finally, the "sputtered and etched" ZnO shows the same properties as the treated LPCVD ZnO. The morphology is U-shaped, and silicon solar cells have drastically fewer cracks, as reported in [Python 2008].

4.4. Discussion

The observed continuous improvement of V_{oc} and FF for p-i-n on smoothed pyramidal wafers confirms the results obtained previously on smoothed TCO's [Bailat 2006] and leads to conclusions similar to Nasuno et al. [Nasuno 2001]: the morphology of the substrate affects the electrical performances of single-junction μc-Si:H solar cells. In contrast to the work of Nasuno in which the substrate angle was the sole critical factor, the curvature radii at the valley between the pyramids is also considered here to be critical for an improvement of the solar cell's performance (see Chapter 5). The U-shaped morphology of the substrate gives better electrical performances of μc-Si:H solar cells compared to substrates with V-shaped pyramids, even for similar opening angles. Indeed, TEM micrographs show a decrease in the density of cracks in the solar cells with the U-shaped modification of the substrate. Compared to previous studies, performed on nanotextured TCO only with typical lateral dimension in the range of 300-500 nm [Python 2008], we find that wafers with pyramidal structures in the micron range lead to similar effects.
Hence we postulate that for most useful structure dimensions from 300 nm to several microns, the detrimental effect of V-shaped valley bottoms occurs. The small structures between the pyramids in the non-treated wafer are also at least partly responsible for the bad electrical performances, because the V_{oc} and FF increase after the treatment. These results confirm the influence of the morphology of the substrate on the cell performances, as described in the case of LPCVD ZnO in [Bailat 2006, Python 2008]. Finally, we should point out that, even on a difficult substrate, it is also possible to achieve reasonable efficiency, usually by working on the PECVD process. The best results (efficiencies in the range of 7-8 %) are however not comparable with the best cells achievable on a substrate having a suitable morphology (efficiencies in the range of 9-10 %).

4.5. Conclusion

Three features of the substrate morphology lead to a decreased crack density:

1) More uniform, controlled size distribution on rough substrate.
2) Smoothed substrate's valley from V-shaped to U-shaped.
3) Lower pyramid's angle, as will be demonstrated in Chapter 5

With the results of these experiments, the morphology of the substrate for μc-Si:H can be optimized in order to reduce the crack density. However, the light scattering is a function of this morphology, and a rough substrate is necessary for high current in the resulting solar cells. Therefore, the ideal substrate would possess high roughness with curvature radii higher than 200-300 nm (and without small-sized structures between large-size pyramids).

5. MANEMO simulation program and comparison with experiments

5.1. Introduction

This Chapter is focused on the modeling of microcrystalline silicon growth with the numerical program, "maximization of neighbor's model" MANEMO, developed in the framework of this thesis. This 3D discrete growth model is based on the approach proposed by Bailat et al. [Bailat 2004]. The growth of μc-Si:H is typically performed in a Plasma-Enhanced chemical vapor deposition (PECVD) regime and the suspected microscopic growth mechanisms are translated into a computer language called the selection rules.
In this program, already described briefly in Chapter 3, a particle is released from a position randomly chosen above the surface. Each particle represents the statistical average behavior of a large number of atoms/molecules. The particle follows a vertical or oblique trajectory in a cubic lattice (up to 512 x 512 x 512) until it reaches the growing surface. After random deposition the particle finds the best position by diffusion and takes a variable (a color or grey level) representing its crystallographic orientation. The resulting simulation yields a 3D layer microstructure (as presented in Fig. 5.1) from which cross-sectional views are generated. The combination of particles with random incidence and substrate morphology result in diffusion and shadowing effects that are demonstrated to play an important role for the nucleation and growth of the microcrystalline phase.

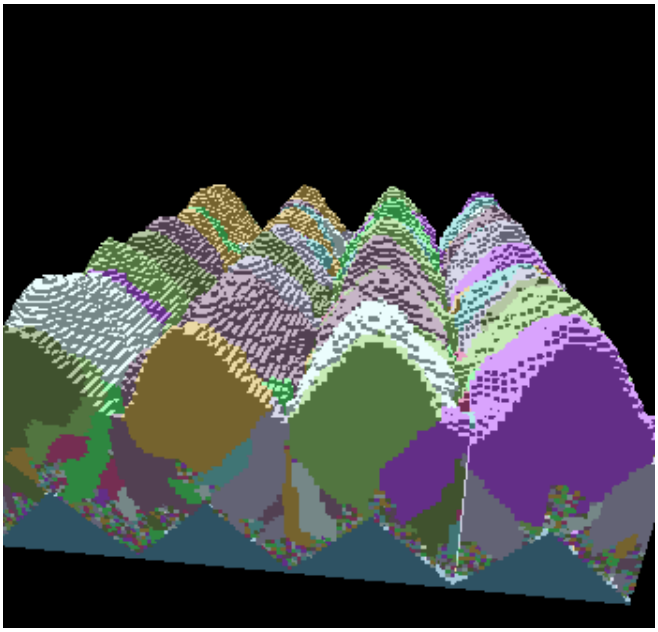

Figure 5.1: 3D simulation model (MANEMO) for a pyramidal linear substrate.

Simulations will be typically compared with transmission electron microscopy (TEM) micrographs of μc-Si:H layers. The comparison between simulated and real μc-Si:H microstructures will allow us to clarify major aspects of the growth mechanisms of microcrystalline silicon and give insight into the generation of micro-cracks in the layer. These cracks are generally formed on the top of the lowest points of the textured substrates (valleys), both in the modeling and in the TEM cross-sections of the films, as previously discussed in Chapter 4.

The simulation program uses several rules that are linked to physical models. There are three major models that explain the growth of hydrogenated microcrystalline silicon [Matsuda 1999, Strahm 2007]:

1) Surface diffusion model [Matsuda 1983]
2) Selective etching model [Tsai 1989]
3) Chemical annealing model [Nakamura 1995]

(1) The surface diffusion model takes into account the diffusion coefficient on the hydrogen-covered surface that is modified by the substrate temperature and the presence of hydrogen allowing the precursors to reach favorable sites. This model can also explain the decrease of cracks observed when the temperature of the substrate increases, as will be detailed in Chapter 8.

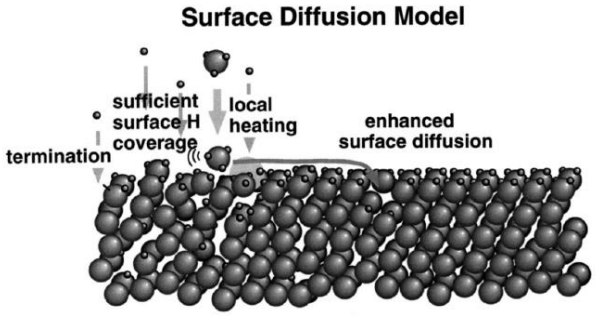

Figure 5.2: Surface diffusion model (from [Matsuda 1999]).

(2) The etching model justifies the increase in the crystalline volume fraction with the increase in the hydrogen dilution by the role of atomic hydrogen on breaking Si-Si bonds. Weaker bonds are preferentially broken, which leads to higher crystallinity of the growing μc-Si:H layer.

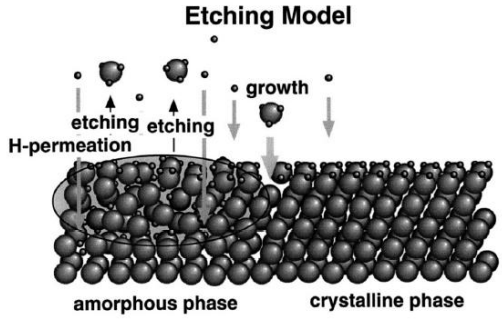

Figure 5.3: Etching model (from [Matsuda 1999]).

(3) The chemical annealing model explains that the hydrogen atoms enter in the sub-surface region giving rise to a crystallization of amorphous network without any etching process of Si atoms. This process also explains the increase in crystallinity in function of the increase in hydrogen during the deposition.

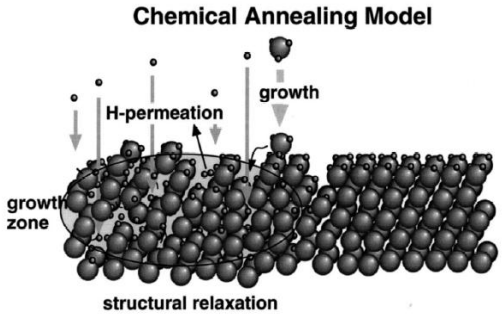

Figure 5.4: Chemical annealing model (from [Matsuda 1999]).

As demonstrated by Strahm [Strahm 2007], the 3 models are necessary to explain the growth of microcrystalline silicon layers.
In the former simulation software, developed by Bailat et al. [Bailat 2004] the transition between the growth of amorphous and microcrystalline silicon is explained with the preferential etching of the amorphous silicon, like in the etching model. Indeed, Bailat et al. have demonstrated that by increasing the etching process during the growth, the crystallinity increase [Bailat 2004b]. Nevertheless, due to the limitation to normal incidence of incoming particles (particles falls vertically) and relaxation procedure (i.e. particles do not interact with other particles at the surface), the software was not able to study the apparition of cracks during the growth. In order to improve the software, two aspects have thus been modified:

a) A combination of isotropic and vertical incidence. Indeed, the main precursors are neutral in PECVD deposition processes used for μc-Si:H fabrication [Strahm 2007], and thus their distribution of incidence angles follows an isotropic distribution function.

b) A surface diffusion process (instead of local relaxation), as discussed in "surface diffusion model (1)". It is assumed here that the driving force of growth is the maximization of neighbors rather than just local relaxation.

5.2. Numerical simulation

The MANEMO software was developed on a Mac G5 with dual 1.8 GHz PowerPC processors. The window user's interface allows the definition of the following model parameters: (i) total layer thickness, (ii) number of states (i.e. crystalline orientation given by a color or a grey level), (iii) neighborhood threshold value, (iv) maximum number of diffusion steps, as well as (v) desorption parameters. Our numerical simulation is composed of five sequential steps; new features as compared to the original software version [Bailat 2004] are indicated with an *:

1) **Generation and incidence path of the particles**:

a. A particle is randomly generated on a virtual plane at a fixed height above the substrate.
b. * A chosen percentage of particles has an incidence angle generated in such a way as to follow an isotropic probability distribution (oblique trajectory) to model the neutral incoming particles. The other particles have a vertical trajectory towards the substrate (for ionized particles).
c. The impinging site for deposition is determined at the place where the particle collides with the substrate or growing layer (temporary position).

2) *** Diffusion**:

After reaching the impinging position, the particle can move at the surface by diffusion. With this process, the particle tends to maximize the number of neighbors and, thus, to minimize bounding energy, as described in the surface diffusion model [Matsuda 1999, Strahm 2007]

a. At the impinging position, the neighborhood is characterized by calculating the total number of neighbors (i.e. the number of particles directly surrounding the incoming one). This value is taken as the reference.
b. The same calculation is performed for the 26 direct positions around the impinging position (cube of 3 x 3 x 3 positions minus the impinging one: 9 below, 8 around and 9 above). If one position contains more neighbor particles than the reference calculated in the

step 2a, then, the particle diffuse to this position. In case of equality over several positions, a random position is chosen between the equal positions.

c. Step 2b is repeated the number of times chosen by the user with the variable (iv): “maximum number of diffusion steps”.

3) ***Lateral sticking:**

a. As already mentioned, the incoming particle can follow either a normal or an oblique incidence [Python 2006]. The combination between the surface morphology and the oblique incidence leads to shadowing (and thus cracks or voids). The simulated microstructure, generated in case of a normal incidence of incoming particles only, consists in a fully dense material (see comparison on Fig. 5.6).

4) **Choice of the crystalline orientation (color or grey level)**:

a. The state “color” of the 26 possible neighbors around the final position is characterized, and the dominant state, if any, is determined.
b. If the number of particles in the dominant state is higher than the chosen variable (iii) “neighborhood threshold value”, the incoming particle takes the dominant state variable. Otherwise, the state is randomly set to one of the possible number of state variables (ii).

5) **Desorption**:

a. After deposition, the particle can be removed under certain circumstances. The probability for such a mechanism to occur depends on the number of neighbors in the same state than the incoming particle and the variable (v) “desorption parameters”. If the former is lower than “desorption parameters”, then the particle has a non-null probability to be desorbed. This selection rule corresponds to the etching model previously described.

5.3. Cracks and voids

In order to study the effect of the substrate surface morphology on μc-Si:H growth, two different rough substrates have been characterized by atomic force microscopy (AFM) and directly implemented in the MANEMO program. Both substrates consist of:

a) A periodic substrate composed of a stack of photo-curable glue, (nanotextured by UV embossing) / Cr / Ag / Sputtered ZnO thin layers (see AFM picture in Fig. 5.5a). Further details on this substrate can be found in [Sharf 2004].
b) A random nanotextured substrate composed of a stack of LP-CVD ZnO / Cr / Ag / sputtered ZnO thin layer (Fig. 5.5b).

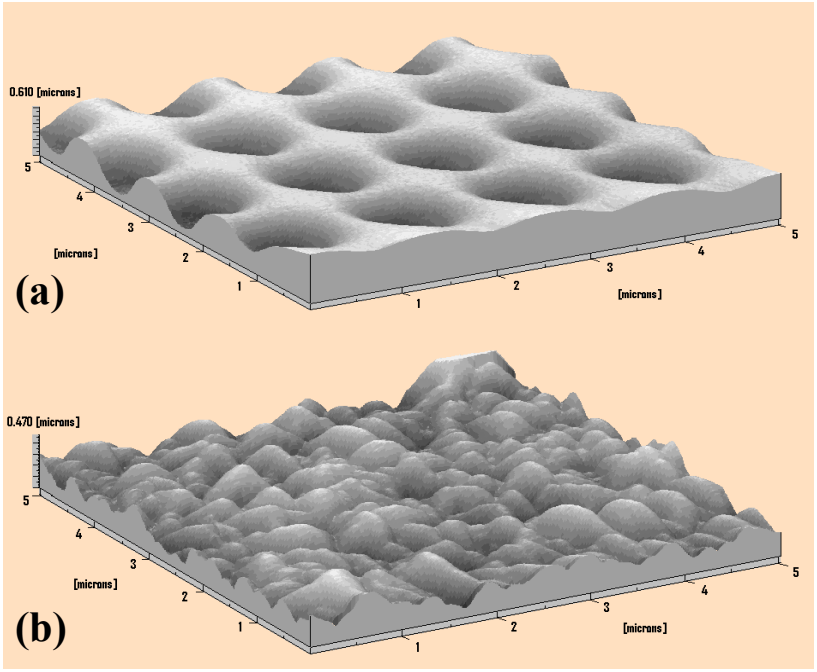

Figure 5.5: AFM non-contact surface topography. Scanned surface: 5x5 µm. (a) Periodic structure, rms = 139 nm, (b) Random structure, rms = 72 nm.

Care was taken to have substrates with the same surface chemistry (sputtered ZnO), as the nucleation of µc-Si:H can critically depend on the substrate's chemistry, as demonstrated by [Vallat-Sauvain 2005].
The two substrates used in this work have characteristic feature size (root mean square roughness (rms)) of the order of 100 nm as typically used for efficient light trapping in µc-Si:H solar cells. Microcrystalline layers were then co-deposited on these substrates by using a highly diluted gas phase mixture of silane and hydrogen (SC = $[SiH_4]/[SiH_4 + H_2] \cong$ 2 %) by VHF-PECVD at 200 °C, with a plasma excitation frequency of 110 MHz.
The layers were prepared for TEM cross-sectional examination by means of the tripod method. TEM bright-field, medium-resolution micrographs (see Fig. 5.6 left column) were obtained with a Philips CM200 microscope operated at 200 kV, and equipped with a digital camera.
On the periodic substrate, two cross-sections were studied: the first one was obtained on a section where the substrate height modulation is small (i.e. "far" from the holes in the substrates"), thus rendering the effect of a smooth, almost flat substrate. The second one was obtained on a section where the substrate height modulation is pronounced (i.e. "through" the holes in the substrate).

5.4. MANEMO and transmission electron microscopy (TEM): Comparison and discussion

Fig. 5.6 left column shows the TEM cross-sections of the µc-Si:H layer on both nanotextured substrates. Voids and cracks (see Chapter 3 for more details about cracks) appear white. Within the microcrystalline phase the amorphous silicon appears grey, whereas the darker regions are due to the diffraction contrast of nanocrystals. In these µc-Si:H layers, conglomerates of nanocrystallites constitute large conical grains, such as previously described in Chapter 1. Simulated crystalline domains are representations of these grains (conglomerates). The main variation between the microstructures originating from the different substrate topographies is the presence of thin cracks or voids in layers grown on rough substrate (see TEM micrograph 5.6(2a) and (3a)) as compared to flatter substrate (5.6(1a)).

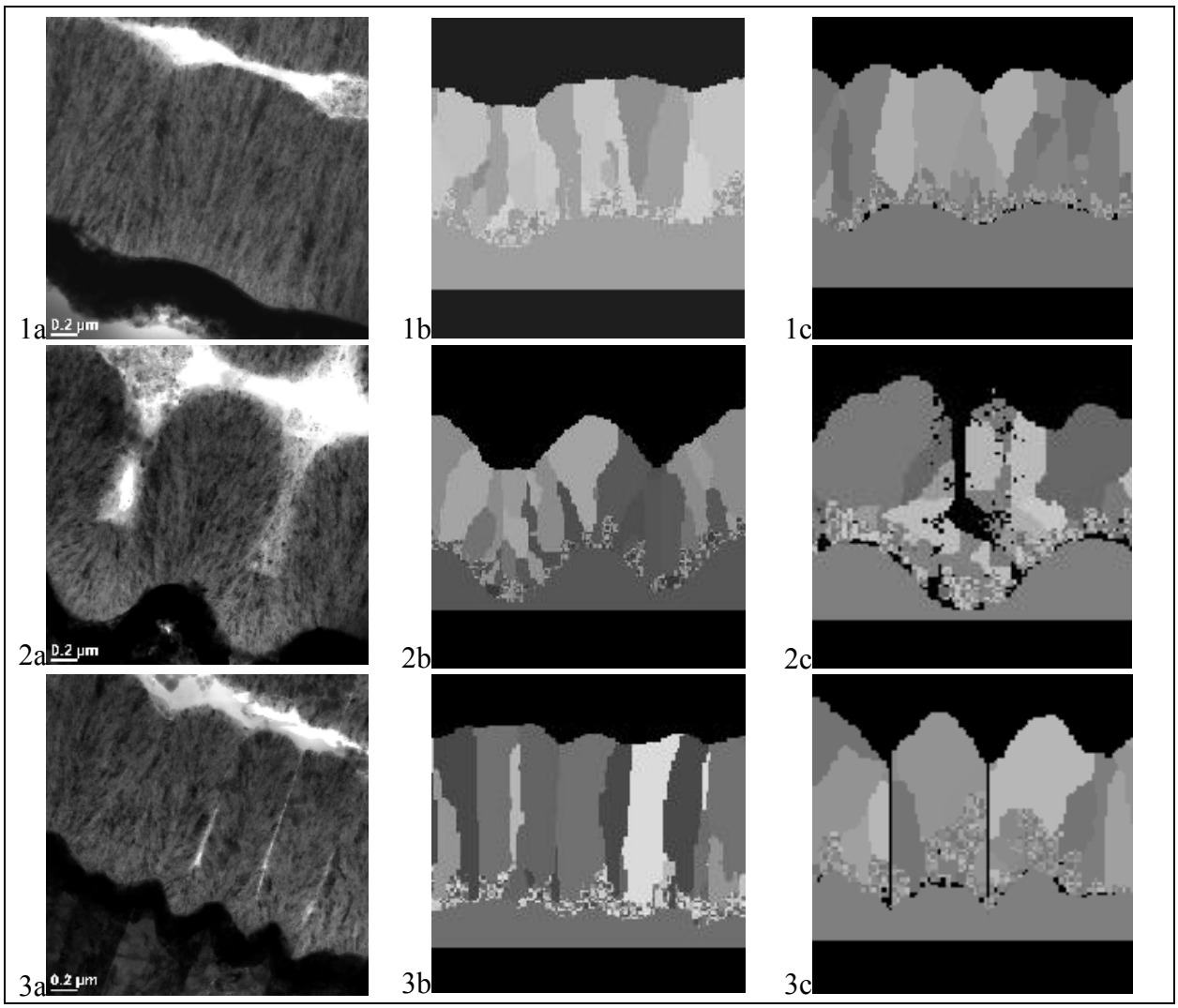

Figure 5.6: Left column: Bright field TEM micrographs of µc-Si:H layers, middle column: Cross-section of simulation with normal incidence, right column: Cross-section of simulation with isotropic incidence / the two first rows: periodic substrate, bottom row: random substrate.

Fig. 5.6 middle column shows the simulated cross-section obtained when using normal incidence of particles only. The simulated growing surface is conformal (see definition in Chapter 3) to the substrate surface without any cracks. The growth of crystalline grains has a columnar shape as discussed in Bailat's thesis [Bailat 2004], like that observed in the TEM micrograph (compare micrograph 5.6 (1b) with (1a)).
The right column shows the simulated cross-sections obtained when an isotropic distribution of incident angles is considered. The simulated layers present a higher roughness than the previous two cases (experiment and simulation with normal incidence), and a less pronounced columnar growth, but cracks and voids appear. In our simulations, voids appear at the bottom of substrate's valley (or pinches), like in the corresponding TEM micrograph in Fig. 5.6 (2a).
The use of normal incidence without lateral sticking did not allow the occurrence of voids/cracks in the simulated microstructure, which was then fully dense (see Fig. 5.6: middle column). The presence or absence of cracks within the μc-Si:H layer (depending on the substrate's topography) is thus a salient difference. It also occurs in our TEM observations, and needed to be reproduced by the numerical simulations.
This could be done by introducing isotropic incidence of particles and lateral sticking in our numerical simulations (see Fig. 5.6 (3c)). It is seen in Chapter 4 that these cracks influence the electrical performances and the μc-Si:H layer's material properties.
The introduction of complementary features in the program thus allows predicting the appearance of cracks and voids. The formation of cracks is relevant for the application of μc-Si:H as the active photogeneration layer in solar cells. Indeed, for this application, nanotextured substrates are systematically used. Thus, the optical optimization of such devices should take into account the observed and, after adaptation of the model, the simulated non-conformal growth of μc-Si:H layers. The occurrence of cracks within the μc-Si:H layer related with shadowing effects of the substrate should also be taken into account for the optimization of the electrical parameters of the device. A more complete analysis of this effect of cracks on the electrical parameters will be presented in Chapter 7 of this thesis, based on the equivalent electrical circuit.

5.5. Quantification of crack density in simulation

In order to evaluate the simulated crack density in the growing layer, a new algorithm was programmed as follows: the number of cracks is defined by each group of missing columns in the growing layer, missing columns representing porous material. According to this simple representation, we can not in principle

distinguish between voids and porous material. Nevertheless, for this modeling program, we assume that a few missing columns are cracks and large groups of missing columns (compared to the typical size of the conglomerate) are voids.

5.5.1. Quantification of missing columns

The first step is to find every column that is empty. It is performed by adding a virtual horizontal plane above the substrate and assuming that a missing column is a column without particle below this plane. The position of this latter is not trivial. Indeed, the plane should be as high as possible in order to count the maximum of cracks (because cracks can begin at the bottom of the valley, in the middle of the growth as well as at the end of the growth) but not too high because of the roughness of the growing layer as seen in Fig. 5.7. The position of this plane is thus fixed just above the substrate's highest peak.

For the simulation in Fig. 5.7, the input parameters are:

(i) total layer thickness 75
(ii) number of states 10
(iii) neighborhood threshold value 4
(iv) maximum number of diffusion steps 10
(v) desorption parameters 30

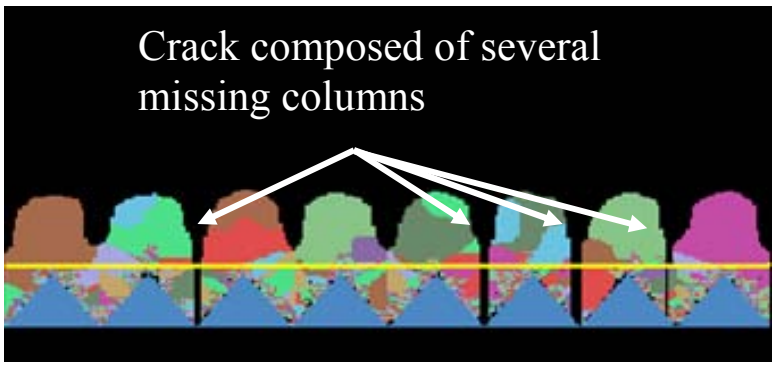

Figure 5.7: Example of simulated silicon growth on a pyramidal substrate. The line represents the position of the virtual plane defined above.

Counting missing columns is easy, because the program knows exactly the position of every cube of the deposition. Thus, if a column contains fewer particles than the height of the virtual fixed plane (represented by a line in Fig. 5.7), the column is defined as a missing column. Cracks can be composed of single missing columns or of a multitude of contiguously grouped missing columns. A procedure is thus needed to determine the crack density, as described here.

5.5.2. Algorithm to quantify cracks with missing columns

If one takes a square flat substrate with a width of 9 sites, one obtains 81 possible deposition sites. The modeling program MANEMO will deposit several particles (cubes) on this flat substrate. At the end of the modeling, a layer will have grown on this 9x9 flat substrate (3D layer). We shall consider the example in the Fig. 5.8:

71	72	73	69	67	68	67	70	72
70	3	0	70	68	3	4	71	70
69	2	1	2	69	1	2	70	69
68	66	2	71	67	68	69	0	68
67	65	3	69	68	67	3	72	67
69	70	69	68	66	66	74	73	69
70	71	69	4	3	2	75	73	70
72	72	68	70	71	72	73	5	72
71	72	73	69	67	68	67	70	72

Figure 5.8: Example of a square substrate with width of 9 sites after deposition. The values represent the height of the column, i.e. number of cubes (sum of substrate and growing layer).

Each number within the possible sites represents the height of the substrate plus the deposited layer for the specific site. For example, on the first possible site in Fig. 5.8, a total number of 71 cubes are piled up (column of 71 cubes). In such a case, and by assuming that each column of height below 50 (vertical position of the virtual plane in Fig. 5.7) is a missing column, one obtains 17 missing columns (in grey or color in Fig. 5.8).
The algorithm described here is able to distinguish the 4 cracks (composed of grouped missing columns), represented by the different colors of the missing columns in Fig. 5.8. Indeed, the algorithm considers the first value below 50 and groups its neighbors:

1) The algorithm changes all values lower than threshold (= 50 in this example) to “5” (arbitrary value), the other values change to “2” (Fig. 5.9a) in order to distinguish the missing columns to others.
2) Then, the first “5” is founded by scanning the 81 possible sites of the substrate and the value is changed to “7”. In order to group all missing columns around this specific missing column, every site containing the value “5” that is related to the value “7” (neighbor) is changed to “6” (see

example in Fig. 5.9b). With this sequence, only the first neighbors are taken into account.

(a) 

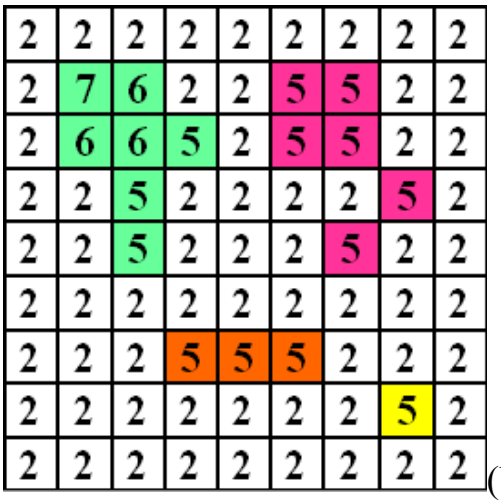

(b)

Figure 5.9: Left, first step of algorithm, the values below threshold (50) are fixed at "5", the others at "2". Right, second step, the first "5" is changed to a "7" and the neighbors to "6".

3) In order to incorporate all grouped missing columns to the same crack, several scans are performed to change every value equal to "5" to "6" when the "5" is located just around a "6". The result of this step is presented in Fig. 5.10a: the first crack is now completely determined.
4) The steps 2 and 3 are repeated until the grid of 81 possible sites no longer contains a "5". The result of this example is presented in Fig. 5.10b.

(a) 

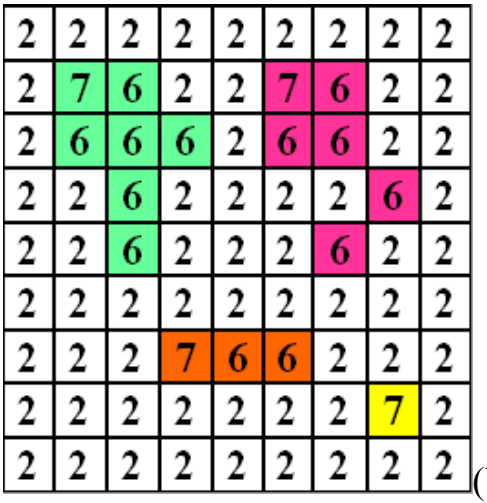

(b)

Figure 5.10: Left: third step, every "5" directly around a "6" changes to "6". Right: last step, every column is completed, the number of cracks is equal to number of "7"'s in the grid.

The number of cracks is thus equal to the number of "7"'s in the grid; in this example, the number of cracks is equal to 4.

5.6. New substrates to study cracks

Our numerical simulations are focused on the influence of the substrate steepness and valley curvature radii on cracks (see Chapter 4 as well, where various types of substrates were studied). For this purpose, we have defined a new substrate that consists of the superposition of a circle shape and a pyramidal shape. The user can choose the steepness of the pyramidal substrate's features (angle α) and the curvature radii of the valleys represented by the circles in Fig. 5.11.

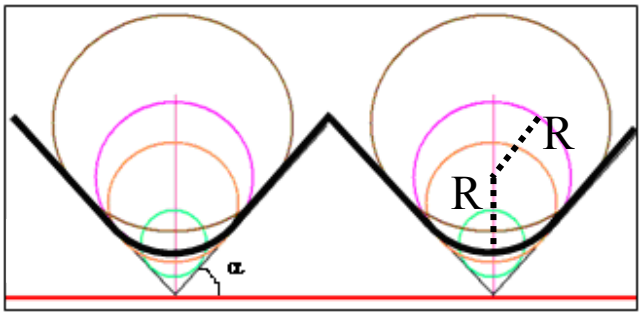

Figure 5.11: Variable substrate used for numerical simulations with MANEMO: The angle of pyramids can be chosen and the U-shaped is determined by its curvature radii. The bold line shows an example of a final substrate.

5.6.1. Simulation results for U-shaped type substrate

By keeping constant all model parameters ((i) to (v)) during the simulation and by changing only the morphology of the substrate, the number of cracks has been calculated for a large number of different substrates with the method described in Section 5.6. The complete result is given in Fig. 5.13 and a view of 2 different cases is presented in Fig. 5.12. (Same input parameters as in Fig. 5.7)

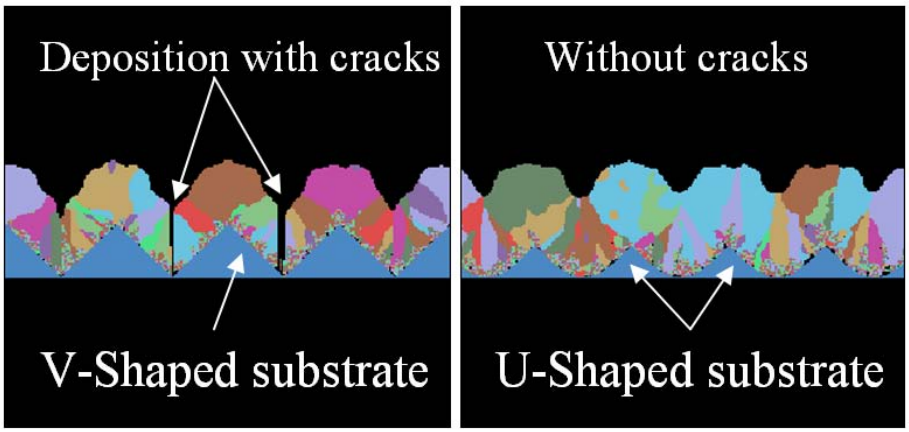

Figure 5.12: Results of numerical simulation with MANEMO. Left: simulated deposition on V-shaped substrate. Right: simulated deposition on U-shaped substrate.

The simulated density of cracks decreases when the morphology of the substrate changes from V-shaped to U-shaped (increase of curvature radii), as shown in Fig. 5.13. The density of cracks also depends on the angles of the pyramids. Smaller pyramid angles lead to higher density material (fewer cracks), as can be seen in Fig. 5.13.

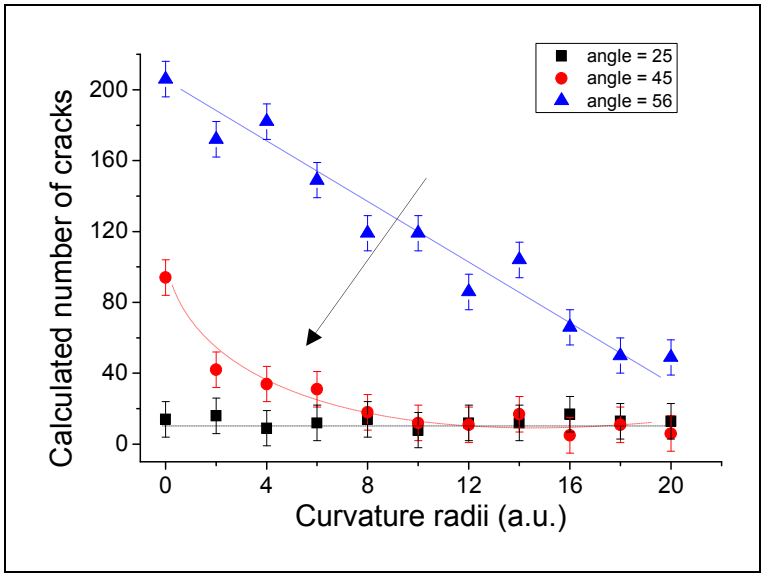

Figure 5.13: Results of the numerical simulation with MANEMO: density of cracks as a function of the substrate's valley curvature radii. One can observe lower density material (more cracks) for steep pyramids (large angle). Dotted lines are a visual guide.

As already mentioned, the density of cracks in µc-Si:H thin film solar cells can be reduced by treating the substrate to avoid small structures between the pyramids and by smoothing the surface (from V-shaped to U-shaped), see Chapter 4 as well.

5.7. Effect of diffusion length on cracks

By keeping constant the input variables during the simulation and by changing only the variable (iv): "maximum number of diffusion steps", the crack density decreases with the diffusion of adatoms (Fig. 5.14).

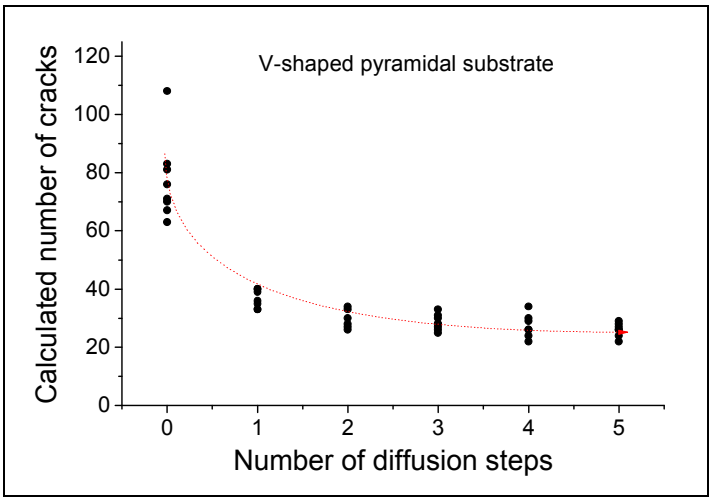

Figure 5.14: Results of numerical simulation with MANEMO: density of cracks as a function of the diffusion steps of adatoms during the deposition. On observe a higher density (less cracks) with high diffusion steps. Dotted line is a visual guide.

This result will be used as the departure point for the analysis of the effect of substrate temperature on cracks presented in Chapter 8. Indeed, the increase of substrate temperature during the deposition will lead to an increase of the diffusion of the adatoms at the surface of the substrate and growing layer. Then, the particle will be able to more easily reach zones like the bottom of the pyramids where low density material is grown.

5.8. Conclusion

The modifications added here, to the initial simulation program developed by J. Bailat et al., were shown to be necessary to correctly model the microcrystalline growth. Indeed, our MANEMO program is now able to reproduce some defects that appear during the deposition, namely the voids and cracks. The microstructure is well simulated by adding to the program (i) the isotropic incidence of particles, (ii) a kind of diffusion, by maximizing the number of neighbors and (iii) the new substrate features (pyramid angle and curvature radii), which help to study the variations in morphologies.
In order to prevent the formation of cracks, our simulations indicate that two factors are determinant: (a) the substrate geometry and (b) the number of adatom diffusion steps on the growing surface.
We have highlighted both, experimentally and numerically that substrates with dedicated morphology are more favorable for dense growth of µc-Si:H. Our simulations confirm the decrease of the crack density with increased curvature radii of the valley and decrease of pyramid angle. As a consequence, according to our simulation, an ideal substrate for dense µc-Si:H growth should possess either large uniform structures with U-shaped valleys or reasonable opening angles. Such substrates should lead to high V_{oc} and high FF devices (see Chapter

4). Nevertheless, such substrates may not be ideal for efficient light trapping within the device (i.e for devices with large short-circuit current). Therefore, the ideal substrate for high performance μc-Si:H single junction solar cells according to simulations confirms the conclusion given at the end of Chapter 4: the ideal substrate would possess high roughness with curvature radii higher than 200-300 nm (approximation for curvature radii of 20 pixels on pyramidal structure of 60 pixels).
In Chapter 8, we will demonstrate experimentally that increasing the surface diffusion length by increasing the substrate temperature may be another way to obtain crack-less, dense μc-Si:H. Experimentally, the increase of diffusion at the growing surface can be achieved by increasing the substrate temperature, the hydrogen content or the ion bombardment during the deposition of the thin film solar cell.

6. µc-Si:H electronic quality evaluated by FTPS

6.1. Introduction

The quality of a thin film solar cell is determined among other things, by the electronic quality of the intrinsic (i-)layer, which is the active part of the solar cell. Indeed, this layer plays the role of absorbing material, whereas p and n layers are too defective and are, hence, only used to create the internal electrical field to separate electrons and holes created in the i-layer by absorption of photons. The intrinsic layer has to possess the lowest possible defect density in order to avoid recombination of photogenerated carriers. Therefore, a characterization technique is necessary to determine the electronic quality of the i-layer (i.e. the defect density) to improve the electrical performances of the microcrystalline solar cells: for a-Si:H material, photothermal deflection spectroscopy (PDS) or constant photocurrent method (CPM) [Fejfar 1996, Poruba 2000, Vanecek 2000, Roca i Cabarrocas 2002] are used on layers deposited on glass. For µc-Si:H solar cells, Fourier Transform Photocurrent Spectroscopy (FTPS) can be used to get information of the material quality, as described in Chapter 2. FTPS is a fast and very sensitive method for the evaluation of the spectral dependence of the optical absorption coefficient [Vanecek 2002], thus permitting the evaluation of the density of defects in the i-layer of µc-Si:H solar cells. In this Chapter, we demonstrate that the properties of the substrate have an influence on the values obtained from "FTPS" measurement, which can be considered as artifacts. Three characteristics of the ZnO (doping, thickness, and surface morphology) modify the light intensity that enters in the silicon solar cell leading to an inexact evaluation. Two methods are then proposed to suppress the influence of the TCO in order to be able to compare the quality of the intrinsic layer of cells deposited on different substrates. However, it turns out from the various measurements, that, with the exception of the strongly pinched substrate, the substrate morphology and the cracks only weakly affect the FTPS material quality.

6.2. Influence of transparent conductive oxide parameters on FTPS measurements

As explained in [Faÿ 2003], the natural ZnO growth result in a pyramidal surface morphology and larger layer thickness leads to larger pyramids. ZnO is "M4" type with a ratio of gas flow (B_2H_6/DEZ) of 0.6, which leads to a density of $8 \cdot 10^{19}$ cm^{-3} electrons. Three main parameters of ZnO on which the solar cells are deposited (see Fig. 6.1), will influence the amount of light entering in the

silicon layers: (i) doping and defect density, (ii) thickness, and (iii) surface morphology.

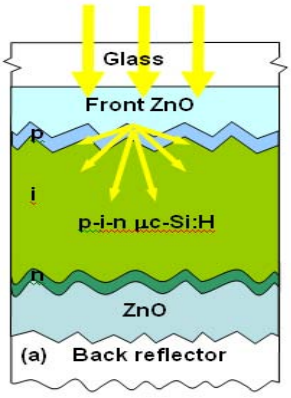

Figure 6.1 Typical structure of a p-i-n thin film microcrystalline silicon solar cell. The light goes through the front TCO before entering in the cell.

The next three Sections present the artifacts that may be observed when various ZnO are used for the same series of single junction µc-Si:H devices, and finally, two methods are presented in order to avoid them.
The parameters under investigation for FTPS measurements are the absorption at 0.8 eV, which represents the density of dangling bonds [Shah 2000, Vanecek 2000, Vanecek 2001] and the slope of the Urbach edge E_0 (determined between 1 and 1.1eV), which gives information about the disorder in a material (see details in Chapter 2). Note that all spectra shown in this Chapter have been calibrated at 1.35 eV according to the description in Chapter 2. If the influence of the ZnO is constant over the range from 0.8 eV to 1.35 eV (calibration point), then, there is no influence on the 2 parameters under investigation. Unfortunately, we will see that the influence is not constant, but varies as a function of the photon energy.

6.2.1. Influence of front ZnO doping concentration on FTPS measurements

Doping of TCO induces free carrier absorption (FCA). In the case of boron-doped LP-CVD ZnO, the light between 0.6 and 1.4 eV is absorbed (as seen in Fig. 6.2) [Faÿ 2003, Steinhauser 2006]. This absorption is not constant over the range of investigation, leading to a variation of the parameters $\alpha_{0.8eV}$ and E_0. The value at 0.8 eV is strongly influenced by doping in the front ZnO, whereas the variation between 1eV and 1.1eV is smaller, as seen in Fig. 6.2.

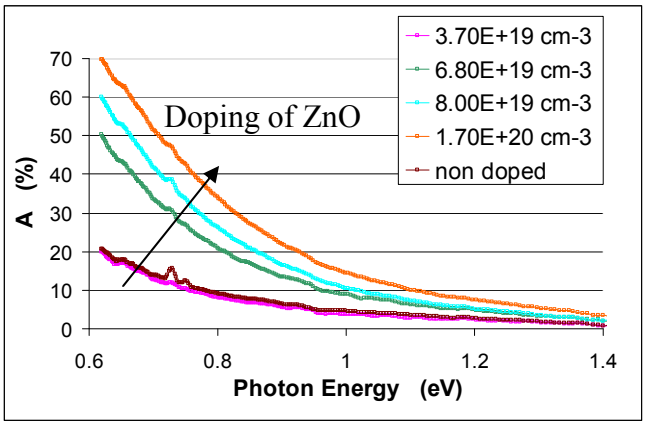

Figure 6.2: Absorption of ZnO films with various concentrations of boron with similar sheet resistance of 10 Ω/sq [Steinhauser 2008] measured by spectroscopy.

In this series, ZnO was deposited with different B_2H_6/DEZ fluxes, resulting in various doping levels. The ZnO thickness was adapted to the doping level in order to keep the same sheet resistance of approximately 10 ohms-square. µc-Si:H cells were deposited with the same PECVD deposition conditions (co-deposition) on the ZnO series and analyzed by FTPS, see Fig. 6.3:

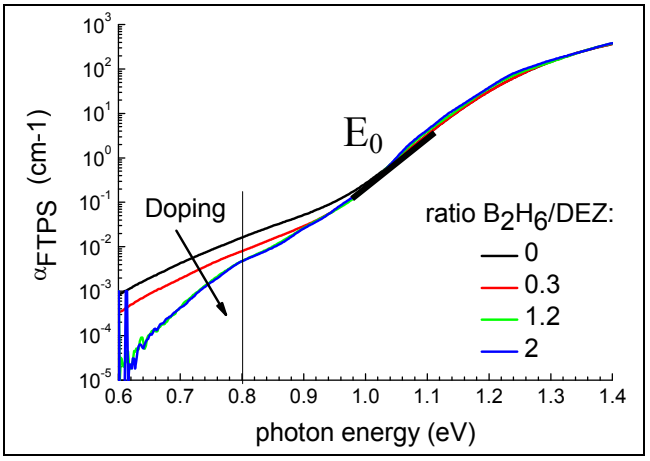

Figure 6.3: Absorption coefficient (FTPS) for µc-Si:H solar cells co-deposited on front ZnO with various doping levels, but similar sheet resistances.

The free carrier absorption (FCA) is high between 0.6 and 0.9 eV and artificially decreases the absorption at 0.8 eV. In Fig. 6.4, it is seen that saturation occurs with doping at low $\alpha_{0.8eV}$ level of 0.005. Two reasons can explain such variation: (i) the major part of the infrared light is absorbed in the TCO and not in the silicon or (ii) the doping efficiency of the boron is reached.

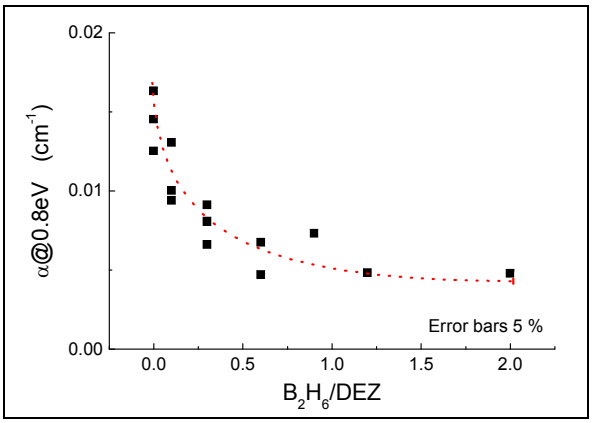

Figure 6.4: Absorption at 0.8 eV of co-deposited µc-Si :H solar cell on ZnO with various boron doping. Dotted line is a visual guide.

The slope between 1 and 1.1 eV (Urbach parameter E_0) is also affected by the FCA of the front TCO (Fig. 6.5). The influence is however lower, because the absorption by the free carrier is lower (see Fig. 6.2) at this photon energy.

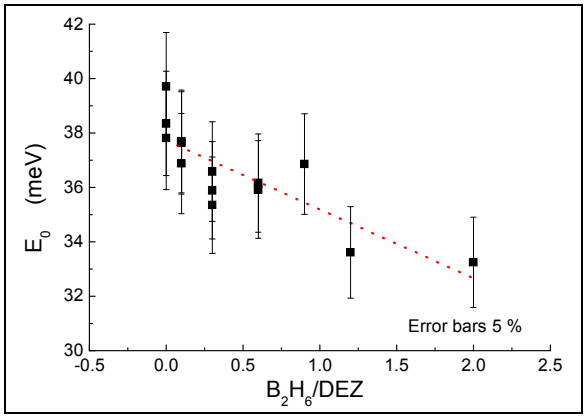

Figure 6.5: Urbach slope for co-deposited µc-Si:H solar cell on ZnO with various boron doping. Dotted line is the linear fit.

Therefore, α(0.8 eV) and E_0 are, under these conditions, not only linked to the i-layer quality, but are also influenced by the doping of the TCO.

It is to mention here that the thickness also varies for this series and probably the quality of the cells is not the same on such various substrates. Then, one can only conclude that the FCA modify the FTPS signal and we have to be careful in treating those results

6.2.2. Influence of ZnO thickness on FTPS measurements

In this series of cells, the ZnO thickness varies as a result of deposition time and thus sheet resistance is not constant [Feitkneicht 2005]. The size of the pyramids is directly linked to the thickness of ZnO: a larger thickness leads to larger

pyramids of ZnO [Faÿ 2003]. If the thickness of ZnO is larger, 2 phenomena are in competition: various-sized pyramids will modify the light scattering and consequently the FTPS measurement, and the thicker ZnO will absorb more light (due to FCA), leading to an apparent reduction of the measured FTPS absorption in infrared (IR) region. Also in this case, the variation of light intensity absorbed in the TCO between 0.8 eV and 1.35 eV will modify the $\alpha_{0.8eV}$ and E_0.
In Fig. 6.6, the transmittance's measurements of ZnO/Si interface for small pyramids (small thickness of ZnO) (type-A) and larger pyramids (type-B) show that the haze factor (ratio between diffuse transmittance and total transmittance), as well as angular diffusion, is not constant (Fig. 6.6e). Note that 0.8 eV = 1550 nm and 1.35 eV = 918 nm.

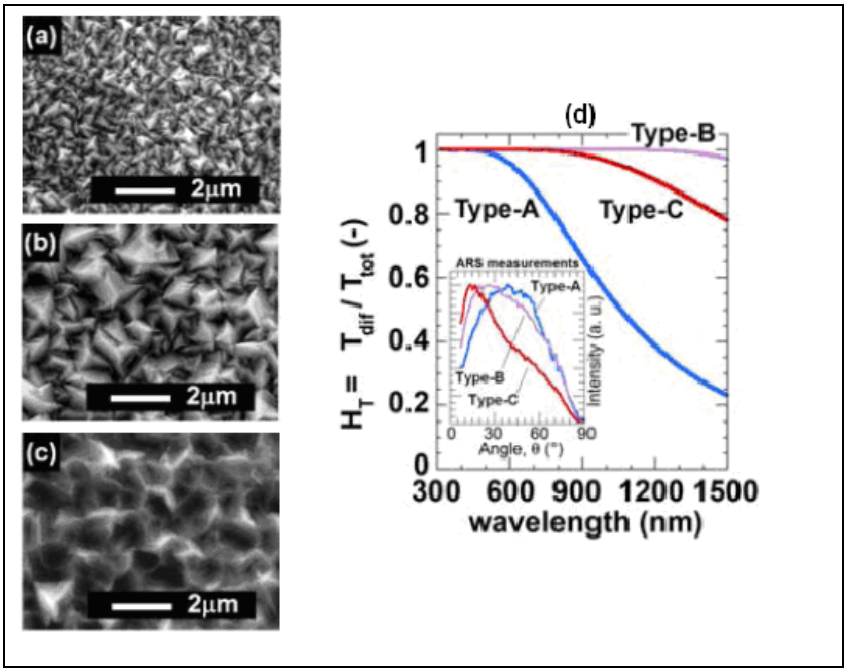

Figure 6.6: (a)–(c) SEM pictures of typical type-A (small pyramids), -B (large pyramids) and –C (large treated pyramids) ZnO layers. Haze at the ZnO/Si interface for the type-A, -B and -C front ZnO layers. The inset in (d) shows angular resolved scattering (ARS) measurements in-air (From [Dominé 2008]).

The variation of this diffusion between 0.8 eV and 1.35 eV (see Fig. 6.6e for ZnO/Si interface) is lower for large pyramids (type-B) than for small ones (type-A): for large pyramids, the haze at 1.35 eV is around 100% and decrease to around 95 % at 0.8 eV, whereas for small pyramids, the haze varies from 65 % to 25 %, respectively. Then, taking into account the calibration at 1.35 eV (918 nm), the apparent FTPS measurement will be modified by the light scattering due to various pyramidal sizes of ZnO: the increase in pyramid size (and thus ZnO thickness) will artificially increase the $\alpha_{0.8eV}$ and E_0.
These two effects are clearly seen in Fig. 6.7a with an initial increase of $\alpha_{0.8}$ followed by a slight reduction. We suggest that the light scattering dominates

but reaches saturation between 2 µm and 2.6 µm, whereas the FCA linearly increases with ZnO thickness leading to a decrease in the measured absorption. For the value of E_0, the increase is linear in function of the thicknesses, as can be seen in Fig. 6.7b, due to the increase in light scattering in infrared region. This effect is important, as it can compensate for the change in FCA, as would be expected from Fig. 6.5.

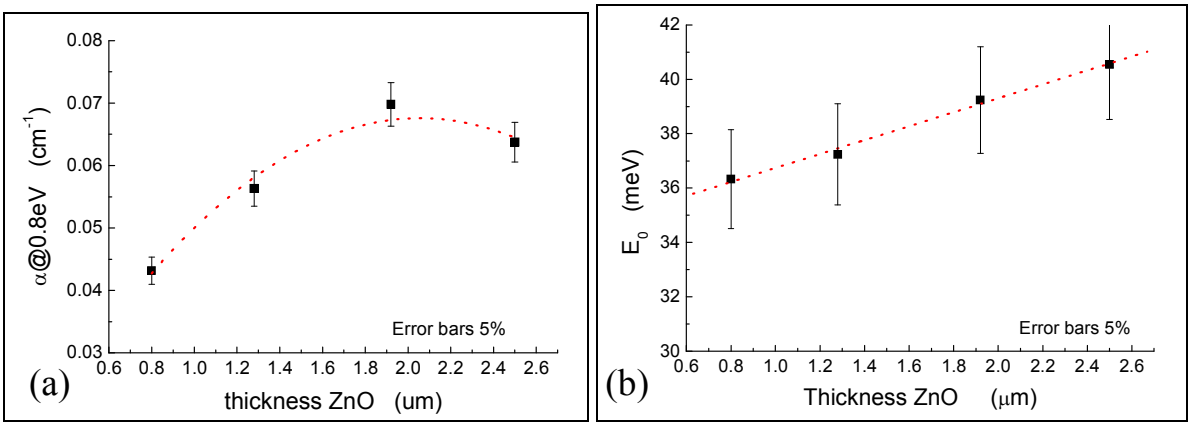

Figure 6.7: Optical parameters of µc-Si:H from ZnO thickness series. a) FTPS signal at 0.8 eV, dotted line is a visual guide, b) Variation of E_0, dotted line is the linear fit.

6.2.3. Influence of ZnO surface morphology on FTPS measurements

The light trapping/scattering depends on the wavelength and can influence $\alpha_{0.8eV}$ and E_0 (as seen in 6.2.1 and 6.2.2). Initially, our aim was to check whether the morphology and the cracks would have a strong influence on the "true" value of $\alpha_{0.8eV}$ and E_0. For this series in ZnO surface morphology, lightly-doped ZnO has been used and a surface post-treatment that modified rms roughness and surface topography (V-shaped to U-shaped) has been performed [Bailat 2006]. The subsequent deposition of the µc-Si:H cells is then identical. The surface treatment thus decreases the light scattering, J_{sc} being reduced for surface treatment times above 20 minutes, whereas the V_{oc} and FF increase with ZnO treatment time as seen in Fig. 6.8.

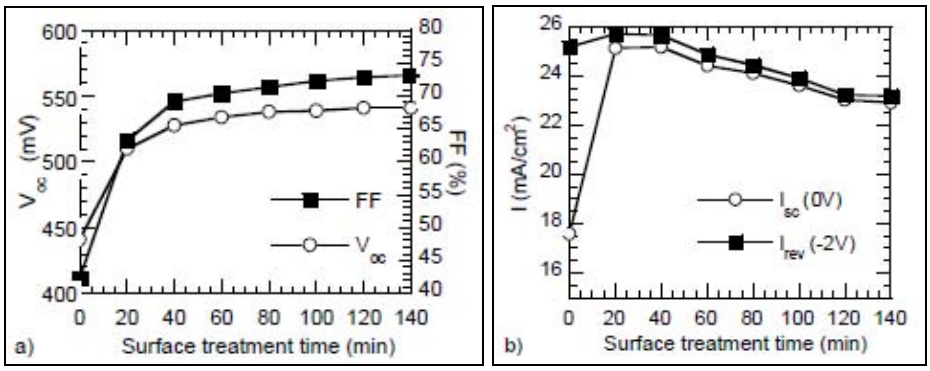

Figure 6.8: Electrical performances of µc-Si:H solar cells deposited on various treated ZnO: a) V_{oc} and FF increase in function of ZnO treatment, b) variation of short-circuit current density (with and without reverse bias voltage). From [Bailat 2006].

The treatment of the surface also decreases the FTPS signal, because the diffusion of the light decreases between type-B (large pyramids) and type-C (large pyramids with surface treatment), as seen in Fig. 6.6e. Nevertheless, the treatment of ZnO also slightly decrease the thickness of the ZnO layer, leading to an artificial increase in the FTPS measurement (less FCA in ZnO).
We observe in Fig. 6.9 that, with the exception of the untreated sample, there is only a minor change in $\alpha_{0.8eV}$ with the treated samples. The substrates are flatter and thinner in function of the treatment and lead to both artificial increase due to less FCA (thinner samples) and artificial decrease due to change in light scattering.

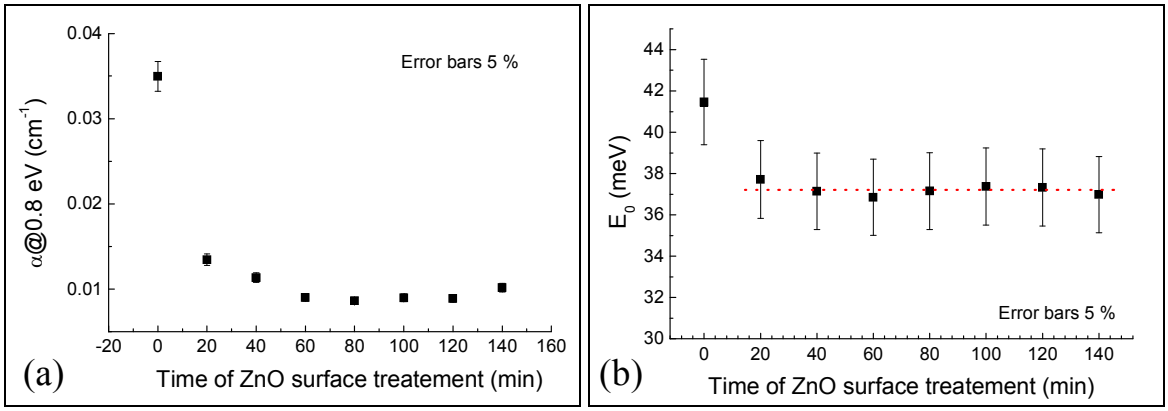

Figure 6.9: Optical parameters of µc-Si:H from ZnO surface treatment time series. a) FTPS signal at 0.8 eV, b) Variation of E_0. Dotted line is a visual guide.

It is also observed in Fig. 6.9b that E_0 is stable from one substrate to another except for non-treated ZnO (E_0 ~ 37 meV and 41 meV for non-treated). Note that, this series of cells is characterized by a high efficiency (between 8 and 9 %), except for the cell deposited without surface treatment, for which efficiency is only 6 %.

6.3. Discussion on the influence of the substrate in FTPS measurements

Based on the results presented here, it appears that roughness, doping as well as the morphology of ZnO modify the α(hυ) measurement of μc-Si:H.
The increase in doping and thickness of ZnO will increase the FCA (Free Carrier Absorption), which is due to the free carriers in ZnO. The intensity of the light which enters the p-i-n device decrease and will thus decrease the FTPS absorption for low photon energies and consequently, the value $\alpha_{0.8}$ will appear lower than in reality. The measurement of the Urbach parameter E_0 is also slightly affected by the difference in doping of ZnO, but to a lower extent because the slope was calculated for the values between 1 and 1.1 eV (1130-1240 nm) where the FCA is low (less than 10% of variation). However, the increase in thickness will increase the pyramid's size and thus increase the light scattering and modify the relative light path enhancement at different wavelengths. Then, the Urbach parameter E_0 will increase with ZnO thickness.
The decrease of $\alpha_{0.8eV}$ between non-treated and treated 20 minutes in Fig. 6.9 is related to the quality of the silicon, as seen in [Bailat 2006]. The slight variation between 20 minutes and 140 minutes is explained by the competitive effect of the change in light scattering (inducing a lower $\alpha_{0.8eV}$) and decrease in thickness of ZnO (less FCA → induce higher $\alpha_{0.8eV}$) due to the surface treatment. The stability of E_0 measured on surface treated sample (except for untreated sample), as well as the minor variations in $\alpha_{0.8eV}$, suggest that no significant difference exists in the material quality of such samples, even though difference in V_{oc} and FF are observed. Two important conclusions can be drawn:
1) Cracks linked to the surface morphology do not contribute significantly to the $\alpha_{0.8eV}$ and can therefore be considered as 2 dimensional surfaces in the device (= no bulk contribution).
2) The FTPS material quality for a given PECVD process seems to be quite independent of the substrate morphology (except for the case of untreated sample).
Chapters 7 and 8 will confirm these conclusions and the role of the cracks will be confirmed as being responsible for the low electrical properties of some devices.
Finally, in order to be able to properly separate the real material quality ($\alpha_{0.8eV}$ true) from artifacts linked to light scattering and FCA in the TCO, a proper correction method should be applied. Even though we do not apply it on the series of samples, we demonstrate in Section 6.4 two methods to correct the FTPS curve.

6.4. Original methods to suppress the influence of ZnO on FTPS measurements

As discussed in the previous Section, the measurement of FTPS signal does not give the real absorption coefficient of the i-layer, because of additional absorption in the front ZnO or wavelength dependent light scattering. This situation is not equivalent to that, for instance, of a glass + ZnO filter placed in front of a silicon layer, because the optical coupling in a full cell structure is completely different (ZnO scatters the light and enhanced multiple internal reflections inside the silicon lead to a strong absorption in the ZnO). In order to obtain the true absorption, it is thus necessary to know the absorption of ZnO in the infrared region (from 0.8 eV to 1.35 eV) under the real optical conditions of a solar cell.

A simple model would consist in assuming that the absorption in the front and back ZnO reduces α_{FTPS} by a factor given by:

$$\alpha_{true} = (\alpha_{FTPS}) / (1 - A_{ZnO}) \qquad (6.1),$$

where the absorption in the doped silicon layers is neglected. They are two possible ways to proceed, described in 6.4.1 and 6.4.2:

6.4.1. First method

The first method to suppress the effect of the front and back ZnO during the FTPS measurement requires the deposition of an amorphous silicon solar cell that is similar to the microcrystalline solar cell we want to measure (Fig. 6.10), meaning here:

- Deposited on the same ZnO.
- Same i-layer thickness as the microcrystalline solar cell (here 1.6 μm).
- Same back TCO.

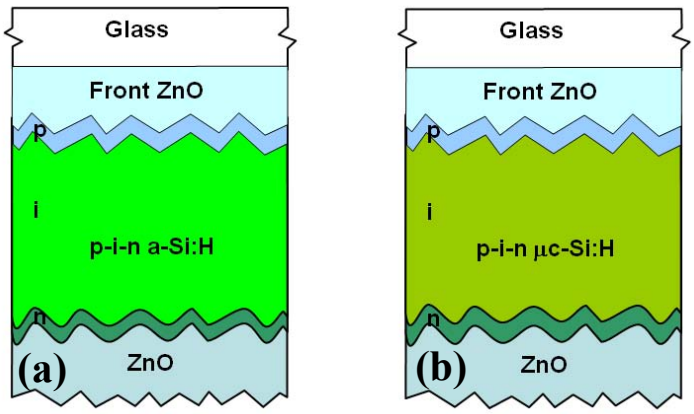

Figure 6.10: Sketch of the two devices necessary for the correction of FTPS measurement by the first method (same TCO and same p-i-n thicknesses).

First, the absorptance of ZnO is calculated by measuring the transmittance and reflectance curves of ZnO with a spectrometer for ZnO in real devices, under the same conditions as for microcrystalline silicon solar cells but with amorphous silicon. Indeed, the absorption is negligible for silicon in the infrared region, but the scattering and internal reflectance due to the front ZnO will be similar. The absorption of ZnO below the bandgap of a-Si:H is then given by:

$$A_{ZnO} = 1 - T_{ZnO} - R_{ZnO} \qquad (6.2)$$

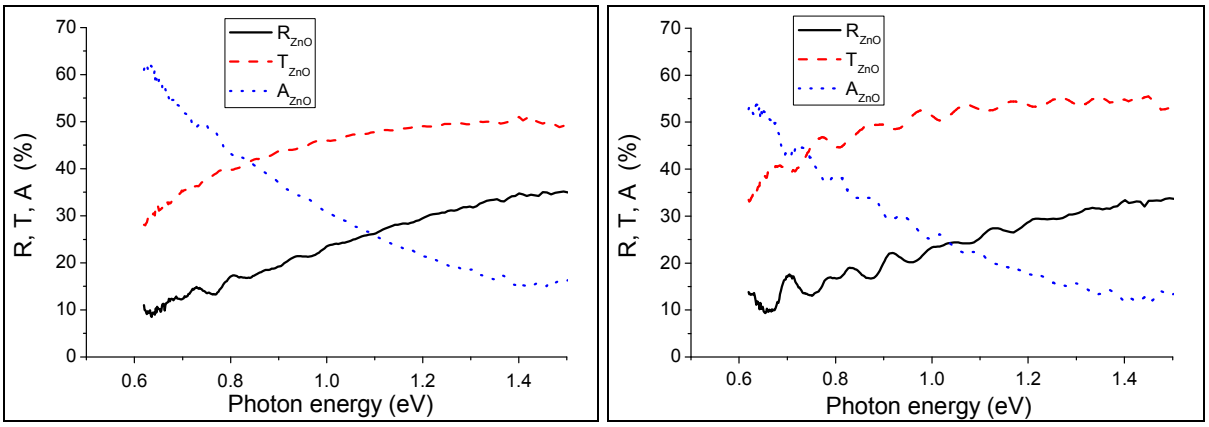

Figure 6.11: Measured transmittance and reflectance and calculated absorptance for the device of Fig. 6.10a. Left: ZnO treated for 30 min // Right: ZnO treated for 60 minutes.

Fig. 6.11 shows the transmittance, reflectance and absorptance of devices as in Fig. 6.10a for two different front ZnO (thickness of the silicon p-i-n layer is around 1.6 µm). The curves in Fig. 6.11 right have more interference due to flatter interface.

Second, the measurement of the microcrystalline silicon solar cell is performed by FTPS (standard measurement) and the correction is applied to obtain the α_{true} from the α_{FTPS} obtained, based on equation 6.1.

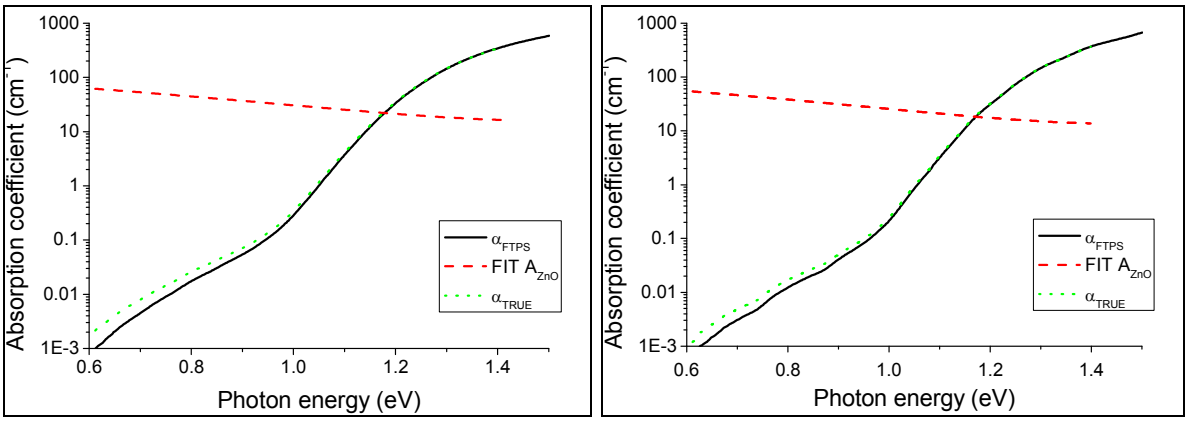

Figure 6.12: Measured and corrected absorption coefficient of µc-Si:H solar cell. Left: ZnO treated for 30 min // Right: ZnO treated for 60 minutes. In red, the extrapolation of the ZnO absorptance as calculated for the device in Fig. 6.10a.

Hence one can observe that the true absorption is higher that the measured one, since zinc oxide absorbs in infrared region (see Fig. 6.2). Note the it is necessary to extrapolate the ZnO absorptance, because the number of points between the FTPS measurements and the spectrometer measurements are not the same.

6.4.2. Second method

With this method, no complementary device is necessary. Indeed, in this case, the ZnO absorption is still measured with the spectrometer in the microcrystalline cell, but this time, the absorption is corrected with the EQE measurement as described in eq. 6.3:

$$A_{ZnO} = 1 - T_{Cell} - R_{Cell} - EQE \qquad (6.3)$$

Then, transmittance, reflectance and EQE of the cells are presented in Fig. 6.13, and the correction is again performed according to eq. 6.1, see Fig. 6.14.

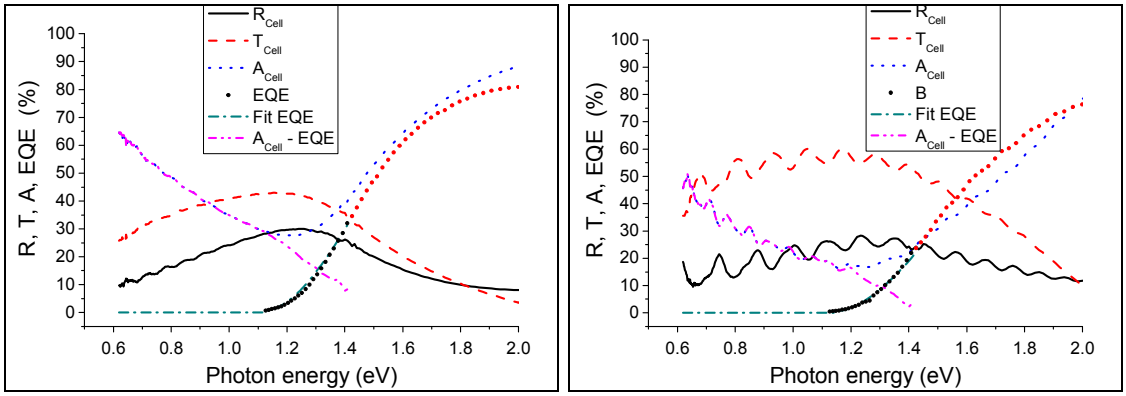

Figure 6.13: Measured reflectance, transmittance, calculated absorption, measured EQE and fit. The final absorption of ZnO is calculated with eq. 6.3. Left: ZnO treated for 30 min // Right: ZnO treated for 60 minutes.

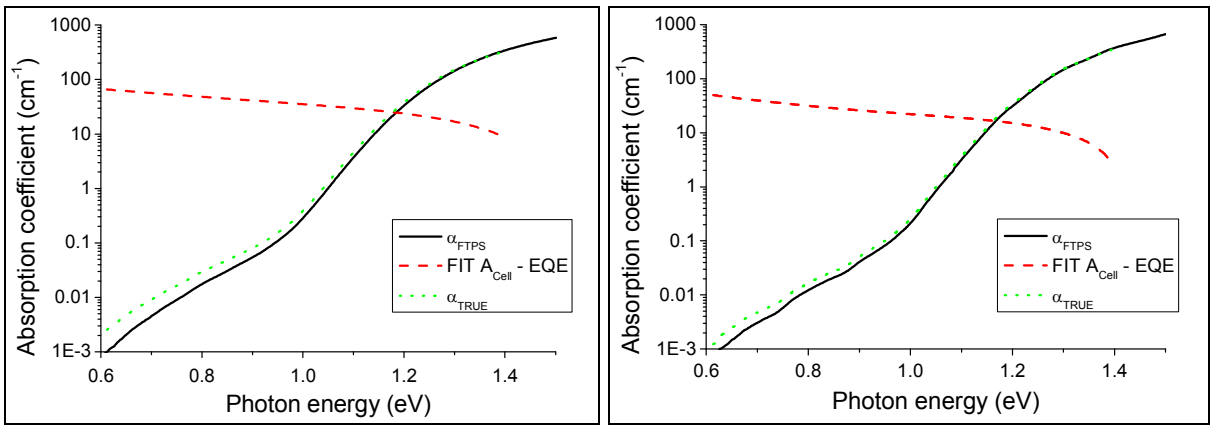

Figure 6.14: Measured and corrected absorption coefficient of microcrystalline silicon solar cell. Left: ZnO treated for 30 min // Right: ZnO treated for 60 minutes. In red, the fit of the ZnO absorptance.

6.4.3. Comparison between both methods

The comparison is performed for both ZnO treated for 30 minutes and for 60 minutes, as shown in Fig. 6.15:

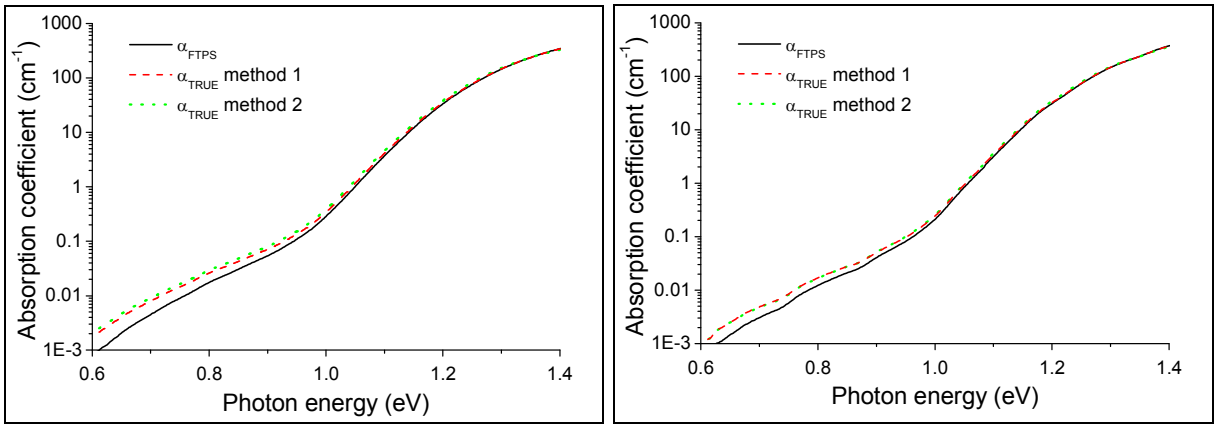

Figure 6.15: Comparison of corrected absorption coefficient with the two methods proposed in this Chapter. Left: ZnO treated for 30 min // Right: ZnO treated for 60 minutes.

We observe that both methods give very similar corrected absorptions for the device with ZnO treated for 30 minutes and with ZnO treated 60 minutes.

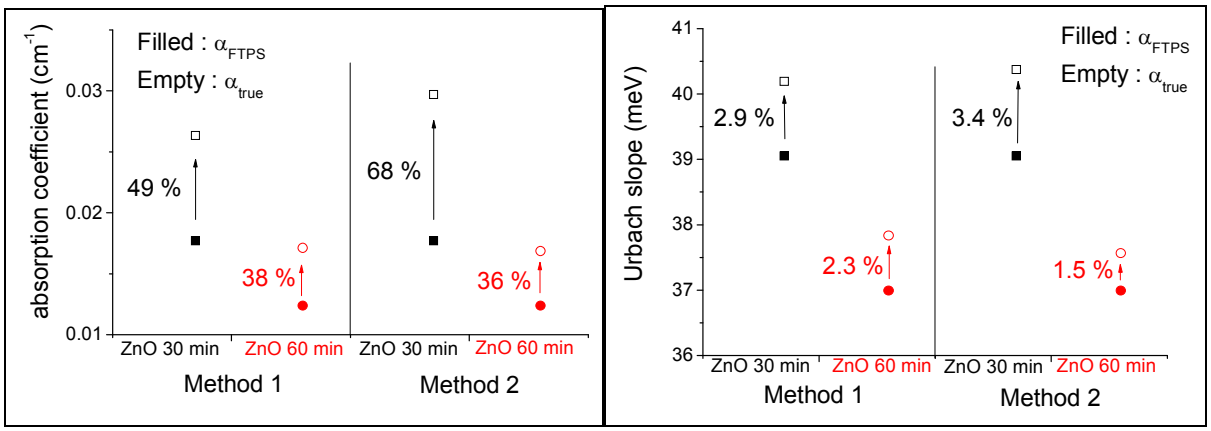

Figure 6.16: Results for $\alpha_{0.8eV}$ and Urbach slope E_0 for comparison between measured and corrected FTPS absorption curves.

Fig. 6.16 shows the variation of $\alpha_{0.8eV}$ and E_0 for the curves presented in Fig. 6.15. The absorption at 0.8 eV, obtained with the FTPS measurements, is underestimated due to the absorption of the light in the ZnO (FCA). With the help of the correction methods, one can see that the $\alpha_{0.8eV}$ true value is between 49 and 68 % higher than the measured one for the cells deposited on ZnO treated during 30 minutes, whereas the correction is around 37 % for cells deposited on ZnO treated 60 minutes.
The value of Urbach parameter E_0 is also modified for around 3 % for cells deposited on ZnO treated 30 minutes and around 2 % for the cells on ZnO treated 60 minutes.

6.4.4. Use of 2nd method for correction of surface treatment series

The simplest method is the second method, because it is not necessary to deposit an amorphous cell of same thickness for each substrate.

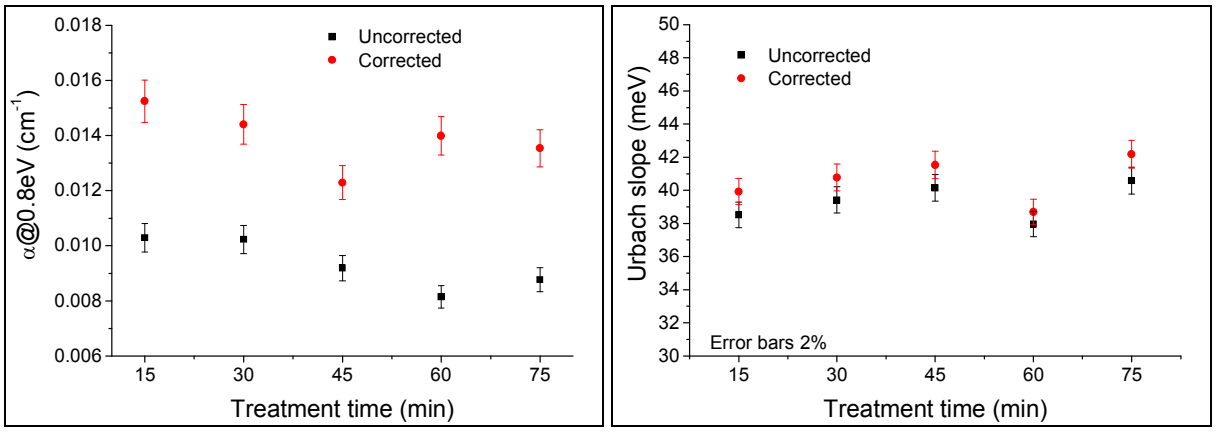

Figure 6.17: Results for $\alpha_{0.8eV}$ and Urbach slope E_0 for comparison between measured and corrected FTPS absorption curves.

In Fig. 6.17, one observes that the absorption at 0.8 eV is around 50 % higher after correction of the ZnO influence and do not vary a lot with the treatment time. For the Urbach slope, the value increase in average of 3 % after the correction and also there, the variation only slightly depends on the treatment.

6.5. Discussion

The influence of the TCO on the FTPS measurement is clearly demonstrated in this Chapter. The doping, the thickness and the surface morphology modify the intensity of the light that enters in the silicon solar cell, leading to an inexact evaluation. The two methods proposed here help to suppress the effect of the substrate and are in principle useful to compare the quality of the intrinsic layer of the microcrystalline silicon solar cells deposited on various substrates.

6.6. Conclusion

In this Chapter, we demonstrate that the substrate (glass + TCO) affects the measurement of FTPS. For series on the same TCO, no correction is necessary if only information on the relative variation is required. However, for a series where the TCO vary, it is then necessary to suppress the effect of the ZnO and thus, calculate the true absorption. We introduced two original methods to do so; the calculation of α_{true} by these two methods gives equivalent results. Finally, we mention here that the FTPS measurement is not suitable to analyze the quality of microcrystalline cells in terms of crack density as only minor variations are measured on a series of samples with changes of morphology. Indeed, this measurement only gives information on "bulk" and is not sensitive to 2D defects like cracks. More details will be given on that particular subject in Chapter 8 with Fig. 8.2 and Fig. 8.4. Note that the cells with back reflector can also be corrected with the 2 methods.

7. Effect of cracks on electrical parameters: experiments and modeling

7.1. Introduction

The effect of substrate surface morphology on microcrystalline silicon growth has already been described in Chapter 4, based on electron microscopy (especially TEM) and on the modified simulation program (see Chapter 5). It was demonstrated that V-shaped valleys of the substrate lead to the creation of cracks in the growing μc-Si:H material.
Furthermore, we have established a direct correlation between rough surface morphology and a reduction of open-circuit voltage (V_{oc}) and Fill Factor (FF) (Chapter 4) as previously observed [Nasuno 2002, Feitkneicht 2005]. Unfortunately, neither the equivalent electrical circuit proposed by Merten (Chapter 2) nor the FTPS measurement (Chapter 6) used to assess the quality of the intrinsic layer could successfully describe the influence of these cracks on electrical performances or defect density.
Here, we will introduce a new equivalent electrical circuit, where an additional parallel diode is introduced to take into account the effect of cracks on the J(V) characteristics of μc-Si:H single junction solar cells. We will show that cracks act as bad diode "recombination" in the equivalent electrical circuit.

7.2. "2 diodes" model

In 1998, Merten et al. [Merten 1998] proposed an equivalent electrical circuit for amorphous silicon solar cells modified to take into account the recombination current within the intrinsic layer (see Chapter 2 for more details). The circuit is composed of a diode, a photogeneration source, a series resistance and a shunt resistance, as well as a recombination current sink (see Fig. 7.1).

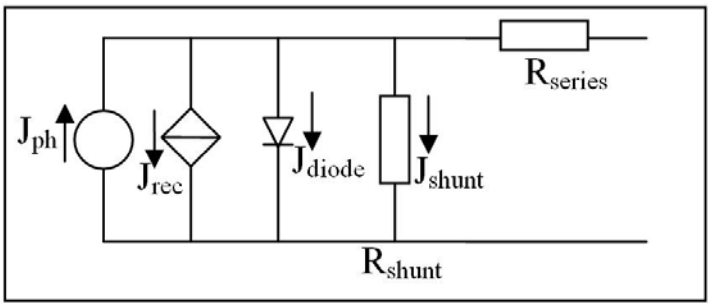

Figure 7.1: Merten's equivalent electrical circuit for a-Si:H solar cells [Merten 1998].

The J(V) curve of the a-Si:H p-i-n solar cell can then be expressed as the sum of the different contributions (principle of superposition), as already described in Chapter 2:

$$J_{tot}(V) = J_{diode} + J_{rec} + J_{shunt} - J_{ph} \tag{7.1}$$

with J_{diode} the current density of the p-i-n diode, J_{rec} the recombination current density, J_{shunt} the current density losses due to shunt and J_{ph} the photogenerated current density.

At first sight, cracks could be considered as some kind of linear shunts between the front and back contacts. Thus, by using this equivalent circuit one should be able to quantify the losses in V_{oc} and fill factor (FF) due to the increased recombination losses (decrease in collection voltage V_{coll}) and decreasing shunt resistance R_{sh}. However, when applying this approach to analyze our µc-Si:H solar cells series, the loss in FF and V_{oc} observed for cells with a high crack density is much larger than the loss that is predicted by the decrease of R_{sh} and of V_{coll} measured [Meillaud 2006]. A modification of the equivalent electrical model is thus necessary.

A new equivalent circuit for µc-Si:H solar cells is thus proposed here, see Fig. 7.2.

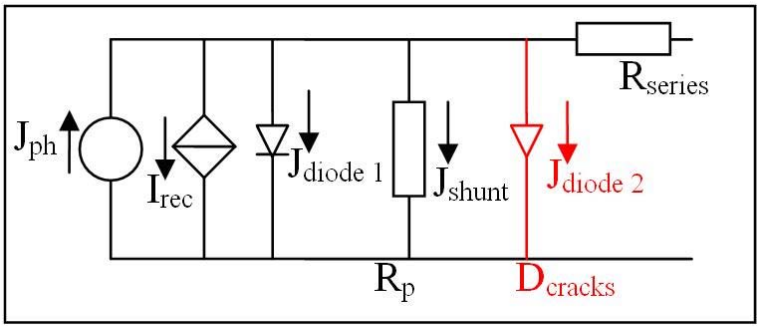

Figure 7.2: New equivalent electrical circuit for µc-Si:H solar cells, with an additional diode modeling cracks.

The µc-Si:H material can be decomposed into two parts: (i) the major part of the layer where the material is dense (represented as the white zone in Fig. 7.3) and (ii) zones of cracks (red zone in Fig. 7.3).

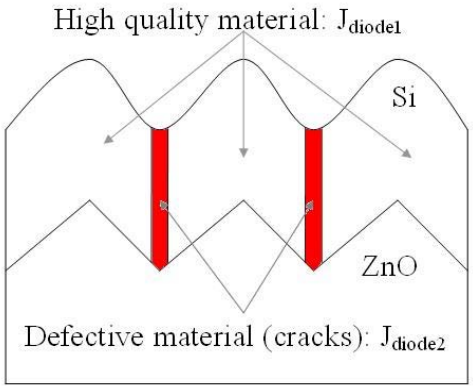

Figure 7.3: Sketch of silicon growth on rough ZnO: cracks are located above the valleys between the substrate's pyramids, the material is decomposed into two parts: dense (high quality material) and cracks (defective material).

The first zone (i) is represented in the model by the diode, as for Merten's model. The sum of every zone (ii) is represented by one additional diode, which represents a recombination diode (defective material) in parallel in the equivalent electrical circuit. The J(V) curve of the p-i-n solar cell is then expressed by:

$$J_{tot}(V) = J_{diode\_1} + J_{diode\_2} + J_{rec} + J_{sh} - J_{ph} \tag{7.2}$$

Which can be described as: (7.3):

$$J_{tot}(V) = J_{01}\left(\exp\left(\frac{qV'}{n_1 kT}\right)-1\right) + J_{02}\left(\exp\left(\frac{qV'}{n_2 kT}\right)-1\right) + J_{ph}\cdot\frac{\varphi(V')\cdot d_i^{\,2}}{(\mu\tau)_{eff}\cdot(V_{bi}-V')} + \frac{V'}{R_{sh}} - J_{ph} \tag{7.3}$$

$$V' = V - J_{tot}\cdot R_s \tag{7.4}$$

With J_{01} and J_{02} the reverse saturation current density for the first diode (high quality material) and the second diode (zones of cracks) respectively, V the voltage, n_1 and n_2 the ideality factors, V_{bi} the built-in voltage, $(\mu\tau)_{eff}$ the effective mobility-lifetime product, d_i the thickness of intrinsic layer, $\varphi(V)$ the electric field deformation factor, R_{sh} the shunt resistance, R_s the series resistance, and J_{ph} the photogenerated current density. The electrical field deformation factor is a function of the applied voltage, but is taken here as a constant ($\varphi = 1$).
In order to avoid the measurement of $(\mu\tau)_{eff}$ product, one can redefine the recombination current density J_{rec} as:

$$J_{rec} = J_{ph}\cdot\frac{\varphi(V')\cdot d_i^{\,2}}{(\mu\tau)_{eff}\cdot(V_{bi}-V')} = J_{ph}\cdot\frac{V_{bi}^2}{V_{coll}\cdot(V_{bi}-V')} \tag{7.5}$$

with $V_{coll} = \frac{(\mu\tau)_{eff} \cdot V_{bi}^2}{\varphi(V) \cdot d_i^2}$ the collection voltage, obtained by variable illumination measurement (VIM) as described in detail in Chapter 2.

The dark current density of the cell containing cracks is thus expressed by two components: (1) $\mathbf{J_{diode\_1}}$ corresponds to the dark current of a high quality reference cell, without cracks. (2) $\mathbf{J_{diode\_2}}$ corresponds to the dark current arising from cracks in the defective part of the solar cell.

7.3. Simulation procedure

A simulation program was developed with LabView that allows for fitting dark and illuminated J(V)-curves based on equation (7.3). The parameters that can be fitted by this program are: R_{sh}, R_s, n_1, n_2, $J_{01,}$ J_{02}, J_{sc} and V_{coll}. Only n_2 is fixed, equal to 2, in order to represent a recombination-limited device (as defined for p-n junction, [Grundmann 2005]). The reverse saturation current density J_{02} is, thus, the model parameter that will depend on the density of cracks in the intrinsic layer. The procedure employed to obtain the characteristics of the shunt diode is as follows:

- First, the parameters (R_{sh}, n_1, J_{01}) of an "ideal" μc-Si:H diode are obtained by measuring and fitting the dark J(V) curve of a high quality reference cell, deposited on rather flat ZnO (140 min of treatment), without any cracks.

- Second, the collection voltage V_{coll} value of this "ideal" cell is obtained from VIM measurements by measuring the slope on the linear part of R_{sc} as a function of $1/J_{sc}$ (see Chapter 2 for more details).

- Third, the standard J(V) curve at "1 sun" is measured for all other cells and fitted with $n_2 = 2$ (value for recombination-limited diode) and the other parameters (R_s, J_{02}, J_{sc}) are established based on the "2 diodes" model (eq. 7.3), whereas R_{sh}, n_1 and J_{01} are kept constant.

7.4. Relation between cracks and J_{02}

In a previous study by J. Bailat et al. [Bailat 2006], a relationship between the electrical parameters (V_{oc} and FF) of μc-Si:H solar cells and ZnO surface treatment was established: the V_{oc}, FF and efficiency values all increased with treatment time (see Fig. 6.8). Here, we find that the variation of solar cell

electrical performances can be properly explained by considering cracks as a second diode in the equivalent electrical circuit of the solar cells, characterized by the value of J_{02} obtained with the procedure describe above. Indeed, the J(V) curves for this series are very well fitted by the simulation procedure previously described, as can be seen in Fig. 7.4. Also, for one solar cell, the curves can be fitted properly at all illumination levels (not shown here).

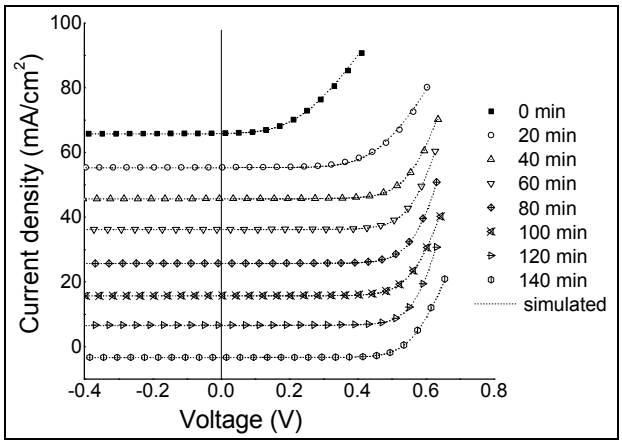

Figure 7.4: Experimental illuminated J(V) curves ("1 sun") for increased treatment time (shifted in current density axis). Excellent fits are obtained with 2 diodes model (dotted lines) by varying only the reverse saturation current density for the defective diode (J_{02}).

It is observed in Fig. 7.5 that J_{02} indeed decreases when the treatment time of the TCO increases.

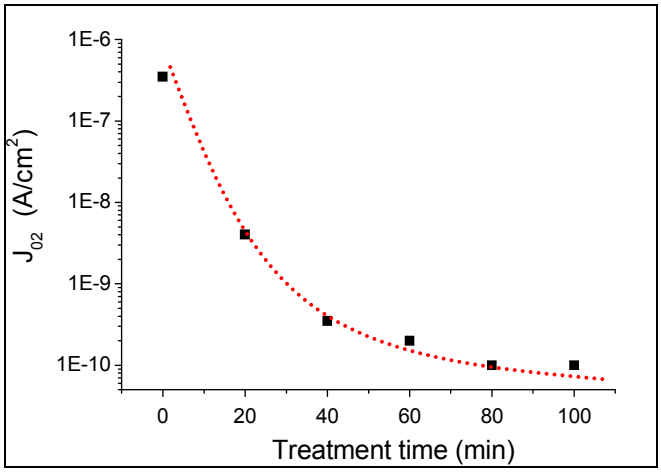

Figure 7.5: Reverse saturation current density J_{02} of the second diode (diode which represents the cracks) as a function of TCO treatment; J_{02} is derived from the "2 diodes model". The dotted line is a visual guide.

An additional defective diode in the equivalent electrical circuit thus allows us to fit the J(V) curves of the co-deposited cells on various treated ZnO. Cracks, acting as defective diode, are proven to be the origin of low electrical performances of µc-Si:H, principally of V_{oc} and FF. Excellent agreement

between measurements and simulation is also observed for all samples just by varying the J_{02} parameter (Fig. 7.6).

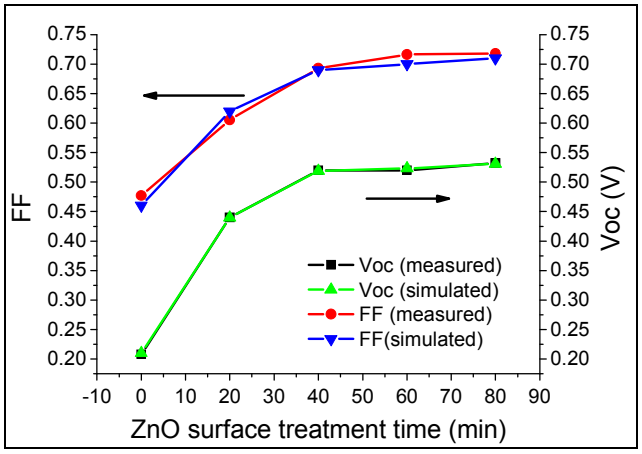

Figure 7.6: Measured and simulated V_{oc} and FF.

SEM and TEM micrographs (of Fig. 7.7), demonstrate the effect of surface treatment from V-shaped to U-shaped on cracks, with three samples from the ZnO treatment series (0 min, 40 min and 80 min). The SEM micrographs show the evolution of the morphology with the treatment time, whereas the TEM micrographs are suitable for comparing the shape of the pyramids (V-shaped or U-shaped) and the crack density.

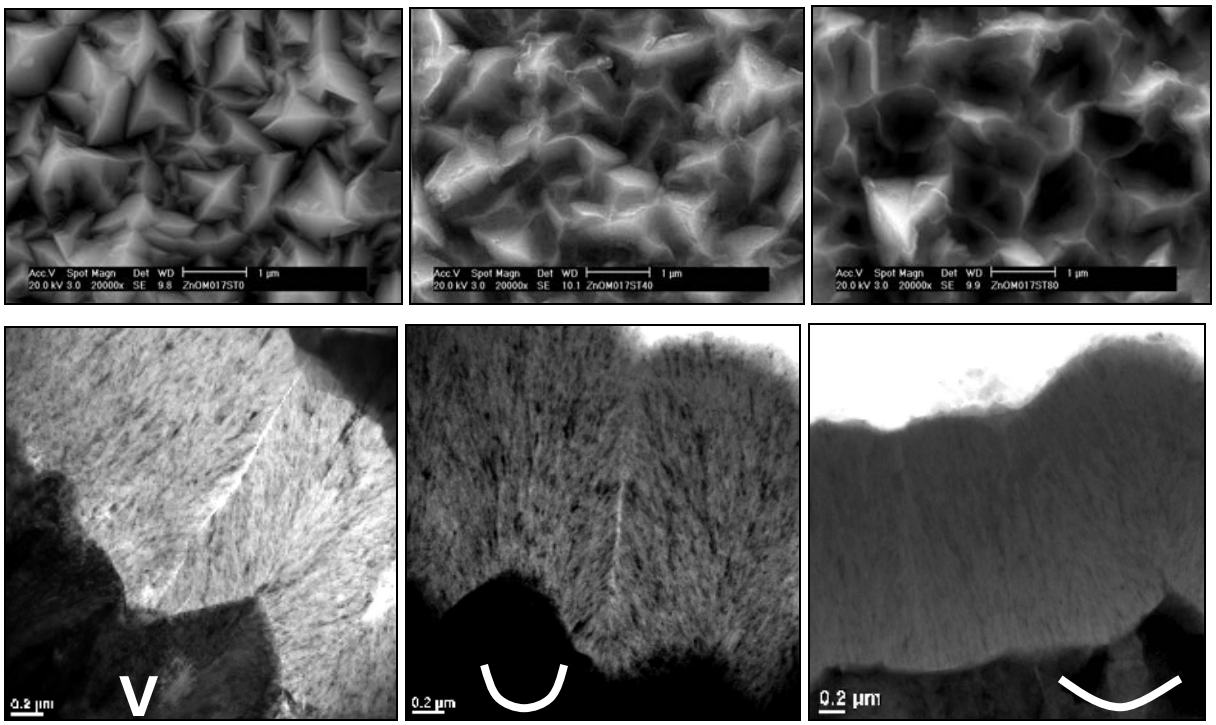

Figure 7.7: Up: SEM micrographs of ZnO surface. Down: bright field TEM cross-section micrographs of µc-Si:H p-i-n on substrates treated with increasing plasma treatment time (Left 0 min // Middle 40 min // Right 80 min).

An estimation of crack density has been derived from TEM measurements by counting the number of cracks of minimum 10 micrographs for every cell (over 50 microns). Five samples have been chosen for the estimation in the series presented above: cells deposited on untreated ZnO, ZnO treated 20 min, 40 min, 80 min, and 140 min. The crack density is presented as a function of the ZnO surface treatment time in Fig. 7.8.

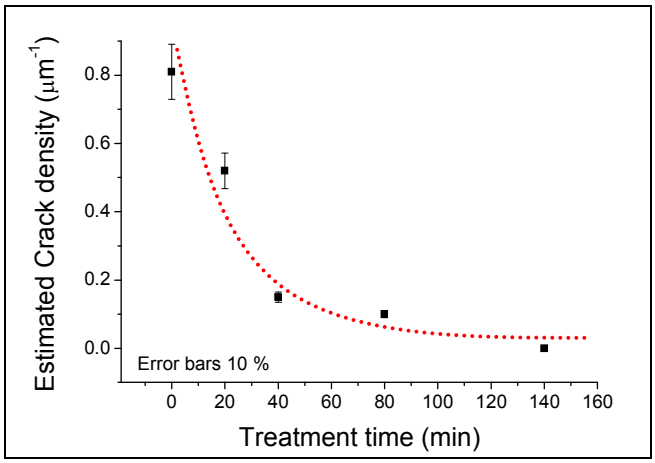

Figure 7.8: Estimation of crack density (obtained by TEM micrographs) for μc-Si:H cells on 5 TCOs of the treatment time series. The dotted line is a visual guide.

The crack density decreases very clearly with increasing ZnO treatment, as expected.
The relationship between the crack density within the intrinsic layer and the reverse saturation current density J_{02} is given in eq. 7.6:

$$J_{02} = n_l^2 \cdot I_{crack} \qquad (7.6)$$

with n_l the linear crack density per cm (given by the estimation of cracks with TEM micrographs) and I_{crack} the reverse saturation current of an individual crack.
If we plot J_{02} as a function of the crack density as in Fig. 7.9, we establish that the reverse saturation current for each crack is around $1.5 \cdot 10^{-13}$ A for intermediate cracks and $5.3 \cdot 10^{-12}$ A for crossing cracks in case of non-treated LPCVD ZnO.

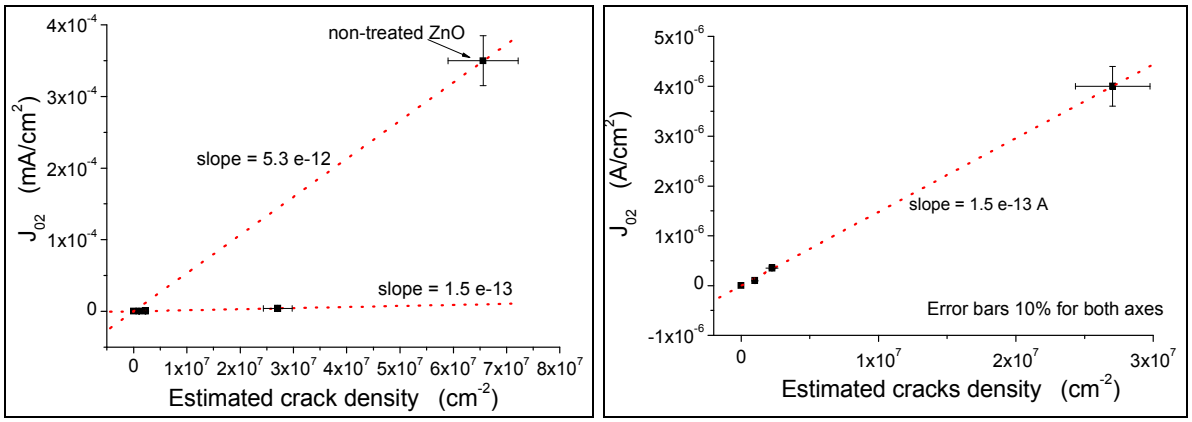

Figure 7.9: Relationship between the J_{02} and the crack density, for p-i-n configuration, estimated by TEM micrographs, in co-deposited µc-Si:H cells on varying substrates. Low J_{02} and low crack density is observed in high efficiency solar cells. On the right, one takes into account the crossing cracks observed for cells on non-treated ZnO.

Finally, Fig. 7.10 gives the variation of electrical parameters as a function of the estimated density of cracks. High values of V_{oc} and FF are confirmed to be related to a low density of cracks in the i-layer of the solar cells.

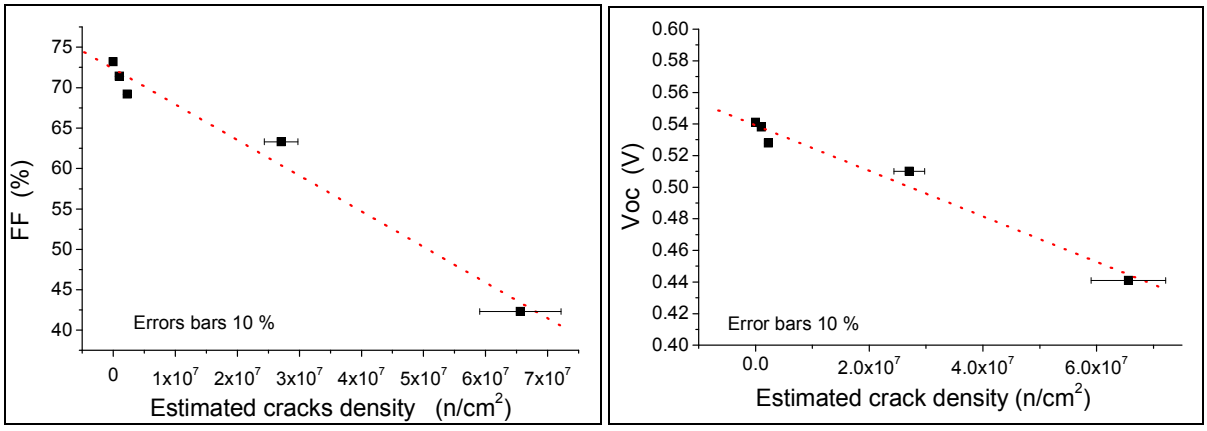

Figure 7.10: Increase of V_{oc} and FF with a decrease in the crack density; the latter has been evaluated from TEM micrographs. Red dotted lines are linear fits.

7.5. Discussion

The present Chapter illustrates the negative effect of the occurrence of cracks in µc-Si:H pin single junction solar cells on the electrical performance of the devices. In particular, V_{oc} and FF values decrease with increasing crack densities. The effect of the substrate's surface geometry on the occurrence of cracks is related to the occurrence of pinches on the substrate; these can be avoided by the modification of the substrate's geometry from V-shaped to U-shaped. It is necessary to add a second parallel diode to the usual equivalent electrical circuit to be able to fit the observed decrease in V_{oc} and FF. In this work, the non-defective part of the device is considered as a 'good' diode (diode

1: n_1 = 1.45, J_{01} = $1.1 \cdot 10^{-8}$ mA/cm^2) whereas the cracks are modeled by a 'defective' diode (diode 2: n_2 = 2, $J_{02} = n_1^2 \cdot I_{crack}$). With this novel equivalent circuit, we are able to fit very well the experimental "1 sun" and dark J(V) curves. Furthermore, the relationship between J_{02} and the estimated density of cracks seems to depend on whether or not the cracks cross through the silicon entire's thickness. Cracks that cross all layers (p–i–n) seem to be more destructive (I_{crack} = $5.3 \cdot 10^{-12}$ A) than cracks that end within the i-layer (I_{crack} = $1.5 \cdot 10^{-13}$ A).

In case of n-i-p configuration, the treatment of ZnO for microcrystalline silicon solar cells leads to similar observations, i.e. crack density can be reduced with the treatment of the ZnO and cracks act as a bad diode in the equivalent electrical circuit as illustrated in Fig. 7.11. This indicates that the mechanisms of crack formation and their role in the deterioration of the electrical properties are universal for all kind of devices.

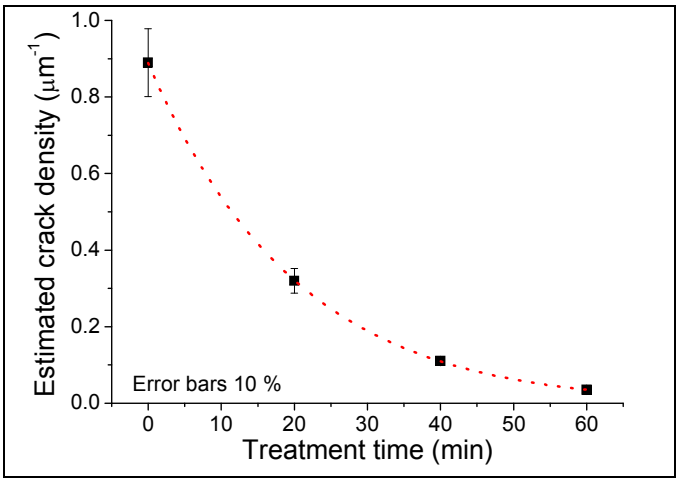

Figure 7.11: Estimation of crack density obtained by SEM micrographs (new method) for n-i-p µc-Si:H cells on 4 various treated TCOs. Dotted line is a visual guide.

Finally, we note that a similar study could be done on amorphous silicon, where cracks also appear. For instance, the problem of cracks appears in a-Si:H thin-film on complementary metal oxide semiconductors (CMOS) technology (TFC), in which amorphous silicon (a-Si:H) detectors are vertically integrated on top of a CMOS readout chip so as to form monolithic image sensors. Additional leakage currents are measured, because of cracks at the corner of the pixel [Miazza 2006].

Nevertheless, we think that the effect in a-Si:H solar cells is less detrimental than for µc-Si:H solar cells, because in the latter, the large thickness of µc-Si:H and weaker internal electrical field give more possibilities for the carriers to recombine in the area of the cracks. In addition, the specific microstructure (grains perpendicular to the substrate and crossing cracks) might lead to an enhancement of the recombination.

7.6. Conclusions

In this Chapter, the origin and effect of cracks on thin film microcrystalline solar cells is discussed. Previous TEM observations (Chapters 4 and 5) showed that V-shaped substrate morphologies result in a large density of cracks crossing the whole p-i-n solar cell, whereas U-shaped substrates lead to the growth of dense μc-Si:H. Characterization of the electrical performance of these devices by Variable illumination measurements (VIM) and dark J(V) measurements indicates that cracks act as diode-like shunts in the equivalent circuit of the solar cell. For the μc-Si:H solar cells studied here, the individual reverse saturation current is established to be about $1.5 \cdot 10^{-13}$ A per crack (non-crossing cracks). The "2 diodes" model is demonstrated to successfully allow us to simulate microcrystalline silicon solar cells by taking into account the cracks as an added bad diode. This is the case for both p-i-n and n-i-p solar cells configurations.

8. Effect of substrate temperature on µc-Si:H solar cells

8.1. Introduction

As already demonstrated in Chapter 7, cracks in microcrystalline silicon solar cells have mainly detrimental effects on the fill factor (FF) and open-circuit voltage (V_{oc}), and act as bad diodes with a high reverse saturation current. In Chapter 5, we attribute the creation of defects to the shadowing effect and to the low diffusion length of the adsorbed precursors, based on numerical simulations of the layer growth.
An existing approach to decrease crack density is to modify the surface morphology of the front ZnO (LP-CVD ZnO) from a V-shaped to a U-shaped by applying a surface treatment as discussed in Chapter 7. However, the surface treatment decreases the light scattering capabilities of the LPCVD ZnO because of the change in morphology (which we consider in a simplified way as reduction of roughness of the ZnO surface).
In this Chapter, a new method to decrease the crack density is presented: we show that an increase in substrate temperature during the deposition of intrinsic layer can improve its density. The increase of substrate temperature enhances the diffusion of precursors at the surface of the growing layer [Matsuda 1983]. The shadowing effect due to surface morphology is then lowered, because the particles can more easily reach the bottom of the pyramids. Other consequences of the increase in temperature (increase in crystallinity, decrease in open-circuit voltage (V_{oc}) and increase in FF) are presented and justified.

8.2. TCO used in this experiment

The substrates were prepared by depositing a 5 µm thick LPCVD-ZnO layer, from a vapor-gas mixture of water, diethyl-zinc and diborane, on an AF45 glass substrate from Schott. In order to achieve good electrical performance of the resulting solar cells, it was decided to perform a surface treatment as described in detail in Chapter 7: the surface morphology was subsequently modified by applying a plasma surface treatment on the ZnO layers for 40 min and 60 min.

8.3. Deposition of µc-Si:H with varying substrate temperature

µc-Si:H single junction solar cells were deposited on these substrates in a small area plasma-enhanced chemical vapor deposition (PECVD) reactor, working at

very-high excitation frequency (VHF) (122 MHz). The thickness of the µc-Si:H intrinsic layer is approximately 1.8 µm. The deposition of µc-Si:H was performed in p-i-n structure with the same p-layer and n-layer for every cell (same substrate temperature). Intrinsic layers were deposited at different substrate temperatures (controlled by the electrode temperature) from 170 °C to 270 °C in order to compare the influence of the substrate temperature on both electrical performances and crack formation.

8.4. Effect of substrate temperature on cracks

The influence of substrate temperature on µc-Si:H growth was already partly studied [Delli Veneri 2004], but the relationship between the substrate temperature and the electrical parameters were not completely established.
In this study, the effect of substrate temperature on electrical performances and an explanation based on the crack density is proposed. The latter was acquired using the original, fast and easy method for counting cracks, based on SEM observations, which was developed and used in this study. This new method is explained in detail in Chapter 2. Fig. 8.1 shows an example of the micrograph obtained.

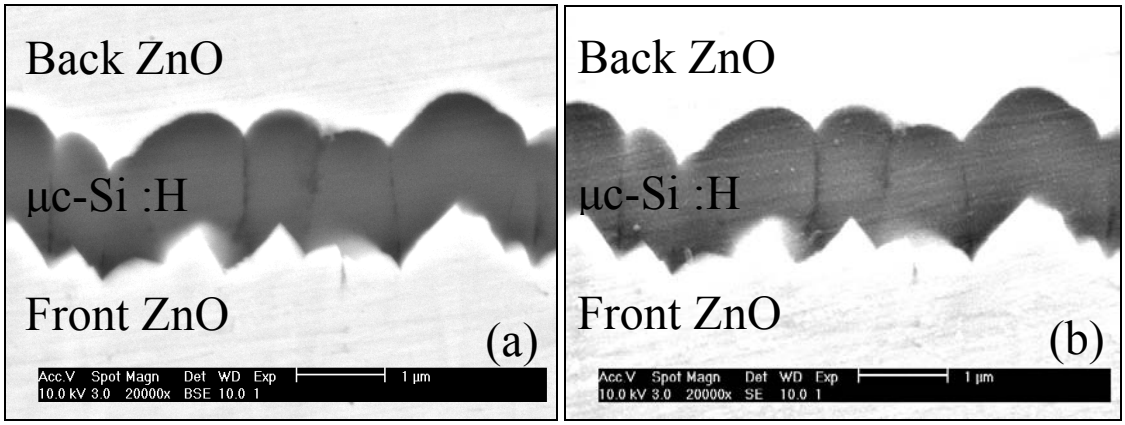

Figure 8.1: SEM on solar cell cross-section: µc-Si:H appears grey between front and back ZnO (light gray). Cracks appear as dark lines in silicon. (a) Micrograph obtained by electron back-scattered (EBS) detector. (b) Micrograph obtained by secondary electron (SE) detector.

The crack density was estimated over an observable area of more than 50 microns. As can be seen in Fig. 8.2, the crack density decreases from 0.23 crack/micron for deposition of the intrinsic layer at 170 °C to 0.13 crack/micron at 270 °C for µc-Si:H solar cells on ZnO treated for 40 min. The same behavior is observed for solar cells deposited on ZnO treated for 60 min, where the density of cracks decreases form 0.16 to 0.02 crack/micron. Hence, for both ZnO series, the increase of substrate temperature is linked to a decrease of crack

density. Note that for the same temperature, crack density is higher for solar cells deposited on ZnO treated 40 minutes compared to 60 minutes.

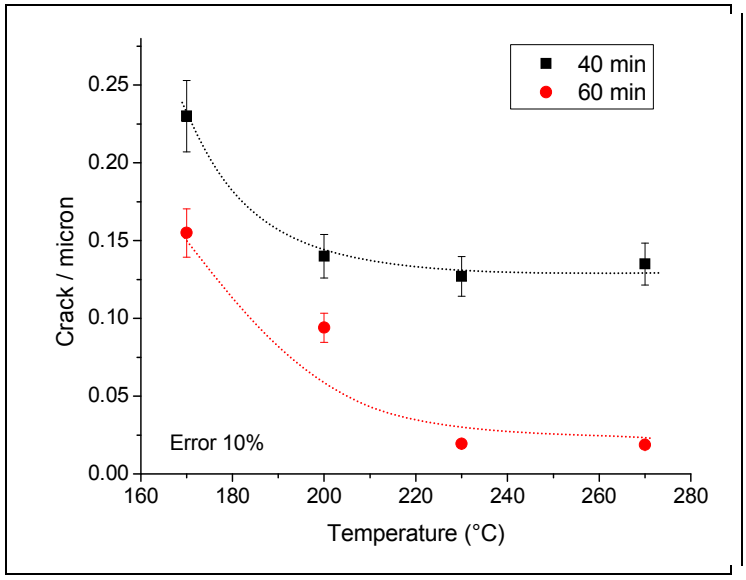

Figure 8.2: Decrease of crack density with the increase of substrate temperature. Dotted lines are visual guides.

The substrate temperature has a strong influence on the growth of microcrystalline silicon thin film by PECVD. As already seen in Chapter 7 and confirmed here, the treatment of the surface facilitates a decrease in the number of cracks, because the shadowing effect, due to roughness rms and "peak to valley", decreases and the collision of growing fronts is less strong than with V-shaped morphology.
The results in Fig. 8.2 do not follow an Arrhenius equation, but one can see that at low temperature, the increase of diffusion by increasing the substrate temperature decreases the crack density, whereas at higher temperature, the number of cracks is dependent on the substrate morphology (saturation of number of cracks).

8.5. Effect of substrate temperature on electrical performances

The Fig. 8.3a shows that fill factor (FF) increases on average from 67 % to 70 % for temperatures from 170 °C to 230 °C. As already seen in Chapter 7, the improvement of FF is expected with the decrease of crack density observed in Fig. 8.2. However, a decrease of V_{oc} is also observed in Fig. 8.3b. The next Section will explain this decrease with the help of micro-Raman spectroscopy.

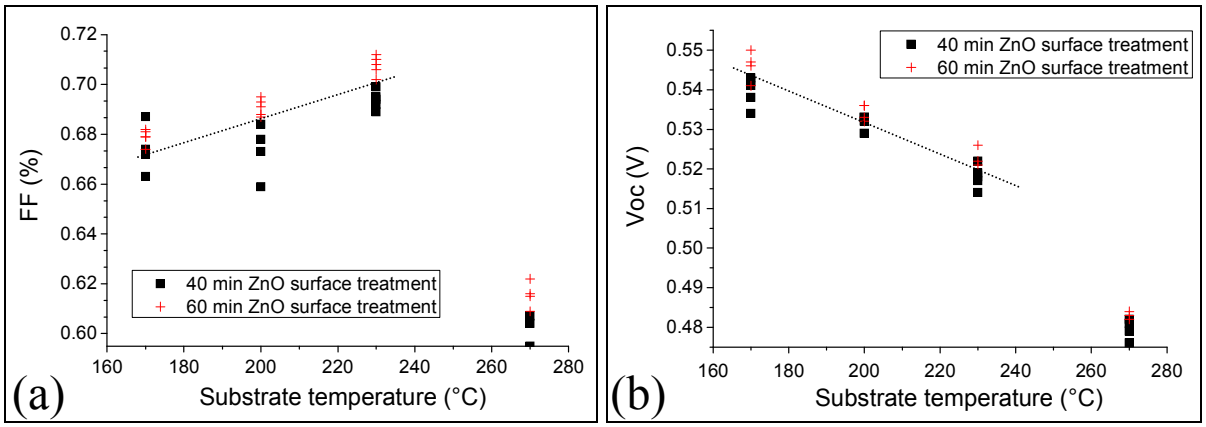

Figure 8.3: J(V) curve parameters obtained under one-sun illumination condition. (a) Increase of fill factor (FF) as a function of substrate temperature. (b) Decrease of V_{oc} as a function of substrate temperature. Dotted lines are visual guides.

Fig. 8.3 further demonstrates that the electrical performances of the solar cell deposited at the substrate temperature equal to 270°C are much lower. The poor values of V_{oc} and FF can be explained by Boron diffusion at the p-i interface due to high temperature at the beginning of the i-layer deposition. Fourier transform photocurrent spectroscopy (FTPS) measurements show that the quality of the microcrystalline material deposited at 270 °C is defective (zone 2 in Fig. 8.4). On the contrary, the quality of the material is high (low α(0.8eV) value) for samples deposited at 170, 200 and 230 °C (zone 1 in Fig. 8.4).

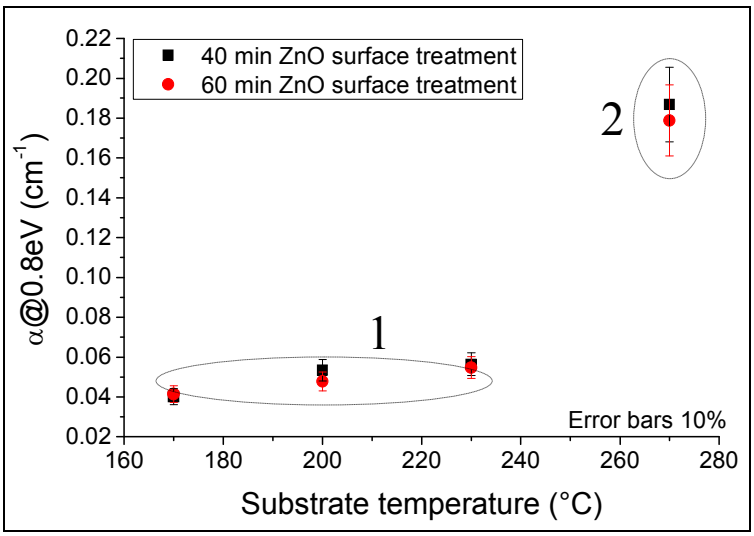

Figure 8.4: Results of FTPS measurement: absorption at 0.8 eV as a function of substrate temperature.

We can thus state that the improvement of the FF for temperatures between 170 °C and 230 °C is indeed attributed to the decrease of crack density observed in Fig. 8.2. Fig. 8.4 demonstrated that cracks do not influence the defect-related α, since the values are similar for solar cells deposited on both ZnO treated for 40 and 60 minutes.

8.6. Effect of substrate temperature on Raman crystallinity

Variations of micro-Raman crystallinity with substrate temperature are presented in Fig. 8.5. The increased substrate temperature induced an increased Raman crystallinity of the intrinsic layer, with a saturation to 50-55% at 270°C (average value).
Note that the measured Raman crystallinity is not constant in the microcrystalline cells. Indeed, the measurement at the beginning of the growth is lower (i.e. the material is more amorphous) than at the end. This is usually the case when no dilution profile is performed.

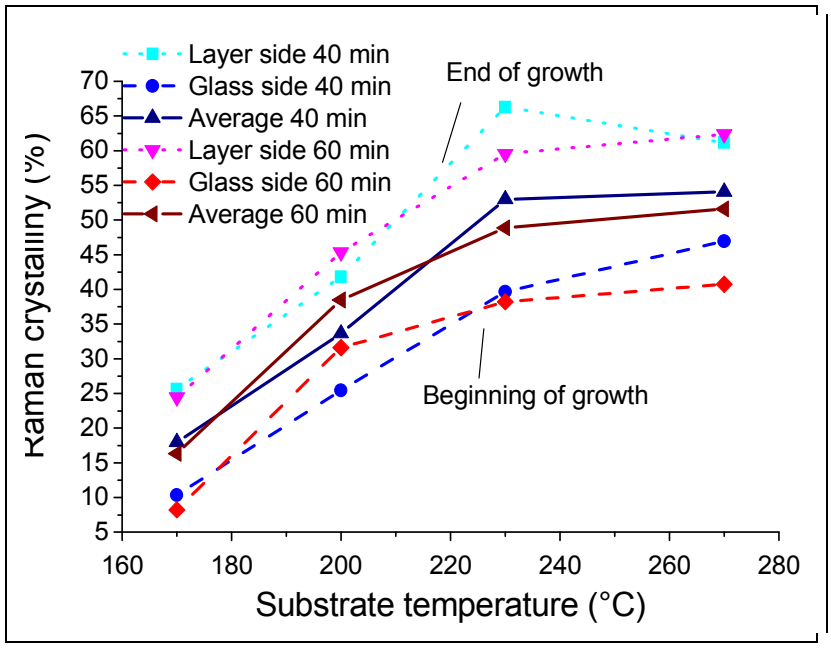

Figure 8.5: Raman crystallinity (with HeNe laser, 633 nm) increases as a function of substrate temperature with saturation at 270 °C.

The losses of V_{oc} observed in Fig. 8.3b can be related to the increase of crystallinity [Stiebig 1999, Droz 2004, Li 2005]. We suggest that the increase of temperature leads to a strong enhancement of the surface diffusion, leading to both an increase in crystallinity and to a filling of the cracks (see Section 8.8 for a more detailed discussion). The crystallinity is however not responsible for the variation of density of silicon (number of cracks), as we will show in the next Section.

8.7. Effect of silane concentration on cracks

A second series was prepared in order to verify the influence of the crystallinity on crack density at constant temperature (200°C). This µc-Si:H solar cell series, deposited on LP-CVD ZnO treated 20 minutes, was prepared by varying the

silane concentration (i.e. the flux of silane divided by the total gas flux) from 5.2% to 6.9% for the intrinsic layer. The same method: “1 face polishing” was finally performed in order to count the number of cracks. The Fig. 8.6 shows that the crack density is constant over the Raman crystallinity from 25 to 70 %.

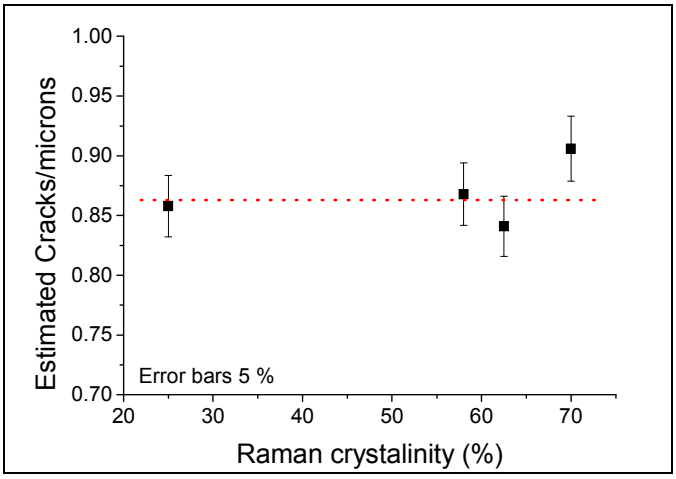

Figure 8.6: Effect of silane concentration (crystallinity) on density of microcrystalline silicon. Dotted line is a visual guide.

It is thus demonstrated with Fig. 8.6 that that the crystallinity does not influence the crack density.

8.8. Discussion

The treatment of the surface of the substrate facilitates a decrease in the number of cracks. Indeed, the solar cells deposited on ZnO60 have less cracks that on ZnO40. Moreover, the substrate temperature has a strong influence on the growth of µc-Si:H layers for thin film by PECVD: it is seen here that the number of cracks can also be decreased by increasing the substrate temperature during the intrinsic layer deposition. As seen in Fig. 8.2, the crack density decreases strongly between 170 °C and 270°C. However, a too high temperature (270 °C) leads to intrinsic layer contamination from the doped layers and to reduced i-layer quality, and, hence, to bad electrical solar cell performances (Fig. 8.3). For 170 °C, 200 °C and 230 °C, the increase of FF can be linked to the decrease in crack density.
In parallel, the crystallinity increases for the 3 first temperatures investigated and leads to a decrease of V_{oc} in the solar cell performances. The relation between the crystallinity and the V_{oc} is already well known [Droz 2004]. An optimization of Raman crystallinity is necessary to improve the electrical performance of the solar cells deposited at higher temperatures in order to benefit to both the increase of FF and high V_{oc}. It is also demonstrated with Fig. 8.6 that the crystallinity does not influence the crack density. Hence, we can

attribute univocally the crack reduction to the increase in temperature and not to the increase in crystallinity. It would seem that the surface diffusion of silicon is increased and the closing of voids is performed better, assuming that substrate temperature has only negligible effect on the plasma composition. This is in agreement with the growth simulation presented in Chapter 5.
Interestingly, our results give some indication on the local growing mechanisms, as the a-Si to μc-Si transition is usually attributed either to an enhancement of the surface diffusion of the SiH_x precursors [Matsuda 1999] or to other models more related to hydrogen interaction at the surface (selective etching and chemical annealing) [Tsai 1989, Teresa 2000, Teresa 2002, Van Oort 1987]. In our case, the increase of the molecular hydrogen input flow at constant temperature leads to an increase of crystallinity because the composition of the flow reaching the surface starts to dominate (but the surface diffusion remains moderate). Whereas, for constant radical flows, the increase of temperature leads to a strong enhancement of the surface diffusion, leading both to an increase in crystallinity and to a filling of the cracks.
Finally, the devices presented in this study are not optimized. In particular it would be necessary to control the crystallinity of the solar cells in order to keep a high value of V_{oc} in the electrical parameters. Also, micromorph (tandem) cells could benefit from the improvement of crack density in the n-i-p configuration, where the p-layer could be fabricated at lower temperature. Indeed, micromorph p-i-n structures require the deposition of amorphous silicon first and then, the high substrate temperature for the intrinsic layer of microcrystalline may lead to interface contamination by boron doping diffusion.

8.9. Conclusion

The decrease in crack density is a key point for developing high efficiency thin film μc-Si:H solar cells. To increase the density of μc-Si:H material, one way is to modify the substrate morphology from a V-shaped to a U-shaped, but this will influence the scattering of the light, and hence, the short-circuit current density of the solar cells. In this Chapter, we show that by increasing the substrate temperature during the intrinsic layer deposition, the crack density can be further decreased, without any influence on the scattering of the light, because the surface morphology of the substrate is not changed. We attribute the closing of the crack to an enhanced surface diffusion of the Si atoms, which is favored by the higher growth temperature. We also show that, at constant deposition temperature, the crack density is independent of the crystalline fraction. Hence, our results tend to show that the enhancement of the surface diffusion of the Si adatoms by the higher molecular hydrogen flow is not as efficient as obtained by the higher temperature. Finally, our findings allow us to give guidelines for the fabrication of higher efficiency single junction and multiple-junction devices.

9. Conclusions and perspectives

The μc-Si:H thin film solar cells were studied in order to improve the understanding between the growth and the electrical properties. In particular, the effect of cracks in the microcrystalline cell was extensively investigated: the origin of these cracks as well as their influence on the electrical model has been highlighted.

An investigation into the nature of the cracks has been performed. Cracks are zones of porous material that appear above a V-shaped morphology, due to oblique incident of adatoms, shadowing, perpendicular growth of μc-Si:H on the surface, and diffusion of adatoms at the growing surface. Porous material is silicon containing nanovoids, which seems to be smaller than 50 nm in diameter (HRTEM micrographs with a 50 nm thick sample do not show any lack of material near and above the cracks). Crossing cracks (cracks which cross p-i-n layers) are more detrimental than cracks which begin in the middle of the intrinsic layer.
It was observed that V_{oc} and FF increase in single junction μc-Si:H p-i-n solar cells with a smoothed wafer surface or treated ZnO. This result confirms previous observations made for p-i-n single junction solar cells. **The increase in electrical performances is related to a decreasing density of cracks** in the silicon layers. Comparison between electrical measurements and a TEM micrograph was performed. With experimental measurements, two features of the substrate morphology lead to a decreased crack density:

1) fewer small-sized structures lying in a disorderly manner in-between large-sized pyramids
2) smoothed substrate's valley, from V-shaped to U-shaped

In consequence, according to our experimental observations, an ideal substrate for dense μc-Si:H growth should possess large uniform structures with U-shaped valleys or reasonable opening angles. Such substrates could lead to high V_{oc} and high FF devices, while maintaining a high current.

The decrease in crack density is then a key point for developing high efficiency thin film μc-Si:H solar cells. To increase the density of μc-Si:H material, one way is thus to modify the substrate morphology from V-shaped to U-shaped, but this will influence the scattering of the light, and hence, the short-circuit current density of the solar cells.
It is shown that by **increasing the substrate temperature** during the intrinsic layer deposition, the **crack density can be further decreased**, without any

influence on the light scattering, because the surface morphology of the substrate is not changed. We attribute the closing of the crack to an enhanced surface diffusion of the Si atoms, which is favored by the higher growth temperature. The increase of substrate temperature has shown interesting decrease in crack density. However, the crystallinity has increased as well, leading to a decrease in open-circuit voltage. An optimization of crystallinity for temperatures around 230°C should thus help to increase the V_{oc}. We expect that the combination of low crack density and optimal crystallinity will produce microcrystalline silicon solar cells with high efficiency.

In parallel, the effect of several substrate morphologies on microcrystalline silicon growth was investigated by the simulation program called MANEMO. It was shown numerically that the morphology of the substrate as well as the **number of diffusion steps** play an important role for the formation of the cracks. Because the main substrate in Neuchâtel is LP-CVD ZnO with a natural pyramidal shape, 2 parameters of these pyramidal substrates were investigated: **angle of the pyramids** as well as **curvature radii at the valley of the pyramids** were found to be related to crack density. The decrease of the angle leads to a decrease in crack density and the increase of the curvature radii leads to a decrease in crack density.

The electrical model proposed by Merten et al. [Merten 1998] and used by Meillaud et al. for μc-Si:H solar cells [Meillaud 2006], does not take into account such cracks. In this thesis, a new equivalent electrical circuit was presented which takes into account the crack density of the solar cells. This new model adds a recombination diode in parallel to the circuit. By modifying the reverse saturation current of this diode, the J(V) curve of a series of cells containing various densities of cracks could fit successfully. This experiment has demonstrated that **cracks act as recombination diode in the solar cells**, and this was also confirmed for devices in the n-i-p structure.

The analysis of these cracks can thus be performed with the help of electron microscopy: TEM micrographs are suitable to count the number of cracks and thus estimate the crack density. However, the preparation for such a TEM sample is time consuming. Thus, a new method was developed and is presented: "**1 face polishing**". The preparation is 4 times faster than conventional TEM preparation. The samples, observable with SEM, are suitable for counting the number of cracks.

As already mentioned, an analysis of these cracks for amorphous silicon solar cells would be interesting to find out the influence of these latter on electrical performances. Even if their influence should be lower due to the isotropic orientation of amorphous silicon, the smaller thickness as well as the stronger

electrical field, the zone of porous material should also behave like a defective diode and then decrease the V_{oc} and FF.
The morphology of an ideal substrate for microcrystalline silicon has to be defined in order to achieve the highest efficiency conversion for µc-Si:H solar cells. In this work, some parameters are given (reasonable opening angle, high curvature radii), but other ones like the influence of smooth, periodical structures or other morphologies should be explored.

Micromorph cells (tandem cell with amorphous and microcrystalline cells) also have the problem of cracks. Indeed, the microcrystalline cell is deposited on a rough TCO in n-i-p configuration, leading to cracks as described in this thesis. For p-i-n configuration, the microcrystalline cell is deposited on the amorphous cell, which also exhibits pinches on its surface morphology. This surface is critical and cannot be modified as simply as the TCO, because the last layer in the n-doped layer and plasma treatment can damage the quality of the layers. Here, the increase of substrate temperature is a possible way to decrease the cracks, but too high a temperature can lead to annealing of amorphous cells and diffusion of doping from doped layers to the intrinsic layer. For multi-junction containing intermediate reflectors, we can imagine a treatment of this layer in order to prepare an optimal surface for the deposition of the next cell.

The simulation software could be improved in order to be able to simulate the growth of a micromorph cell or multiple junctions. For now, only one layer can be simulated at once. However, we can imagine adding an option that permits to the software to keep the first layer deposited in memory, before depositing the second one, and so on. Then, the effect of cracks could be analyzed directly in the simulation program.

Acknowledgments

This work was supported by the Swiss National Science Foundation under grant SNSF 200020-116630 and the Swiss Federal Office of Energy under contract 101191.

I would like to thank Prof. A. Shah for the opportunity he gave me to do my Ph.D thesis in the PV-Lab and for the interesting discussions and advices. Also, I wish to thank Prof. C. Ballif for confirming my position within the group at the time of the succession. I greatly appreciated his trust and help during these 4 years and his role of supervisor during the second part of my thesis work.

Special thanks to Dr. F. Sculati-Meillaud and Assoc. Prof. E. Vallat-Sauvain for supervising and correcting my thesis and the papers I wrote during these years. It was a real chance for me to have the opportunity to work with both of you.

I wish to thank my referees Prof. Miro Zeman, Dr. P. Thomann and A. Poruba for joining the examination board and for their constructive remarks. They helped me to improve this thesis.

I am grateful to Mrs. Leboeuf, Dr. Dadras and Dr. V. Spassov for their advices in sample preparation and microscopy. They were always available for discussions and teached me a lot in this field.

I would like to warmly thank the group of Prof. M. Vanecek for welcoming me for three weeks in the research group at the Czech Academy of Sciences in Praha. The group and in particular J. Holovski and A. Poruba helped me a lot to learn the subtleties of the FTPS measurements.

The work done during this thesis would not have been possible without the interaction with my colleagues at PV-Lab. since, the major part of the solar cells investigated during this work were deposited by some of them. So, I would like to sincerely thank J. Bailat, D. Dominé, P. Buehlmann, A. Feltrin, X. Niquille, L. Feitkneicht, F. Haug, S. De Wolf, and O. Madani. Of course, the other members of the group were also crucial for all the work and "extra-work" support, which I don't want to mention here… I think in particular of S. Dunand, F. Jeanneret, X. Niquille, A. Billet, S. Olibet, C. Denizot, J. Steinhauser, S. Pelisset, and J. Damon-Lacoste.

Finally, I would like to thank my family for their constant support during all these years of studies, and my girlfriend for her advices and her motivation.

References

[Abolhassani 2006] S. Abolhassani and P. Gasser, Preparation of TEM samples of metal–oxide interface by the focused ion beam technique, Journal of Microscopy, 223 (2006) 73-82.

[Bailat 2003] J. Bailat, E. Vallat-Sauvain, L. Feitknecht, C. Droz, and A. Shah, Microstructure and Open-Circuit Voltage of n-i-p Microcrystalline Silicon Solar Cells, Journal of Applied Physics, 93 (2003) 5727-5732.

[Bailat 2004] J. Bailat thesis, University of Neuchâtel, (2004)

[Bailat 2004a] J. Bailat, E. Vallat-Sauvain, A. Vallat, A. Shah, Simulation of the growth dynamics of amorphous and microcrystalline silicon, Journal of Non-Crystalline Solids, 338-340 (2004) 32-36.

[Bailat 2004b] J. Bailat, E. Vallat-Sauvain, A. Vallat and A. Shah, Phase diagrams and microstructure of microcrystalline and amorphous silicon studied by dynamical simulation of the growth of microcrystalline silicon, Materials Research Society Symposium Proceedings, 808 (2004) 221-226.

[Bailat 2006] J. Bailat, D. Dominé, R. Schlüchter, J. Steinhauser, S. Faÿ, F. Freitas, C. Bücher, L. Feitknecht, X. Niquille, T. Tscharner, A. Shah, C. Ballif, High-efficiency p-i-n microcrystalline and micromorph thin film silicon solar cells deposited on LPCVD ZnO coated glass substrates, Proceedings of the 4th WCPEC Conference, (2006) 1533-1536.

[Barabasi 1995] A.L. Barabasi and H.E. Stanley, Fractal Concepts in Surface Growth, Cambridge University Press, ISBN 0-521-48318-2, 1995

[Beck 1996] N. Beck, J. Meier, J. Fric, Z. Remeš, A. Poruba, R. Flückiger, J. Pohl, A. Shah, M. Vanecek, Enhanced Optical Absorption in Microcrystalline Silicon, Journal of Non-Crystalline Solids 198-200 (1996) 903-906.

[Belsky 2005] P Belsky, R Streiter, H Wolf, T Gessner, Application of Molecular Dynamics to the Simulation of IPVD, Advanced Metallization Conference 2004, San Diego CA, U.S.A., 2004 Oct 19-21; MRS Conf. Proc. AMC XX, Material Research Society, Warrendale PA (2005), pp 787-792 (ISBN 1-55899-814-4 / ISSN 1048-0854)

[Benedict 1992] J. Benedict, R. Andersen and S.J. Klepeis, Recent Developments in the Use of the Tripod Polisher for TEM Specimen Preparation, Proc. Mater. Res. Soc. Symp. 254 (1992) 121-140.

[Binnig 1987] G. K. Binnig, Atomic-Force Microscopy, Physica Scripta. T19 (1987) 53-54.

[Chatterjee 1995] P.K. Chatterjee, W.R. Hunter, A. Amerasekera, S. Aur, C. Duvvury, P.E. Nicollian, L.M. Ting, P. Yang, Trends for deep submicron VLSI and their implications for reliability, Reliability Physics Symposium, 33rd Annual Proceedings, IEEE International (1995) 1-11.

[Chittick 1969] R.C. Chittick, J.H. Alexander, and H.F. Sterling, The Preparation and Properties of Amorphous Silicon, J. Electrochem. Soc., 116(1) (1969) 77-81.

[Collins 2003] R.W. Collins, A.S. Ferlauto, G.M. Ferreira, C. Chen, J. Koh, R.J. Koval, Y. Lee, J.M. Pearce and C.R. Wronski, Evolution of microstructure and phase in amorphous, protocrystalline, and microcrystalline silicon studied by real time spectroscopic ellipsometry, Solar Energy Materials and Solar Cells, 78 (2003) 143-180.

[Curtins 1987] H. Curtins, N. Wyrsch, and A. Shah, High-rate deposition of amorphous hydrogenated silicon: effect of plasma excitation frequency, Electronic Letters, 23 (1987) 228.

[Delli Veneri 2004] P. Delli Veneri, L. V. Mercaldo, E. Bobeico, P. Spinillo, C. Privato, 19th European Photovoltaic Solar Energy Conference, Paris (2004) 1469.

[Despeisse 2008] M. Despeisse, G. Anelli, P. Jarron, J. Kaplon, D. Moraes, A. Nardulli, F. Powolny, N. Wyrsch, Hydrogenated Amorphous Silicon Sensor Deposited on Integrated Circuit for Radiation Detection, Transactions on Nuclear Science, 55 (2008) 802-811.

[Dew 1991] S.K. Dew, T. Smy, R.N. Tait and M.J Brett, Modeling bias sputter planarization of metal films using SIMBAD, J. Vac. Sci. Technol. A, 9(3) (1991) 519-523.

[Dominé 2007] D. Dominé, J. Bailat, M. Python, N. Wyrsch, C. Ballif, H. R. Moutinho, C.-S. Jiang, M. M. Al-Jassim, Investigation of the Electric-Field Profile in Microcrystalline Silicon p-i-n Solar Cells by Cross-Sectional Scanning Kelvin Probe Microscopy, Proceedings of the 22nd EU-PVSEC, Milan, (2007).

[Dominé 2008] D. Dominé, P. Buehlmann, J. Bailat, A. Billet, A. Feltrin, and C. Ballif, Optical management in high-efficiency thin-film silicon micromorph solar cells with a silicon oxide based intermediate reflector, Phys. stat. sol., 2(4) (2008) 163–165.

[Donker 2006] M.N. van den Donker, R. Schmitz, W. Appenzeller, B. Rech, W.M.M. Kessels, M.C.M. van de Sanden, The role of plasma induced substrate heating during high rate deposition of microcrystalline silicon solar cells, Thin Solid Films 511-512 (2006) 562-566.

[Droz 2003] C. Droz thesis, University of Neuchâtel, (2003)

[Droz 2004] C. Droz, E. Vallat-Sauvain, J. Bailat, L. Feitknecht, J. Meier, A. Shah, Relationship between Raman crystallinity and open-circuit voltage in microcrystalline silicon solar cells, Solar Energy Materials and Solar Cells, 81 (2004) 61-71.

[Faÿ 2000] S. Faÿ, S. Dubail, U. Kroll, J. Meier, Y. Ziegler, A. Shah, Light Trapping Enhancement for Thin-Film Silicon Solar Cells by Roughness Improvement of the ZnO Front TCO, Proceedings of the 16th EC Photovoltaic Solar Energy Conference, (2000) 361-364.

[Faÿ 2003] S. Faÿ thesis, University of Neuchâtel, (2003)

[Faÿ 2006] S. Faÿ, L. Feitknecht, R. Schlüchter, U. Kroll, E. Vallat-Sauvain, A. Shah, Rough ZnO layers by LP-CVD process and their effect in improving performances of amorphous and microcrystalline silicon solar cells, Solar Energy Materials and Solar Cells, 90 (2006) 2960-2967.

[Fejfar 1996] A. Fejfar, A. Poruba, M. Vanecek, J. Kocka, Precise measurement of the deep defects and surface states in a-Si:H films by absolute CPM, Journal of Non-Crystalline Solids, 198-200 (1996) 304-308.

[Feitknecht 2005] L. Feitknecht, J. Steinhauser, R. Schlüchter, S. Faÿ, D. Dominé, E. Vallat-Sauvin, F. Meillaud, C. Ballif, A. Shah, Investigations on Fill-Factor drop of microcrystalline silicon p-i-n solar cells deposited onto highly surface-textured ZnO substrates, Technical digest of the 15th International Photovoltaic Science and Engineering Conference, 1 (2005) 473-474.

[Fichthorn 1991] K.A. Fichthorn and W.H. Weinberg, Theoretical foundations of dynamical Monte Carlo simulations, J. Chem. Phys., 95(1991) 1090-1096.

[Goerlitzer 1997] M. Goerlitzer, N. Beck, P. Torres, U. Kroll, H. Keppner, J. Meier, j. Koehler, N. Wyrsch, and A. Shah, Electronic Transport and Structure of Microcrystalline Silicon Deposited by the VHF-GD Technique, Mat. Res. Soc. Symp. Proc. 467 (1997) 301-306.

[Goerlitzer 1998] M. goerlitzer, P. Torres, N. Beck, N. Wyrsch, U. Kroll, H. Keppner, J. Pohl and A. Shah, Structural Properties and Electronic Transport in Intrinsic Microcrystalline Silicon Deposited by the VHF-GD Technique, J. Non-Crystalline Solids, 227-230 (1998) 996-1000.

[Goldstein 2003] J. Goldstein, D.E. Newbury, P. Echlin, C.E. Lyman, D.C. Joy, E. Lifshin, L.C. Sawyer, J.R. Michael, Scanning Electron Microscopy and X-ray Microanalysis, ISBN 0306472929, Published by Springer, 2003.

[Graf 2003] U. Graf, J. Meier, U. Kroll, J. Bailat, C. Droz, E. Vallat-Sauvain, A. Shah, High Rate Growth of Microcrystalline Silicon by VHF-GD at High Pressure, Thin Solid Films 427 (2003) 37-40.

[Green 2008] M.A. Green, K. Emery, Y. Hishikawa and W. Warta, Solar Cell Efficiency Tables (Version 32), Progress in Photovoltaics: Research and Applications, 16 (2008) 345-440.

[Grundmann 2005] M. Grundmann, The bias dependence of the non-radiative recombination current in p–n diodes, Solid-State Electronics, 49(8) (2005) 1446-1448.

[Hamaguchi 1993] S. Hamaguchi, M. Dalvie, R.T. Farouki, and S. Sethuraman, A shock-tracking algorithm for surface evolution under reactive-ion etching, J. Appl. Phys., 74 (1993) 5172-5184.

[Heintze 1996] M. Heintze, R. Zedlitz, H. N. Wanka, and M. B. Schubert, J. Appl. Phys., 79 (1996) 2699-2706.

[Hod'áková 2006] L. Hod'áková, A. Poruba, R. Kravets, M. Vanecek, Fast quantum efficiency measurement of solar cells by Fourier transform photocurrent spectroscopy, Journal of Non-crystalline Solids 352 (2006) 1221-1224.

[Houben 1998] L. Houben, M. Luysberg, P. Hapke, R. Carius, F. Finger, H. Wagner, Structural properties of microcrystalline silicon in the transition from highly crystalline to amorphous growth, Philosophical Magazine A, 77(6) (1998) 1447-1460.

[Ikegawa 1989] M. Ikegawa and J. Kobayashi, Deposition Profile Simulation Using the Direct Simulation Monte Carlo Method, J. Electrochem. Soc., 136(10) (1989) 2982-2986.

[Keppner 1999] H. Keppner, J. Meier, P. Torres, D. Fischer and A. Shah, Microcrystalline silicon and micromorph tandem solar cells, Applied Physics A – Material Science & Processing, 69 (1999) 169-177.

[King 1994] D.L. King, W.K. Schubert, T.D. Hund, World's First 15 % Efficient Multicrystalline Silicon Modules, Conference record, 1st World Conference on Photovoltaic Energy Conversion, Hawaï, (1994) 1660-1662.

[Klein 2001] S. Klein, F. Finger, R. Carius, H. Wagner and M. Stutzmann, Intrinsic amorphous and microcrystalline silicon by hot-wire-deposition for thin film solar cell applications, Thin Solid Films, 395(1-2) (2001) 305-309.

[Klein 2003] S. Klein, F. Finger, R. Carius, T. Dylla, B. Rech, M. Grimm, L. Houben and M. Stutzmann, Intrinsic microcrystalline silicon prepared by hot-wire chemical vapour deposition for thin film solar cells, Thin Solid Films, 430(1-2) (2003) 202-207.

[Klein 2007] S. Klein, F. Finger; R. Cariu, T. Dylla, J. Klomfass, Relationship between the optical absorption and the density of deep gap states in microcrystalline silicon, Journal of Applied Physics, 102 (2007) n°103501.

[Kroll 1996] U. Kroll, J. Meier, A. Shah, S. Mikhailov and J. Weber, Hydrogen in amorphous and microcrystalline silicon films prepared by hydrogen dilution, Journal of applied Physics, 80 (1996) 4971-4975.

[Li 1995] J. Li, J.P. McVittie, J. Ferziger, K.C. Saraswat, J. Dong, Optimization of intermetal dielectric deposition module using simulation, J. Vac. Sci. Technol. B, 13(4) (1995) 1867-1874.

[Li 2005] Y.-M. Li, L. Li, J.A. Anna Selvan, A.E. Delahoy and R.A. Levy, Effects of seeding methods on the fabrication of microcrystalline silicon solar cells using radio frequency plasma enhanced chemical vapor deposition, Thin Solid Films, 483(1-2) (2005) 84-88.

[Li 2008] H. Li, R. Franken, R.L. Stolk, J.K. Rath, R.E.I. Schropp, Mechanism of Shunting of Nanocrystalline Silicon Solar Cells Deposited on Rough Ag/ZnO Substrates, Solid State Phenomena, 131-133 (2008) 27-32.

[Lihui 2000] G. Lihui and L. Rongming, Studies on the formation of microcrystalline silicon with PECVD under low and high working pressure, Thin Solid Films, 376(1-2) (2000) 249-254.

[Löffler 2005] J. Löffler, A. Gordijn, R.L. Stolk, H. Li, J.K. Rath, R.E.I. Schropp, Amorphous and 'micromorph' silicon tandem cells with high open-circuit voltage, Solar Energy Materials & Solar Cells 87 (2005) 251–259.

[Luysberg 1997] M. Luysberg, P. Hapke, R. Carius, F. Finger, Structure and growth of hydrogenated microcrystalline silicon : investigation by transmission electron microscopy and Raman spectroscopy of films grown at different plasma excitation frequencies, Philosophical Magazine A, 75(1) (1997) 31-47.

[Luysberg 2001] M. Luysberg, C. Scholten, L. Houben, R. Carius, F. Finger, and O. Vetterl, Structural Properties of Microcrystalline Si Solar Cells, Mat. Res. Soc. Symp. Proc. 664 (2001) A15.2.1.

[Lyka 2005] B Lyka, E. Amanatides, D. Mataras and D.E. Rapakoulias, Power consumption effect on the microcrystalline silicon deposition process: a comparison between model and experimental results, Journal of physics: Conference series, 10 (2005) 198-201.

[Markvart 2000] T. Markvart, Solar electricity 2nd ed. (John Wiley & sons, 2000). ISBN 0-471-98853-7.

[Mataras 2002] D. Mataras, E. Amanatides, D.E. Rapakoulias, Combination of plasma diagnostics and modelling for the investigation of microcrystalline silicon deposition process, Conference Record of the Twenty-Ninth IEEE, (2002) 1158-1161.

[Matsuda 1983] A. Matsuda, Formation kinetics and control of microcrystallite in μc-Si:H from glow discharge plasma, Journal of Non-Crystalline Solids, 59/60 (1983) 767-774

[Matsuda 1999] A. Matsuda, Growth mechanism of microcrystalline silicon obtained from reactive plasmas, Thin Solid Films, 337(1-2) (1999) 1-6.

[McCaffrey 1991] J. P. Mc Caffrey, Small-angle cleavage of semiconductors for transmission electron microscopy, Ultramicroscopy, 38(2) (1991) 149-157.

[McVittie 1990] J.P. McVittie, J.C. Rey, M.M. IslamRaja, L.Y. Cheng and K.C. Saraswat, LPCVD Profile Simulations Using a Re-Emission Model, IEEE International Electron Devices Meeting, (1990) 917-920.

[Meier 1994] J. Meier, S. Dubail, R. Fliickiger, D. Fischer, H. Keppner, A. Shah, Intrinsic Microcrystalline Silicon (μc-Si:H)- a Promising New Thin Film Solar Cell Material, Proceedings of the 1st World Conference on Photovoltaic Energy Conversion, (1994) 409-412.

[Meier 2004] J. Meier, J. Spitznagel, U. Kroll, C. Bucher, S. Faÿ, T. Moriarty, A. Shah, Potential of Amorphous and Microcrystalline Silicon Solar Cells, Thin Solid Films, 451-452 (2004) 518-524.

[Meillaud 2005] F. Meillaud, E. Vallat-Sauvain, X. Niquille, M. Dubey, A. Shah, C. Ballif, Light-Induced Degradation of Thin-Film Microcrystalline Silicon Solar Cells, Proceedings of the 20th EU Photovoltaic Solar Energy Conference, ISBN 3-936338-19-1, Barcelona, Spain, (2005) 1509-1512.

[Meillaud 2006] F. Meillaud thesis, University of Neuchâtel, (2006)

[Meillaud 2006a] F. Meillaud, A. Shah, C. Droz, E. Vallat-Sauvain, C. Miazza, Efficiency limits for single-junction and tandem solar cells, Solar Energy Materials & Solar Cells, 90 (2006) 2952–2959.

[Meillaud 2006b] F. Meillaud, A. Shah, J. Bailat, E. Vallat-Sauvain, T. Roschek, B. Rech, D. Dominé, T. Söderström, M. Python, C. Ballif, Proc. of the 4th WCPEC Conf., (2006), 1572

[Meillaud 2006c] F. Meillaud, E. Vallat-Sauvain, X. Niquille, M. Dubey, A. Shah and C. Ballif, Proton-induced degradation of Thin-Film Microcrystalline Silicon Solar Cells, Journal of Non-Crystalline Solids, 352(9-20) (2006) 1851-1854.

[Merten 1998] J. Merten, J.M. Asensi, C. Voz, A. Shah, R. Platz, J. Andreu, Improved equivalent circuit and analytical model for amorphous silicon solar cells and modules, IEEE Transactions on Electron Devices, 45 (1998) 423-429.

[Miazza 2004] C. Miazza, S. Dunand, N. Wyrsch, A. Shah, N. Blanc, R. Kaufmann, L. Cavalier, Performance analysis of a-Si:H detectors deposited on CMOS chips, Mat. Res. Soc. Symp. Proc., 808 (2004) 513-518.

[Müller 2001] J. Müller, G. Schöpe, O. Kluth, B. Rech, M. Ruske, J. Trube, B. Szyszka, X. Jiang, G. Bräuer, Upscaling of texture-etched zinc oxide substrates for silicon thin film solar cells, Thin Solid Films, 392 (2001) 327-333.

[Nakamura 1995] K. Nakamura, K. Yoshida, S. Takeoka, I. Shimizu, Roles of Atomic Hydrogen in Chemical Annealing, Jpn. J. Appl. Phys., 34 (1995) 442-449.

[Nasuno 2000] Y. Nasuno, M. Kondo, A.. Matsuda, Microcrystalline silicon thin-film solar cells prepared at low temperature using RF-PECVD, Photovoltaic Specialists Conference, Conference Record of the Twenty-Eighth IEEE, ISBN: 0-7803-5772-8, (2000) 142-145.

[Nasuno 2001]. Y. Nasuno, M. Kondo and A. Matsuda, Effects of Substrate Surface Morphology on Microcrystalline Silicon Solar Cells, Japanese Journal of Applied Physics, 40 (2001) 303-305.

[Nasuno 2002] Y. Nasuno, M. Kondo, A. Matsuda, Microcrystalline silicon thin-film solar cells prepared at low temperature using PECVD, Solar Energy Mat. & Solar Cells, 74 (2002) 497-503.

[Oldham 1979] W.G. Oldham, S.N. Nandgaonkar, A.R. Neureuther and M.O'Toole, A general simulator for VLSI lithography and etching processes: Part I—Application to projection lithography, IEEE Transactions On Electron Devices, 26(4) (1979) 717-722

[Oldham 1980] W.G. Oldham, A.R. Neureuther, C. Sung, J.L. Reynolds and S.N. Nandgaonkar, A general simulator for VLSI lithography and etching processes: Part II—Application to deposition and etching, IEEE Transactions On Electron Devices, 27(8) (1980) 1455-1459.

[Pelliccione 2006] M. Pelliccione, T. Karabacak, C. Gaire, G.-C. Wang, and T.-M. Lu, Mound formation in surface growth under shadowing, Physical Review B, 74 (2006) 125420.

[Platz 1998] R. Platz, S. Wagner, C. Hof, A. Shah, S. Wieder, B. Rech, Influence of excitation frequency, temperature, and hydrogen dilution on the stability of plasma enhanced chemical vapor deposited a-Si:H, J. Appl. Phys., 84 (1998) 3949-3953.

[Poruba 2000] A. Poruba, A. Feijar, O. Salyk, M. Vanecek, J. Kocka, Surface and bulk light scattering in microcrystalline silicon for solar cells, Journal of Non-Crystalline Solids, 271 (2000) 152-156.

[Poruba 2008] A. Poruba, J. Holovsky, A. Purkrt and M. Vanecek, Advanced optical characterization of disordered semiconductors by Fourier transform

photocurrent spectroscopy, Journal of Non-Crystalline Solids, 354 (2008) 2421-2425.

[Prasad 2002] V. Prasad, M.O. Bloomfield, D.F. Richards, H. Liang, T.S. Cale, Modeling and simulation of plasma enhanced processing for integrated circuit fabrication, Vacuum, 65 (2002) 443-455.

[Python 2006] M. Python, E. Vallat-Sauvain, J. Bailat, C. Ballif and A. Shah, Numerical Simulation of Microcrystalline Silicon Growth on Structured Substrate, Material Research Society Symposium Proceedings, 910 (2006) 0910-A13-02.

[Python 2008] M. Python, E. Vallat-Sauvain, J. Bailat, D. Dominé, L. Fesquet, A. Shah, C. Ballif, Relation between substrate surface morphology and microcrystalline silicon solar cell performance, Journal of Non-Crystalline Solids, 354 (2008) 2258-2262.

[Ramalingam 2001] S. Ramalingam, S. Sriraman, E. S. Aydil, and D. Maroudas, Evolution of structure, morphology, and reactivity of hydrogenated amorphous silicon film surfaces grown by molecular-dynamics simulation, Applied Pysics Leltters, 78 (2001) 2685-2687.

[Rech 2003] B. Rech, T. Roschek, T. Repmann, J. Müller, R. Schmitz and W. Appenzeller, Microcrystalline silicon for large area thin film solar cells, Thin Solid Films, 427 (2003) 157-165.

[Rey 1990] J.C. Rey, L.Y Cheng, J.P. McVittie and K.C. Saraswat, Numerical simulation of CVD trench filling using a surface reaction coefficient model, VLSI Multilevel Interconnection Conference, (1990) 425-427.

[Roca i Cabarrocas 2002] P. Roca i Cabarrocas, A. Fontcuberta i Morral, Y. Poissant, Growth and optoelectronic properties of polymorphous silicon thin films, Thin Solid Films, 403-404 (2002) 39-46.

[Saito 2003] K. Saito, M. Sano, H. Otoshi, A. Sakai, S. Okabe, and K. Ogawa, High efficiency large area solar cells using microcrystalline silicon, Proceedings of the 3rd World Conference on Photovoltaic Energy Conversion, 3 (2003) 2793-2798.

[Sakai 1989] H. Sakai, T. Yoshida, S. Fujikake, Y. Ichikawa, A. Ueda, O. Ischiwata and M. Nagano, Effects of the surface morphology of transparent electrode on film deposition and photovoltaic performance of A-SI:H solar cells, Journal of Non-Crystalline Solids, 115 (1989) 198-200.

[Sakai 1990] H. Sakai, T. Yoshida, T. Hama and Y. Ichikawa, Effects of Surface Morphology of Transparent Electrode on the Open-Circuit Voltage in a-Si:H Solar Cells, Japanese Journal of Applied Physics, 29 (1990) 630-635.

[Shah 2000] A. Shah, E. Vallat-Sauvain, P. Torres, J. Meier, U. Kroll, C. Hof, C. Droz, M. Goerlitzer, N. Wyrsch, and M. Vanecek, Intrinsic microcrystalline silicon (μc-Si:H) deposited by VHF-GD (very high frequency-glow discharge): a new material for photovoltaics and optoelectronics, Mater. Sci. Eng. B, 69-70 (2000) 219-226.

[Shah 2002] A. Shah, J. Meier, E. Vallat-Sauvain, C. Droz, U. Kroll, N. Wyrsch, J. Guillet, U. Graf, Microcrystalline silicon and 'micromorph' tandem solar cells, Thin Solid Films, 403-404 (2002) 179-187.

[Sharf 2004] T. Sharf, A.Shlayen, C. Gernez, N. Basturk and J. Grupp, Liquid crystal alignment on replicated nanostructured surfaces, Mol. Cryst. Liq. Cryst., Taylor & Francis, 411 (2004) 135-145.

[Schropp 1997] R.E.I. Schropp; K.F. Feenstra; E.C. Molenbroek; H. Meiling; J. K. Rath, Device-quality polycrystalline and amorphous silicon films by hot-wire chemical vapour deposition, Philosophical Magazine Part B, 76(3) (1997) 309-321.

[Schropp 1999] R.E.I. Schropp, J.K. Rath, Novel profiled thin-film polycrystalline silicon solar cells on stainless steel substrates, IEEE Transactions on Electron Devices, 46(10) (1999) 2069-2071.

[Schropp 2003] R.E.I. Schropp, J. Adams, A. Bink, P.C.P. Bronsveld, J. Francke, R.H. J. Franken, H.D. Goldbach, A. Gordjin, R.J. Jimenez Zambaro, H. Li, R.W. Lof, J. Löffler, G. van der Mark, J.K. Rath, M. Rusche, R.L. Stolk, M.K. van Veen, and C.H.M. van de Werf, First hot-wire deposited triple junction silicon thin film solar cell, Proceedings of the 3rd World Conference on photovoltaic Energy Conversion, 2 (2003) 1847-1851

[Schultz 2004] O. Schultz, S.W. Glunz, G.P. Willeke, Short communication accelerated publication: Multicrystalline silicon solar cells exceeding 20% efficiency, Progress in Photovoltaics: Research and Applications, 12(7) (2004) 553-558.

[Smets 2008] A.H.M. Smets, T. Matsui, M. Kondo, Infrared analysis of the bulk silicon-hydrogen bonds as an optimization tool for high-rate deposition of

microcrystalline silicon solar cells, Applied Physics Letters, 92 (2008) n° 033506.

[Smy 2001] T. Smy, D. Walkey, K.D. Harris, M.J. Brett, Thin film microstructure and thermal transport simulation using 3D-films, Thin Solid Films, 391(1) (2001) 88-100.

[Smy 2002] T. Smy, S. K. Dew and R. V. Joshi, Modeling 3D effects of substrate topography on step coverage and film morphology of thin metal films, Thin Solid Films, 415(1-2) (2002) 32-45.

[Sriraman 2002] S. Sriraman, S. Agarwal, E.S. Aydil and D. Maroudas, Mechanism of hydrogen-induced crystallization of amorphous silicon, Nature, 418 (2002) 62-65.

[Staebler 1977] D.L. Staebler and C.R. Wronski, Reversible conductivity changes in discharge-produced amorphous Si, Applied Physics Letters, 3 (1997) 292-294.

[Steinhauser 2006] J. Steinhauser, S. Faÿ, R. Schlüchter, S. Y. Myong, E. Vallat, C. Ballif, Boron Doping Effects on the Electro-optical Properties of Zinc Oxide Thin Films Deposited by Low-Pressure Chemical Vapor Deposition Process, Mater. Res. Soc. Symp. Proc., 928 (2006)

[Steinhauser 2008] J. Steinhauser thesis, University of Neuchâtel, (2008)

[Stiebig 1999] H. Stiebig, T. Brammer, J. Zimmer, A. Lambertz, N. Senoussaoui and H. Wagner, Microcrystalline Silicon Pin Solar Cells - Investigation of the Optoelectronic Properties, Rev. Energ. Ren., 2 (1999) 99-108.

[Stout 1993] P.J. Stout and M.J. Kushner, Monte Carlo simulation of surface kinetics during plasma enhanced chemical vapor deposition of SiO2 using oxygen/tetraethoxysilane chemistry, J. Vac. Sci. Technol. A, 11(5) (1993) 2562-2571.

[Strahm 2007] B. Strahm thesis, EPFL, (2007)

[Street 1991] R.A. Street, Hydrogenated Amorphous Silicon, Cambridge University Press, Cambridge, ISBN: 0521019346 (1991).

[Tanem 2005] B. S. Tanem, G. Svenningsen, J. Mardalen, Relations between sample preparation and SKPFM Volta potential maps on an EN AW-6005 aluminium alloy, Corrosion Science, 47(6) (2005) 1506–1519.

[Teresa 2000] R. Terasa, M. Albert, H. Grüger, A. Haiduk, and A. Kottwitz, Investigation of growth mechanisms of microcrystalline silicon in the very high frequency range, J. Non-Cryst. Solids, 266-269 (2000) 95-99.

[Teresa 2002] R. Terasa, M. Albert, J.W. Bartha, H. Brechtel, and A. Kottwitz, Time-resolved layer thickness behavior of microcrystalline and amorphous silicon samples after switching on a hydrogen/silane VHF plasma, J. Non-Cryst. Solids, 299-302 (2002) 58-62.

[Torres 1994] P. Torres, H. Keppner, R. Flückiger, J. Meier, A. Shah, Passivation of Crystalline Silicon Solar Cell Wafers by Amorphous and Microcrystalline Silicon Layers deposited by VHF-GD, Proceedings of the 12th EC Photovoltaic Solar Energy Conference, Amsterdam, (1994) 705-708.

[Torres 1996] P. Torres, J. Meier, R. Flückiger, U. Kroll, J. Anna Selvan, H. Keppner, A. Shah, S.D. Littlewood, I.E. Kelly, P. Giannoulès, Device Grade Microcrystalline Silicon Owing to Reduced Oxygen Contamination, Appl. Phys. Lett., 69 (1996) 1373-1375.

[Tsai 1989] C.C. Tsai, G.B. Anderson, R. Thompson, and B.Wacker, Control of silicon network structure in plasma deposition, J. Non-Cryst. Solids, 114 (1989) 151-153.

[Vallat-Sauvain 2000] E. Vallat-Sauvain, U. Kroll, J. Meier, A. Shah, and J. Pohl, Evolution of the microstructure in microcrystalline silicon prepared by very high frequency glow-discharge using hydrogen dilution, J. Appl. Phys., 87 (2000) 3137-3142.

[Vallat-Sauvain 2005] E. Vallat-Sauvain, J. Bailat, J. Meier, X. Niquille, U. Kroll, A. Shah, Influence of the substrate's surface morphology and chemical nature on the nucleation and growth of microcrystalline silicon, Thin Solid Films, 485 (2005) 77-81.

[Vallat-Sauvain 2006] E. Vallat-Sauvain, C. Droz, F. Meillaud, J. Bailat, A. Shah, C. Ballif, Determination of Raman emission cross-section ratio in hydrogenated microcrystalline silicon, Journal of Non-Crystalline Solids, 352(9-20) (2006) 1200-1203.

[Van Oort 1987] R.C. van Oort, M.J. Geerts, J.C. van den Heuvel, and J.W. Metselaar, Hydrogen plasma etching of amorphous and microcrystalline silicon, Electronic Lett., 23(18) (1987) 967-968.

[Vanecek 2000] M. Vanecek, A.Poruba, Z. Remes, J. Rose, S. Kamba, V. Vorlícek, J. Meier, A. Shah, Electron spin resonance and optical characterization of defects in microcrystalline silicon, Journal of Non-Crystalline Solids, 266-269 (2000) 519-523.

[Vanecek 2001] M. Vanecek and A. Poruba, in "Properties and Applications of Amorphous Materials", edited by M. F. Thorpe and L. Tichy, (Kluwer Academic, The Netherlands), ISBN-10: 079236810X, (2001) 401

[Vanecek 2002] M. Vanecek and A. Poruba, Fourier-transform photocurrent spectroscopy of microcrystalline silicon for solar cells, Applied Physics Letters, 80(5) (2002) 719-721.

[Veprek 1968] S. Veprek and V. Marecek, The preparation of thin layers of Ge and Si by chemical hydrogen plasma transport, Solid-State Electron., 11(7) (1968) 683-684.

[Vetterl 2000] O. Vetterl, F. Finger, R. Carius, P. Hapke, L. Houben, O. Kluth, A. Lambertz, A. Muck, B. Rech and H. Wagner, Intrinsic microcrystalline silicon: A new material for photovoltaics, Solar Energy Materials and Solar Cells, 62 (2000) 97-108.

[Voutsas 1995] A. T. Voutsas, M. K. Hatalis, J. Boyce and A. Chiang, Raman spectroscopy of amorphous and microcrystalline silicon films deposited by low-pressure chemical vapor deposition, Journal of Applied Physics, 78(12) (1995) 6999-7006.

[Wessels 2006] K. Wessels, A. Feldhoff, M. Wark, J. Rathousky, and T. Oekermann, Low-Temperature Preparation of Crystalline Nanoporous TiO2 Films by Surfactant-Assisted Anodic Electrodeposition, Electrochem. Solid-State Lett., 9(6) (2006) C93-C96.

[Yamamoto 1998] K. Yamamoto, M. Toshimi, T. Suzuki, Y. Tawada, T. Okamoto, A. Nakajima, Thin film poly-Si solar cell on glass substrate fabricated at low temperature, MRS Spring Meeting, (1998)

[Yamamoto 2000] K. Yamamoto, M. Yoshimi, Y. Tawada, Y. Okamoto and A. Nakajima, Thin film Si solar cell fabricated at low temperature, Journal of Non-Crystalline Solids, 266-269 (2000) 1082-1087.

[Zhao 1998] J. Zaho, A. Wang, M.A. Green, F. Ferrazza, 19.8% efficient "honeycomb" textured multicrystalline and 24.4% monocrystalline silicon solar cells, Applied Physics Letters, 73 (1998) 1991-1993.

[Zeman 2007] M. Zeman, J. Krc, Electrical and Optical Modelling of Thin-Film Silicon Solar Cells, Proceedings of the Material Research Society, Symposium A (2007) A3.1